Novel Trapping and Scattering of Light in Resonant Nanophotonic Structures

Novel Trapping and Scattering of Light in Resonant Nanophotonic Structures

A DISSERTATION PRESENTED
BY
CHIA WEI HSU
TO
THE DEPARTMENT OF PHYSICS

IN PARTIAL FULFILLMENT OF THE REQUIREMENTS
FOR THE DEGREE OF
DOCTOR OF PHILOSOPHY
IN THE SUBJECT OF
PHYSICS

HARVARD UNIVERSITY
CAMBRIDGE, MASSACHUSETTS
NOVEMBER 2014

Thesis advisor: Professor Marin Soljačić Chia Wei Hsu

Novel Trapping and Scattering of Light in Resonant Nanophotonic Structures

Abstract

Nanophotonic structures provide unique ways to control light and alter its behaviors in ways not possible in macroscopic structures. In this thesis, we explore novel behaviors of light created by nanophotonic structures, with a common theme on resonance effects. The first half of the thesis focuses on a peculiar type of electromagnetic resonance, where the resonance lifetime diverges to infinity. These states, called bound states in the continuum, remain localized in space even though their frequency lie within a continuum of extended modes. We find such states in photonic crystal slabs and the surface of bulk photonic crystals. We show the conditions necessary for them to exist, and provide the first experimental observation of these unusual states. We also show that these states have a topological nature, with conserved and quantized topological charges that govern their generation, evolution, and annihilation. The second half of the thesis concerns light scattering from resonant nanophotonic structures, where resonances can enhance or suppress scattering at particular wavelengths and angles. We show that multiple resonances in one nanostructure and in the same multipole channel generally lead to a scattering dark state where the structure becomes transparent. Based on the coherent interference from multiple scatterers, we show there are geometries that can achieve a sharp structural color where the hue, saturation, and brightness are all viewing-angle independent. We also invent a new type of transparent display based on wavelength-selective light scattering from nanostructures.

To my wonderful wife, Aivi

Contents

List of Figures

List of Tables

Acknowledgments

My PhD journey wouldn't have been half as meaningful, or possible at all, without these people.

I am truly lucky to have Professor Marin Soljačić as my advisor. Marin is incredibly creative and visionary, and he often brings the value of scientific research beyond academic pursuits. He carries a serious face, but is actually one of the nicest professors I have met. He also generates this collaborative and congenial atmosphere that makes working in his group a joyful experience. I am grateful that he took me in when I first "saw the light" and wanted to study nanophotonics. In his group, I have found my interest and passion. Thank you, Marin!

Professor Steven Johnson and Professor John Joannopoulos have been my unofficial co-advisors. Steven has given me valuable lessons for lots of things from physics and numerical tools to paper writing, and I am always amazed at his deep and clear understanding for the mathematics underlying different disciplines. John is an inspirational figure, and conversations with him often bring out whole new directions and ideas. The first time meeting John I was nervous to talk to such an esteemed physicist, but I soon found John to be one of the most friendly and cheerful person I have met.

I thank my undergraduate advisor Professor Francis Starr and my first year's advisor Professor Tim Kaxiras, who started me on the road to physics research. What I learned from them paved a solid foundation for my research. I am grateful to Professor Adam Cohen and Professor Marko Lončar for serving on my committee and providing feedback on my progress.

During this PhD journey, I had the chance to work with and learn from many talented colleagues. When I first came to this group, Bo Zhen taught me all the things that were to become my toolbox for photonics research, from band-structure and FDTD calculations to optical-lab measurement skills. He also turned out to become my closest collaborator; we have been working together on most of our projects since then. Yichen Shen has been a great officemate and friend, sharing with me not just conversations on physics but also many hobbies and pass-times. The experiment on photonic crystal slabs

would not have been possible without Jeongwon Lee, who skillfully fabricated the perfect sample for this study. Owen Miller has worked with me on several projects and has taught me a lot about light scattering and absorption. Ling Lu taught me many things such as semiconductor lasers and topological photonics. Dr. Brendan DeLacy from ECBC taught me how to synthesize nanoparticles. During my first semester at MIT, I inherited the spherical-particle scattering calculation from Wenjun Qiu and benefitted from many discussions with Song Liang Chua. Ofer Shapira and Eric Gastfriend worked closely with me on the transparent display. Professor Hongsheng Chen worked on fiber BIC with me and taught me about metamaterials. I learned lots of physics and teaching tips from Jacob Barandes as a teaching fellow for his class. Emma Anquillare, Li Wang, Nick Rivera, and Asra Ali worked with me on various research projects, and I was privileged to have been their mentor at various points. I thank the current and former members Ognjen Ilic, Scott Skirlo, Ido Kaminer, Yoav Lahini, Adrian Yeng, Veronika Rinnerbauer, and Yi Yang in Marin's group, David Liu, Xiangdong Liang, Homer Reid, Aaron Welters, Adi Pick, and Fan Wang in Steven's group, for the numerous stimulating discussions. And I want to thank my friends at Harvard and MIT and my housemates for the company and fun we had throughout my grad school years.

I want to thank Professor Doug Stone and Professor Hui Cao at Yale for the discussions that led to the work on BIC topological charge and the work on angle-independent structural color.

Lisa Cacciabaudo, Margaret O'Meara, and Lesley Keaney helped me with all kinds of administrative tasks during my years at Harvard and MIT, and I am grateful to them.

Lastly, I would like to thank my family for their everlasting support and encouragement as I pursued my dreams far away from home. I dedicate this thesis to my wife Aivi, who has been my source of happiness and strength.

Chapter 1

Introduction

1.1 The Innocuous Maxwell's Equations

Light is ubiquitous. It gives us vision, heat, the convenience of electricity, telecommunication*, and global internet as enabled by optical fibers—just to name a few. Classically, the behavior of light is governed by four coupled partial differential equations, first presented by James Clerk Maxwell in 1864 [125]. The simplicity and elegance of Maxwell's equations can sometimes disguise the rich and sometimes complex behaviors of light in various structures it interacts with. Despite the long history of classical electromagnetism, unusual behaviors of light are still being discovered in recent years, such as light that propagates without diffraction [171] or only in one direction [228], self-accelerating beams [89], and cloaking [161]. In this thesis, we set out on a journey to explore other interesting behaviors of light—some of them unexpected—that arise from the innocuous Maxwell's equations.

The common objects that we interact with in daily lives typically have features at the millimeter to meter scale, much larger than the wavelength of light. At those length scales, the properties of light are reduced to that of ray optics; therefore we do not observe many of the interesting properties of light as an electromagnetic wave.

*If we generalize to electromagnetic waves beyond optical frequencies.

Interesting properties emerge when the structure light interacts with has features at the length scale comparable to or smaller than light's wavelength—the nanometer to micrometer scale. These are the nanophotonic structure we study in this thesis. Nature engineers its own nanophotonic structures: precious opals [183], certain butterfly wings [221, 222, 184], beetles [159], peacock and bird feathers [167, 248], sea mouse [158], and plants [231, 219] all have structures at the wavelength scale that give them unique colors. But our exploration is not limited to what nature provides us with. The past decade has seen rapid developments in nano fabrication techniques, both for top-down lithographic and direct writing approaches and for bottom-up self-assembly and chemical synthetic approaches. These advancements made it possible to create a wide range of nanoscale structures including those not seen in nature. Armed with the ability to make nanophotonic structures, our exploration can go beyond theorists' imaginations. In several studies in this thesis, we start with theory and proceed to experiments to realize the phenomena of interest.

1.2 Infinite-lifetime Resonances

Several phenomena are explored in this thesis, and a common theme is resonance. In open nanophotonic structures, light can be partially confined and partially leaky, therefore forming resonances—waves that oscillate and attenuate gradually. In the first half of the thesis, we study a peculiar type of electromagnetic resonance, where the resonance lifetime diverges to infinity. These are electromagnetic waves that oscillate indefinitely without decaying even though they reside in a leaky open structure. This is like having a cup with water level much higher than the rim, and yet the water does not leak out[†].

[†]No, I am not talking about surface tension.

Or this is like plucking a string of a guitar, and the string continues to oscillate forever. Physicists will be familiar with another analogy: a localized wave function with positive energy even though the potential goes to zero at infinity, which many elementary quantum mechanics textbooks (such as Griffith [57]) say is impossible. Such an impossible state is called a "bound state in the continuum" or an "embedded eigenstate." As it turns out, these unusual states exist in very simple nanophotonic structures, and we are the first to experimentally observe such states[‡].

In Chapter 2, we show that infinite-lifetime resonances exist on the surface of bulk photonic crystals. These are Bloch-periodic surface eigenstates inside the continuum of free-space modes. Coupling to the free space causes the surface modes to leak, but the forward and back-reflected leakage can interfere destructively to create a state perfectly confined to the surface with no leakage. We perform analytical temporal coupled-mode theory analysis to show the generality of such a phenomenon and its robustness from variations of system parameters. We find that periodicity, time-reversal invariance, two-fold rotational symmetry, and a perfectly reflecting boundary are necessary for this type of embedded eigenstates.

In Chapter 3, we present both theoretical prediction and experimental observation of infinite-lifetime resonances in photonic crystal slabs—structures that are finite in one direction and periodic in the other two directions. Again, these states are not index-guided; they are above the light line, within the continuum of free-space modes. Photonic crystal slabs are relatively easy to fabricate (unlike bulk photonic crystals), making this type of embedded eigenstates much easier to realize than other types. We are able to fabricate the structure and observe these unusual states experimentally for

[‡]Barring those arising from symmetry incompatibilities, which are almost trivial and have been known for decades.

the first time. We show that these states exist in a general class of geometries, and we show how to detect them experimentally using angle- and spectral-resolved reflectivity measurements.

In Chapter 4, we show that these unusual infinite-lifetime resonances are vortex centers in the polarization directions of the far-field radiation. The robustness of these states arises from conserved and quantized topological charges, which we define using the winding number of the polarization vectors. We find that there are strict rules governing the generation, evolution and annihilation of these charges. This finding connects these states to a wide range of topological physical phenomena.

1.3 Resonant Light Scattering

Light scattering is important for many reasons. For one, it is the reason that we see things—incident light (from the sun or from a light bulb) scatters off objects, and we see the objects because the scattered light enters our eyes. When light impinges on a macroscopic object, the amount of light being scattered—the scattering cross section—is determined by the size of the object (its geometric cross section) and is independent of the wavelength and the incident or scattering angle. However, a resonant nanophotonic structure can appear to light as being much larger or much smaller than its geometric size; the scattering can be enhanced or suppressed by the resonance. The scattering can also be highly wavelength dependent and/or highly angle dependent. The presence of multiple resonances or multiple scatterers brings even more possibilities through mode hybridization and interference. In the second half of the thesis, we study unusual light scattering properties due to resonances, and we present a novel application of it on transparent displays.

In Chapter 5, we present a new type of transparent display that is enabled by resonant light scattering. We project monochromatic images onto a transparent medium embedded with nanoparticles that selectively scatter light at the projected wavelength. The projected images show up on the screen due to the scattering, and yet the screen remains highly transparent. We describe the optimal design of such nanoparticles, and experimentally demonstrate this concept with a blue-color transparent display made of silver nanoparticles in a polymer matrix. This new type of transparent display has attractive features including simplicity, wide viewing angle, scalability to large sizes, and low cost.

In Chapter 6, we describe the phenomenon of a scattering dark state using temporal coupled-mode theory. We find that when there are multiple resonances in the same "channel" (each channel is a multipole, corresponding to a distinct angular momentum and polarization), coherent interference of the scattered waves can lead to a transparency frequency where the scattering cross section in this channel vanishes. We consider nanostructures that are spherical or non-spherical but subwavelength in size, and we find that such scattering dark states always exist in the low-absorption limit, regardless of the system details. This phenomenon can be interpreted as arising from far-field or near-field coupling. We provide explicit examples to illustrate these concepts.

In Chapter 7, we consider how the coherent interference of waves scattered from multiple scatterers can be designed to create sharp and viewing-angle-independent structural colors. Structural coloration produces some of the most brilliant colors in nature. However, sharp color (narrow frequency response) and wide viewing angle (broad angular response) are competing properties and have not been achieved simultaneously in previous studies. Here, we show that both goals can be achieved simultaneously through an optimization-based design. We use a model system consisting of dipole

scatterers arranged into ring shapes; the scattered waves interfere to yield the desired wavelength-selective and yet angle-insensitive response. With this approach, we discover extraordinary structures where the structural color is very sharp and yet the hue, saturation, and brightness are all viewing-angle independent when illuminated from a directional light source.

Finally, in Chapter 8, we provide concluding remarks and future outlooks.

Materials of the chapters are largely based on our works in Refs. [71, 72, 75, 73, 74, 247]. Meanwhile, Refs. [31, 132, 133, 32, 5, 188] describe other related works of us that are not covered in this thesis.

Chapter 2

Bloch surface eigenstates within the radiation continuum*

2.1 Introduction

Soon after the discovery of photonic bandgap materials, it became known that electromagnetic modes could be localized on the surface of a photonic crystal (PhC) [80, 126]. Such a state may exist if it cannot couple to any bulk state in the PhC or to any free-space mode in air; the band-gap of the PhC prohibits propagation, serving the same role as metals and negative-index materials in surface plasmon modes [214]. These PhC surface states have been observed experimentally [174, 77], and their localized properties have been applied to enhance light collimation [139, 101] and to manipulate photons on defects of the surface [77]. It is often thought that bona fide photonic surface states can only exist below the light cone of the ambient air (i.e. below the continuum of radiation modes in air), where they are confined by total internal reflection. We show that, under appropriate but general conditions, photonic surface states may also exist inside the radiation continuum. Although coupling to radiation modes is allowed, such a state

*This chapter is based on: C. W. Hsu, B. Zhen, S.-L. Chua, J. D. Joannopoulos, and M. Soljačić, "Bloch surface eigenstates within the radiation continuum," *Light: Science & Applications* **2**, e84 (2013).

can have an infinite lifetime because different leakage channels interfere destructively to completely cancel each other.

To explain the physical origin of perfect cancellation among different leakage channels, we carry out rigorous analysis using temporal coupled-mode theory, which provides a generic description for coupling between the localized and propagating modes. We find that in addition to periodicity along the surface and a photonic bandgap that perfectly reflects light, the existence of these embedded Bloch surface eigenstates also requires unbroken time-reversal symmetry and a C_2 rotational symmetry about the surface normal. The analysis applies to general wave systems, suggesting that this phenomenon may exist beyond optical systems. Such states offer new possibilities that may find use in the design of narrow-band waveguiding structures or in applications where strongly localized fields are desired.

We also note that, a lossless Bloch surface mode inside the radiation continuum falls within a rare class of states known as *embedded eigenvalues* [220, 69, 201, 49, 143, 197, 135, 175, 146, 102, 244, 154, 153, 149, 41, 190, 162, 108, 217, 92, 229, 124, 137, 191, 216, 86, 160, 234, 39, 38, 58, 163, 111]. Shortly after the emergence of quantum mechanics, von Neumann and Wigner proposed that the single-particle Schrödinger equation may possess spatially localized states lying above the asymptotic limit of the potential and embedded in the continuum of extended states [220]. Unlike non-embedded eigenvalues, embedded eigenvalues are typically difficult to find and generally disappear (become resonances) when slightly perturbed. Moreover, the impractical nature of the original proposed artificial Hamiltonians has made experimental verification difficult. For this reason, an embedded eigenvalue in quantum systems has never been demonstrated. The only known attempt concerns an electron bound state lying above the quantum-well potentials of a superlattice heterostructure, but within the bandgap

of its mini bands [24], *i.e.* not an embedded eigenvalue. Thus theoretical explorations to discover simpler, easily realizable, and more robust systems that can contain embedded eigenvalues are of great interest. Embedded eigenvalues have also been explored in Maxwell's equations [154, 153, 149, 41, 190, 162, 108, 217, 92, 229, 124, 137, 191] and in the acoustic and water wave equations [216, 86, 160, 234, 39, 38, 58, 163, 111]. One occasion is when the spectrum of the problem can be separated by space group symmetry and when an odd-symmetry bound state lies in the continuum spectrum of the even states [154, 153, 149, 41, 190, 162, 108, 216, 86, 160, 234, 39]. Embedded states that do not rely on symmetry separability have received much attention [201, 49, 143, 175, 146, 197, 135, 102, 244, 217, 92, 229, 124, 137, 191, 38, 58, 163, 111] but have never been experimentally verified, primarily because they are fragile to perturbations. (Among them, Refs. [175, 146, 217, 92, 229] concern embedded states due to coordinate separability instead of symmetry separability.) In this work, we identify theoretically a new realization of an embedded eigenvalue in a PhC system that does not rely on symmetry, yet should be easily realizable. Moreover, we find that unlike most known embedded eigenvalues, the one described here is robust from changes of system parameters; the eigenvalue simply shifts to another wavevector without fading into a resonance (as is characteristic in other embedded eigenvalue systems). The possibility of an embedded eigenvalue in a very similar structure was previously suggested by numerical investigations [189], but without proof or explanation of how such a state might arise.

2.2 Surface Eigenstate In The Continuum

For comparison, we begin with a known example of a PhC surface-mode band structure [80, 174], given in Figure 2.1a, where the PhC is a 2D square lattice of dielectric

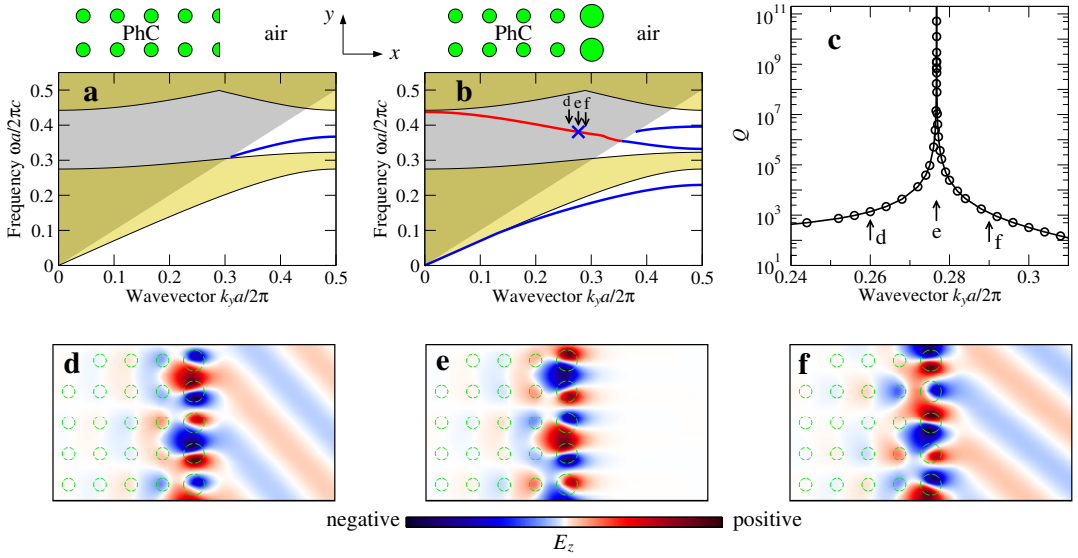

Figure 2.1: Properties of surface modes lying within the radiation continuum. (**a**) and (**b**) Projected band structures for a square lattice (period a) of cylindrical dielectric rods ($\epsilon = 8.9$, $r = 0.2a$) in air, with terminations as shown in the insets. In **a**, the surface rods are cut in half, while in **b**, the surface rods have increased radii, $r_s = 0.33a$. Gray shaded regions represent the light cone where there is a continuum of radiation modes. The light and dark khaki regions are the projected bulk bands of the PhC. Surface modes that do not couple to radiation are shown as blue lines (these are the well known states) and a blue cross (this is an embedded eigenstate); those that do couple to radiation are shown as a red line. (**c**) Quality factor Q for the leaky surface modes along the red line in **b**. At $k_y = 0.2768 \times 2\pi/a$, the lifetime goes to infinity, and the leaky mode becomes an eigenmode. (**d-f**) E_z field patterns of the surface modes at the specified wavevectors, where $k_y a/2\pi = 0.260$, 0.2768, 0.290 respectively.

cylinders. By terminating the surface rods in half on the (100) surface, one creates surface modes in the lowest photonic bandgap of TM modes (where electric field is normal to the plane, $\mathbf{E} = E_z\hat{\mathbf{z}}$). These states are on the lowest-frequency band of the surface rods; they lie below the light cone, and do not interact with the continuum of free-space modes. In comparison, higher-frequency bands of the surface rods can be brought into the photonic bandgap of the same bulk PhC by increasing the radii of the surface rods; this band structure is shown in Figure 2.1b. Here, the second band enters the light cone, where it couples to the radiation modes and becomes leaky. From finite-difference time-domain (FDTD) simulations [152], we excite these resonances with point sources on the surface, and perform harmonic analysis to obtain the lifetime τ and quality factor $Q = \omega\tau/2$ of these resonant modes. As shown in Figure 2.1c, there is a sharp increase of lifetime that approaches infinity when the surface-parallel wavevector is near $k_y \approx 0.28 \times 2\pi/a$, with a being the period of the PhC. In other words, there is a discrete point of wavevector where the resonant mode decouples from radiation and becomes an eigenstate. Figures 2.1d-f show the field profiles E_z of the surface modes at and away from the peak. There is no leakage to air at the particular wavevector (Figure 2.1e), in contrast to nearby resonant modes (Figures 2.1d-f) where radiation leakage is clearly visible.

2.3 Interference Effect

This phenomenon can be understood as an interference effect. The surface rods support a localized mode, which leaks to the right into the air (channel one), and to the left into the bulk PhC. Since the frequency of the state is inside the bandgap of the bulk PhC, all the left-going light is reflected, and part of that is transmitted through the surface

rods into the air (channel two), interfering with channel one. When waves in these two channels have the same magnitude and differ in phase by π, destructive interference eliminates the radiation loss.

Periodicity is an important ingredient to these unique embedded states. If the structure is uniform in the surface-parallel direction (such as a plain uniform slab next to a uniform bulk structure), then any state within the radiation continuum must be leaky because fields in the air consist of propagating planewaves only. On the other hand, when the structure has periodicity in the surface-parallel direction (y-direction), fields in the air can consist of evanescent fields with any wavevector k_y in the reciprocal lattice (i.e. k_y's that differ by integer multiples of $2\pi/a$), so an infinite-lifetime resonance may exist. In the present case, periodicity also gives rise to band folding, which creates the resonant modes we study.

Given periodicity, it still remains to be answered if a *perfect* cancellation between the forward leakage and the back-reflected leakage can occur at all, and if so, what the other required conditions are. Furthermore, for experimental demonstrations, it is also critical to know whether the occurrence of such unique states is robust from small differences between the theoretical structure and the fabricated structure. In the next section, we carry out an analysis using temporal coupled-mode theory to answer these questions and to explain why such states do indeed exist and should be readily observable experimentally.

2.4 Coupled-Mode Theory Analysis

In our intuitive understanding of cancellation, the coupling between the surface mode and the radiating modes is an essential element. Therefore we apply temporal coupled-

mode theory [80, 66], which provides a simple analytical description for resonant objects weakly coupled to incoming and outgoing ports. Temporal coupled-mode theory has been widely used in a variety of resonator systems ranging from optical waveguides and cavities, electronic circuits, to mechanical and acoustic resonators. It works well in the weak-coupling regime (when $Q = \omega_0\tau_0/2 \gg \pi$); in practice it is nearly exact when $Q > 30$, which is the case for all examples considered in this work. In our system, ω_0 is the frequency of the localized mode, and τ_0 is its lifetime when coupled to planewave modes in air (without considering the back-reflection). Inside the bandgap, the bulk PhC reflects all incoming waves. Thus, we treat the bulk PhC as a perfectly reflecting mirror, as illustrated in Figure 2.2. The amplitude A of the localized mode evolves as $dA/dt = (-i\omega_0 - 1/\tau_0)A$ in the absence of input powers. When incoming planewaves are included, the temporal coupled-mode theory equation can be written in Dirac notation as [80, 66, 42]

$$\frac{dA}{dt} = \left(-i\omega_0 - \frac{1}{\tau_0}\right) A + \langle \kappa^* | s_+ \rangle \tag{2.1a}$$

$$|s_-\rangle = \mathbf{C}|s_+\rangle + A|d\rangle \tag{2.1b}$$

where $|s_+\rangle$ and $|s_-\rangle$ are column vectors whose components s_{1+}, s_{2+} and s_{1-}, s_{2-} respectively, are amplitudes of the incoming and outgoing planewave modes as illustrated schematically in Figure 2.2, and $|\kappa\rangle$ and $|d\rangle$ are coupling coefficients between the localized mode and the planewave modes. The matrix C is a scattering matrix that describes the direct coupling between the planewave modes on both sides of the rods. We choose the normalizations such that $|A|^2$ is the energy inside the rods, and that $|s_{m+}|^2$ and $|s_{m-}|^2$ are the incoming and outgoing powers in the m-th planewave mode. The coupling coefficients $|\kappa\rangle$, $|d\rangle$ and the direct scattering matrix C are not independent; energy

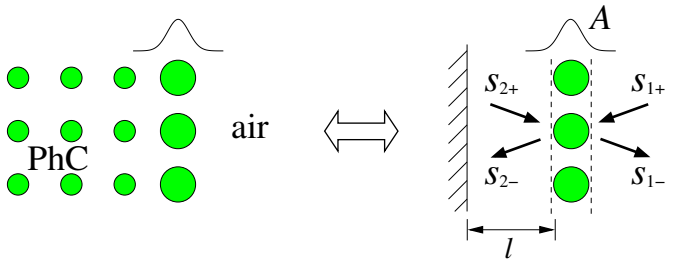

Figure 2.2: Schematics for the setup of temporal coupled-mode theory. Inside the band-gap, the bulk photonic crystal reflects all incoming light, so in our analysis we treat the PhC as a reflecting boundary. In temporal coupled-mode theory, the localized mode has amplitude A, which is coupled to the incoming and outgoing waves with amplitudes $|s_+\rangle$ and $|s_-\rangle$ respectively. Dashed lines indicate the reference planes for the phase of $|s_\pm\rangle$.

conservation and time-reversal symmetry require these coefficients to be related by

$$|\kappa\rangle = |d\rangle \tag{2.2a}$$

$$\langle d|d\rangle = \frac{2}{\tau_0} \tag{2.2b}$$

$$\mathbf{C}|d^*\rangle + |d\rangle = 0. \tag{2.2c}$$

as has been shown in Ref. [42].

The localized mode couples to one planewave mode on each side of the rods, with the surface-normal wavevector of the planewave given by $k_x = \sqrt{(\omega/c)^2 - k_y^2}$. In the frequency range of interest, higher order diffractions (with k_y differ by integer multiples of $2\pi/a$) correspond to evanescent modes with imaginary k_x that do not carry outgoing power, so they can be neglected. The reflection from the bulk PhC imposes

$$s_{2+} = e^{i\psi} s_{2-} \tag{2.3}$$

with ψ being a phase shift. For reflection from the bulk PhC, there is no explicit

expression of this phase shift. But for a closely related system where the PhC is replaced with a perfect metal distance l away from the rods, the phase shift is simply $\psi = 2k_x l - \pi$. Also, we write the direct scattering matrix as $\mathbf{C} = \begin{pmatrix} r & t' \\ t & r' \end{pmatrix}$, where r [r'] and t [t'] are the complex reflection and transmission coefficients on the left [right] side of the rods. In the absence of input power ($s_{1+} = 0$), a stationary state with no leakage ($s_{1-} = 0$) occurs when

$$e^{-i\psi} = r' - \frac{d_2}{d_1} t'. \tag{2.4}$$

This equation is a mathematical translation of the intuitive statement that the forward leakage $d_1 A$ and the back-reflected leakage $te^{i\psi} s_{2-}$ cancel each other.

The question remains whether such cancellation can occur generally, and if so, what are the requirements. Assume time-reversal symmetry in the system is unbroken (i.e. negligible absorption, and no magneto-optic effect imposed). Then, the complex conjugate of fields in the direct scattering process $|s_-\rangle = C|s_+\rangle$ is a solution of the Maxwell's equations with opposite wavevector [80], namely $|s_+\rangle^* = C'|s_-\rangle^*$ where C' is the scattering matrix of wavevector $-k_\parallel$. Further, assume that the structure has two-fold rotational symmetry C_2 about the surface normal, so that $C = C'$; in the present example where the z dimension is uniform, mirror symmetry σ_y is sufficient. These results combine to $|s_-\rangle = CC^*|s_-\rangle$, and so $CC^* = \hat{I}$, which gives the Stokes relations $|r|^2 + t't'^* = 1$ and $r't'^* + r^*t = 0$. Same procedure on the process $|s_-\rangle = C|s_+\rangle + A|d\rangle$ leads to equation (2c), which reduces to $t|d_2|^2 - t'|d_1|^2 + r'd_1^* d_2 - rd_1 d_2^* = 0$. Combining this and the Stokes relations, we get $r - d_2 t/d_1|^2 = 1$. In other words, in the presence of time-reversal symmetry and a C_2 rotational symmetry about the surface normal, the right-hand side of equation (4) always has unit magnitude.

2.5 Robustness of cancellation

The left-hand side of equation (4) also has unit magnitude because of the perfectly reflecting boundary. In such case, *the magnitude condition is always satisfied*, and equation (4) can be reduced to the phase

$$\psi + \arg\left(r' - \frac{d_2}{d_1}t'\right) = 2n\pi \tag{2.5}$$

with n being an integer. In other words, this phase condition, equation (5), is the only requirement for achieving perfect cancellation. Intuitively, it may be understood as a sum of phase shifts, with the first term ψ coming from propagation and reflection, and the second term $\arg(r - d_2 t/d_1)$ coming from coupling with the localized mode. A conceptually similar phase-shift equation has been used in the context of metallic nanorod cavity, where the second term is replaced with the phase shift from coupling with surface plasmon [3]. Equation (5) comes down to locating where the phase shift crosses integer multiples of 2π. Such an intersection may be located by varying the wavevector k_y; it results in discrete states with infinite lifetimes, as we have observed in Figure 2.1c. Not all bands in the light cone will produce such crossings; for example, our previous reasoning indicates that structures without periodicity cannot support such embedded states, so the phase shift for such structures should never cross integer multiples of 2π. But once a crossing is found, the existence of a root will be robust to changes of system parameters since the perturbation will only shift the intersection to a slightly different wavevector.

We note a subtle but important difference between the embedded eigenvalue we study here and that in most known examples. In most examples, the embedded eigenvalue

disappears when the parameters of the system deviates slightly from the designed structure or potential, making it very difficult to observe experimentally. In our case, we are concerned with a *family* of eigenproblems, with each eigenproblem defined by the wavevector of the system. When the parameters of the system change, the embedded eigenvalue disappears from the eigenproblem of one wavevector, but appears in that of another wavevector. In experiments, states with all wavevectors can be measured, and therefore this shifting does not prevent us from physically observing such states. Following this reasoning, we can also expect that embedded eigenvalues in other periodic systems such as Refs [124, 163] should also be robust to parameter changes.

Lastly, we mention that the lifetime of certain resonant cavities can be increased by optimizing their geometries to cancel the dominant component of the far-field radiation [85, 223, 2, 90] (45-48). However, the embedded eigenstate described here, though not localized in the surface-parallel direction, achieves *complete* cancellation, which includes all components of the far-field radiation.

2.6 Validation Of Analysis

The coupled-mode analysis has translated our intuitive picture of cancellation into mathematical statements. Furthermore, it showed that perfect cancellation is possible given time-reversal and C_2 symmetries in the system. Next, we compare its quantitative predictions with numerical simulations.

With no input power ($s_{1+} = 0$), equations (1) and (3) have solution
$A(t) = A(0)\exp(-i\omega t - t/\tau)$ with decay rate

$$\frac{1}{\tau} = \frac{1}{\tau_0} - \mathrm{Re}\left\{\frac{d_2^2}{e^{-i\psi} - r'}\right\} \tag{2.6}$$

This gives the lifetime τ and quality factor Q of the mode. At the perfect-cancellation points discussed in previous section, τ is infinite; away from these points, τ is finite.

Several reference quantities, the natural frequency ω_0, lifetime τ_0, and the left/right ratio of the decay rates which we denote as $\xi \equiv |d_2/d_1|^2$, are measurable and can also be calculated in FDTD simulations. The direct scattering matrix C may be approximated by treating the surface rods as a slab. With these values known, the coupling coefficients d_1 and d_2 can be determined from equation (2), and lifetime of the localized mode and the location of the perfect-cancellation point can be evaluated from equations (6) and (5) respectively to yield quantitative predictions. Equation (2c) gives a quadratic equation with two roots $\frac{d_2}{d_1} = \frac{t'}{2r'}(1-\xi) \pm \sqrt{\left(\frac{t'}{2r'}\right)^2 (1-\xi)^2 + \frac{r}{r'}\xi}$; for rods with mirror symmetry in x direction, we have $\xi = 1$ and $r = r'$, and these two roots correspond to modes whose E_z are even ($d_1 = d_2$) or odd ($d_1 = -d_2$) in x direction.

For quantitative validation of these predictions, we consider some explicit examples. First, we consider a simplifying example where the PhC is replaced with a perfect-metal boundary at distance l from the surface rods (Figure 2.3a inset). In this system, the phase shift at the reflection boundary is simply π, making evaluation of the coupled-mode theory equations easy. This perfect-metal boundary also makes the eigenmodes of this structure equivalent to the asymmetric eigenmodes of a double-column structure (with separation $2l$), which has been studied in Ref. [124] (27) with a Fabry-Perot transmission analysis. Figure 2.3a shows the band structure for separation $l = 1.6a$. The quality factor $Q(k_y)$ of the second band inside the light cone is computed from FDTD simulations and shown in circles in Figure 2.3b; two infinite-lifetime states corresponding to $n = 0$ and $n = 1$ in equation (5) are observed. Since $\psi = 2k_x l - \pi$, we expect that qualitatively the surface-normal wavevector k_x of the infinite-Q states should be inversely proportional to the separation l, which is confirmed in Figure 2.3c. We also ex-

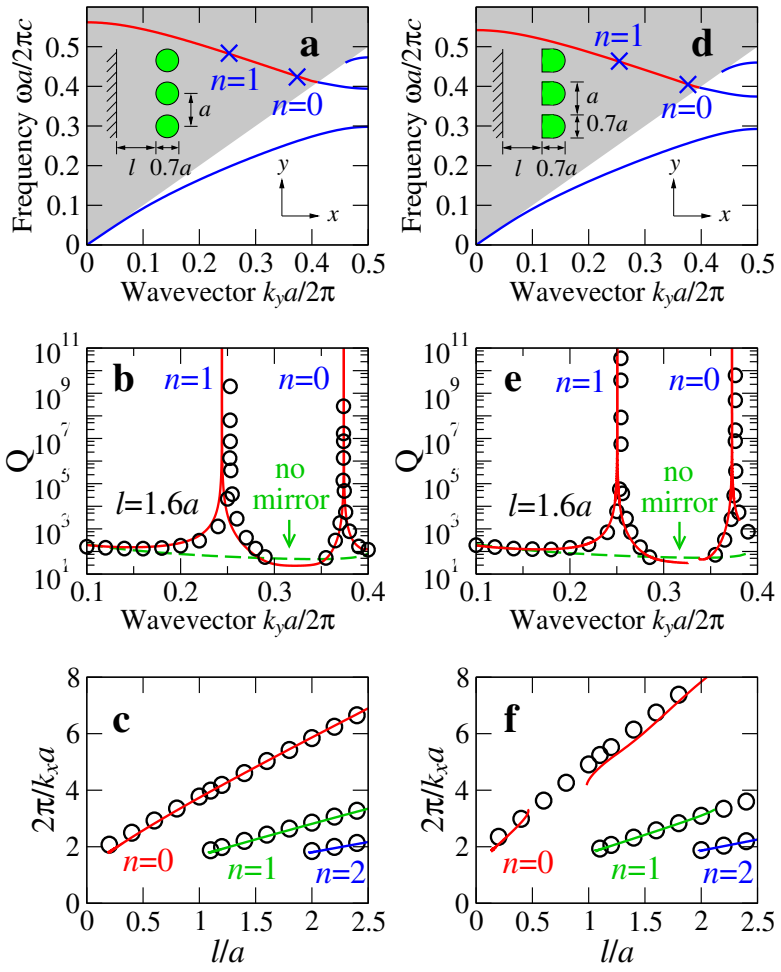

Figure 2.3: Comparison between FDTD simulations and temporal coupled-mode theory predictions, for a simplified structure where the PhC is replaced with a perfect-metal boundary. Left: data for one column of cylindrical rods with $\epsilon = 4.9$. (**a**) Band structure for TM modes with $l = 1.6a$. Shaded region is the light cone, states that do not couple to radiation are shown in blue, and states that do are shown in red. The embedded eigenstates are indicated with blue crosses, labeled with the integer n in equation (5). (**b**) Quality factor Q for leaky modes along the red line in **a**. Circles are from FDTD simulations, and the red solid line is the prediction from equation (6). The green dashed line shows Q for the same structure without a mirror. (**c**) Relation between the surface-normal wavevector k_x of the embedded eigenstates and the rod-to-mirror distance l. Circles are from FDTD simulations, and lines are predictions from equation (5). Right: (**d-f**) show the same plots as in the left column, but with asymmetric rods as shown in the inset.

pect that at larger separation, there will be more embedded eigenstates that correspond to phase shifts differ by $2n\pi$; this is indeed observed in the numerical simulations.

For comparison, we evaluate predictions from equations (5) and (6). We approximate the direct scattering matrix C as the TM scattering matrix of a uniform slab with thickness equal to the rod diameter and the dielectric constant equal to a spatial average of the structure. The natural frequency ω_0 and lifetime τ_0 of the localized mode are calculated from FDTD with only the rods (no mirror). Without the mirror, E_z profile of the band of interest is even in x, so we choose the $d_1 = d_2$ root. Predictions of equations (5) and (6) are plotted in Figure 2.3c and b respectively as solid lines. Quantitative agreement between FDTD and the model is observed.

When the separation l is smaller than the rod diameter, we observe some discrepancy between the FDTD results and the model predictions. This is expected, because when the mirror is less than half a wavelength away from the rods, it starts to distort symmetry of the resonance on the rods, and the assumption $d_1 = d_2$ above is no longer valid. But we note that breaking σ_x symmetry of the resonance does not suppress the infinite-lifetime state, which is consistent with our coupled-mode theory explanations.

The temporal coupled-mode theory analysis applies to localized modes in arbitrary geometries. To illustrate this point, we consider one more example, where the rods consist of a flat edge and a circular edge, as shown in the inset of Figure 2.3d. Data for this geometry are shown in Figure 2.3d-f. We see that the same features of infinite lifetime occur, demonstrating that the described embedded eigenstates are not sensitive to geometry. Again we evaluate equations (5) and (6) to compare with FDTD, with the only difference being that the decay ratio ξ is no longer unity because the left-right symmetry is broken. The same approximation for the direct scattering matrix C is used, although in this case there is a small region where no solution of d_1 and d_2 exists;

this is the discontinuity in the red curve of Figure 2.3f. Again, we observe very good agreement between temporal coupled-mode theory and FDTD.

2.7 Imperfect reflection

Lastly, we comment that when reflection on the boundary is not perfect, the lifetime will no longer be infinite but can still be very large. For the structure in Figure 2.3b with only four periods of small rods in x direction, the finite-sized PhC will allow some light in the bandgap to pass through (intensity reflectance $R = 0.9998$ for the four-period PhC at the wavelength and angle of interest), yet the peak of Q still reaches 6×10^6. For the structure in Figure 2.3a-b with a plain silver mirror (material ohmic losses included, with complex refractive index from Ref. (49)) and assuming periodicity $a = 300$ nm, the first peak of Q (where the mirror has $R = 0.996$) still reaches 2×10^4, which is 300-times enhancement compared to the no-mirror case. For the second peak, the mirror has larger reflectivity $R = 0.999$ because it is near grazing incidence, and the peak of Q reaches 7×10^4 (1300-times enhancement).

2.8 Conclusions

To summarize, we have demonstrated that surface-localized Bloch eigenstates can exist inside the radiation continuum, without using the symmetry-separability of the spectrum. This is a new class of surface modes, and it can be interpreted as the von Neumann-Wigner states realized in a simple photonic system. Infinite lifetime is achieved by complete cancellation between the two leakage channels, and four ingredients enable this cancellation: (i) periodicity, (ii) time-reversal invariance, (iii)

two-fold rotational symmetry, and (iv) a perfectly reflecting boundary. These states may be excited for example through near-field coupling either with a prism or with a gain medium in direct contact with the surface. The narrow width of the high-Q state indicates that it may be useful in the design of narrow-band waveguiding structures and single-mode lasers [28, 18]. As compared to high-Q Fano states at the Γ point [154, 153, 149, 41, 190, 108], this state offers two unique advantages: (i) the angle at which it occurs is tunable, and (ii) the radiative Q of this state can be tuned to arbitrary values by using a non-perfect reflector or by weakly breaking one of the symmetry requirements. The enhanced lifetime, large surface area, and strong localization of these surface states also suggest that they may find use in fluorescence enhancement [67], spectroscopy [177], sensing [116], and other applications where strong light-matter interaction is desired. The analysis we perform here with temporal coupled-mode theory treatment is general, and we believe states similar to those reported in this paper may also be observed in more systems, possibly beyond optics.

Chapter 3

Observation of trapped light within the radiation continuum*

3.1 Introduction

The ability to confine light is important both scientifically and technologically. Many light confinement methods exist, but they all achieve confinement with materials or systems that forbid outgoing waves. Such systems can be implemented by metallic mirrors, by photonic band-gap materials [80], by highly disordered media (Anderson localization [105]) and, for a subset of outgoing waves, by translational symmetry (total internal reflection [80]) or rotation/reflection symmetry [162, 108]. Exceptions to these examples exist only in theoretical proposals [229, 124, 137, 71]. Here we predict and experimentally demonstrate that light can be perfectly confined in a patterned dielectric slab, even though outgoing waves are allowed in the surrounding medium. Technically, this is an observation of an "embedded eigenvalue" [69]—namely a bound state in a continuum of radiation modes—that is not due to symmetry incompatibility [220, 137, 201, 49, 244, 229, 124, 71, 163, 111, 102]. Such a bound state can exist stably in a general

*This chapter is based on: C. W. Hsu†, B. Zhen†, J. Lee, S.-L. Chua, S. G. Johnson, J. D. Joannopoulos, and M. Soljačić, "Observation of trapped light within the radiation continuum," *Nature* **499**, 188 (2013) [†equal contribuation].

class of geometries where all of its radiation amplitudes vanish simultaneously due to destructive interference. This method to trap electromagnetic waves is also applicable to electronic [49] and mechanical waves [163, 111].

The propagation of waves can be easily understood from the wave equation, but the localization of waves (creation of bound states) is more complex. Typically, wave localization can only be achieved when suitable outgoing waves either do not exist or are forbidden due to symmetry incompatibility. For electromagnetic waves, this is commonly implemented with metals, photonic bandgaps, or total internal reflections; for electron waves, this is commonly achieved with potential barriers. In 1929, von Neumann and Wigner proposed the first counterexample [220], in which they designed a quantum potential to trap an electron whose energy would normally allow coupling to outgoing waves. However, such artificially designed potential does not exist in reality. Furthermore, the trapping is destroyed by any generic perturbation to the potential. More recently, other counterexamples have been proposed theoretically in quantum systems [201, 49, 244], photonics [229, 124, 137, 71], acoustic and water waves [163, 111], and mathematics [102]; the proposed systems in Refs. [124] and [163] are most closely related to what is demonstrated here. While no general explanation exists, some cases have been interpreted as two interfering resonances that leaves one resonance with zero width [201, 49, 124]. Among these many proposals, most cannot be readily realized due to their inherent fragility. A different form of embedded eigenvalue has been realized in symmetry-protected systems [162, 108], where no outgoing wave exists for modes of a particular symmetry.

3.2 Bound State in the Continuum in a Photonic Crystal Slab

To show that an optical bound state is feasible even when it is surrounded by symmetry-compatible radiation modes, we consider a practical structure: a dielectric slab with a square array of cylindrical holes (Figure 3.1a), an example of photonic crystal (PhC) slab [80]. The periodic geometry leads to photonic band structures, analogous to how a periodic potential in solids gives rise to electron band structures. The PhC slab supports guided resonances whose frequencies lie within the continuum of radiation modes in free space (Figure 3.1b); these resonances generally have finite lifetimes because they can couple to the free-space modes. However, using finite-difference time-domain (FDTD) simulations [208] and along with the analytical proof below, we find that the lifetime of the resonance goes to infinity at discrete k points on certain bands; here we focus on the lowest TM-like band in the continuum (referred to as TM_1 hereafter), with its lifetime shown in Figure 3.1c, d. At these seemingly unremarkable k points, light becomes perfectly confined in the slab, as is evident both from the divergent lifetime and from the field profile (Figure 3.1e). These states are no longer leaky resonances; they are eigenmodes that do not decay. In the functional analysis literature, eigenvalues like this, which exist within the continuous spectrum of radiation modes, are called *embedded eigenvalues* [69]. Here, embedded eigenvalues occur at five k points over the first Brillouin zone. The one at Γ arises because symmetry forbids coupling to any outgoing wave [108]; the other four (which are equivalent under 90° rotations) deserve further analysis since, intuitively, they should not be confined.

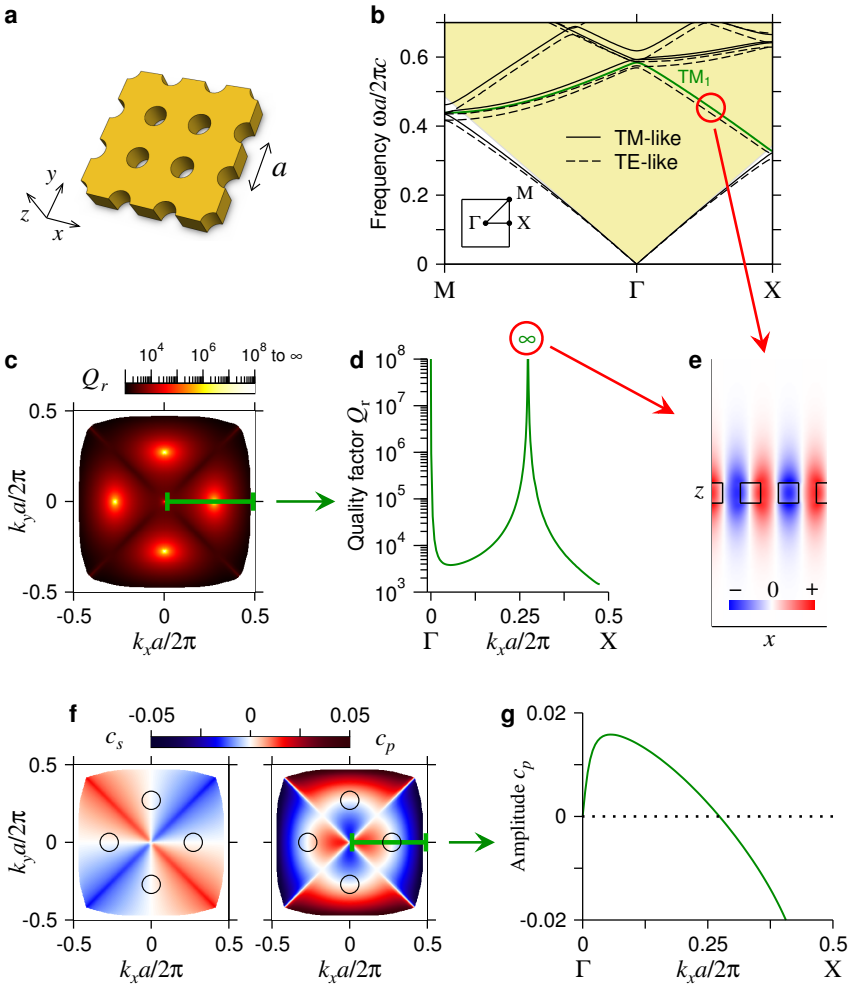

Figure 3.1: Theory predictions. a, Schematic of the photonic crystal (PhC) slab. **b,** Calculated band structure. Yellow shaded area indicates light cone of the surrounding medium, where there is a continuum of radiation modes in free space. The trapped state is marked with a red circle, and the TM_1 band is marked with a green line. Inset shows the first Brillouin zone. **c, d,** Normalized radiative lifetime Q_r of the TM_1 band calculated from FDTD, with values along the Γ-X direction shown in **d**. Below the light cone there is no radiation mode to couple to (*i.e.* total internal reflection), so Q_r is infinite. But at discrete points inside the light cone, Q_r also goes to infinity. **e,** Electric-field profile E_z of the trapped state, plotted on the $y = 0$ slice. **f, g,** Amplitudes of the *s*- and *p*-polarized outgoing planewaves for the TM_1 band, with c_p along the Γ-X direction shown in **g**. Black circles in **f** indicate k points where both c_s and c_p are zero.

3.3 Zero crossing of radiation amplitudes

To understand this unexpected disappearance of leakage, we examine the outgoing planewaves. Using Bloch's theorem [80], we let the electric and magnetic fields of the resonance be $\mathbf{E}_\mathbf{k}(\boldsymbol{\rho}, z) = e^{i\mathbf{k}\cdot\boldsymbol{\rho}}\mathbf{u}_\mathbf{k}(\boldsymbol{\rho}, z)$ and $\mathbf{H}_\mathbf{k}(\boldsymbol{\rho}, z) = e^{i\mathbf{k}\cdot\boldsymbol{\rho}}\mathbf{v}_\mathbf{k}(\boldsymbol{\rho}, z)$ where $\mathbf{k} = (k_x, k_y, 0)$, and $\mathbf{u}_\mathbf{k}$, $\mathbf{v}_\mathbf{k}$ are periodic functions in $\boldsymbol{\rho} = (x, y)$. Outside of the slab, these fields are composed of planewaves that propagate energy and evanescent waves that decay exponentially. For frequencies below the diffraction limit, the only propagating-wave amplitudes are the zeroth-order Fourier coefficients, given by

$$c_s(\mathbf{k}) = \langle \hat{\mathbf{e}}_\mathbf{k} \cdot \mathbf{u}_\mathbf{k} \rangle, \quad c_p(\mathbf{k}) = \langle \hat{\mathbf{e}}_\mathbf{k} \cdot \mathbf{v}_\mathbf{k} \rangle \tag{3.1}$$

for s and p polarizations respectively, where $\hat{\mathbf{e}}_\mathbf{k} = (k_y, -k_x, 0)/|\mathbf{k}|$ is the polarization direction of the in-plane fields, and the brackets denote spatial average on some x-y plane outside of the slab. The outgoing power from the resonance is proportional to $(|c_s|^2 + |c_p|^2)\cos\theta$, with θ being the angle of propagation. In general, c_s and c_p are two non-zero complex numbers, with a total of *four* degrees of freedom: therefore the outgoing power is unlikely to be zero when only two parameters (k_x and k_y) are varied.

However, for a certain class of geometries, the degrees of freedom can be reduced. If the structure has time-reversal symmetry $\epsilon(\mathbf{r}) = \epsilon^*(\mathbf{r})$ and inversion symmetry $\epsilon(\mathbf{r}) = \epsilon(-\mathbf{r})$, then the periodic part of the fields can be chosen to satisfy $\mathbf{u}_\mathbf{k}(\mathbf{r}) = \mathbf{u}^*_\mathbf{k}(-\mathbf{r})$ and $\mathbf{v}_\mathbf{k}(\mathbf{r}) = \mathbf{v}^*_\mathbf{k}(-\mathbf{r})$ (Ref. [84]). If the structure also has a mirror symmetry in z direction, then the fields must transform as ± 1 under mirror flips in z (Ref. [80]), so the plane-parallel components must satisfy $\mathbf{u}^\parallel_\mathbf{k}(x, y, z) = \pm\mathbf{u}^\parallel_\mathbf{k}(x, y, -z)$ and $\mathbf{v}^\parallel_\mathbf{k}(x, y, z) = \mp\mathbf{v}^\parallel_\mathbf{k}(x, y, -z)$. Following these two properties, the amplitudes c_s and c_p must be purely

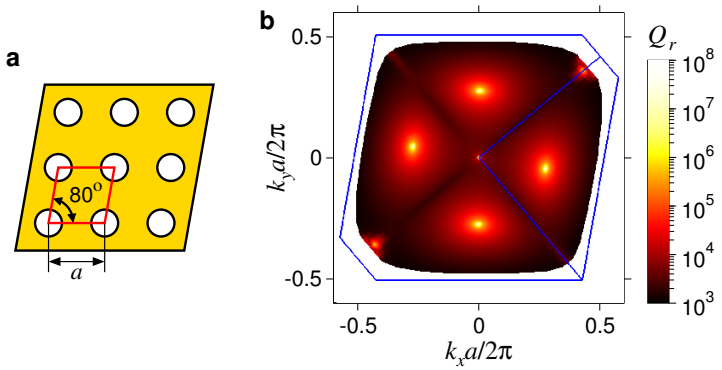

Figure 3.2: Existence of infinite-Q_{r} state in a rhombic-lattice photonic crystal slab. **a,** The lattice viewed from above, with the unit cell framed in red. **b,** Lifetime of the TM_1 band. Compared to the square-lattice case (Figure 3.1c in main text), the special trapped states simply shift to different k points. Blue lines indicate the boundary of the first Brillouin zone and the irreducible Brillouin zone. On a rhombic lattice, C_4 rotational symmetry is broken, but the structure still has inversion symmetry and C_2 rotational symmetry.

real or purely imaginary numbers on every k point. With only *two* degrees of freedom left, it may be possible that the two amplitudes cross zero simultaneously as two parameters k_x and k_y are scanned. A simultaneous crossing at zero means no outgoing power, and therefore, a perfectly confined state. We note that such an "accidental" crossing is distinct from those where leakage is forbidden due to symmetry incompatibility between the confined mode and the radiation modes [162, 108].

This disappearance of leakage may also be understood as the destructive interference between several leakage channels. The field profile inside the PhC slab can be written as a superposition of waves with different propagation constants β_z in z direction. At the slab-medium interface, each wave partially reflects back into the slab, and partially transmits into the medium to become an outgoing planewave. The transmitted waves from different β_z channels interfere, and at appropriate k points they may cancel each other. One can make this argument quantitative by writing down the corresponding

equations, yet because this argument ignores the existence of evanescent waves, it is intrinsically an approximation that works best for slabs much thicker than the wavelength [163]. Nonetheless, this argument provides an intuitive physical picture that supplements the exact (yet less intuitive) mathematical proof given above.

With FDTD simulations, we confirm that both Fourier amplitudes are zero at the k points where the special trapped state is observed (Figure 3.1f, g). The zeros of c_s on the two axes and the zeros of c_p on the diagonal lines arise from symmetry mismatch, but the zeros of c_p along the roughly circular contour are "accidental" crossings that would not be meaningful if c_p had both real and imaginary parts. We have checked that a frequency-domain eigenmode solver [84] also predicts planewave amplitudes that cross zero at these k points.

The trapped state is *robust*, because small variations of the system parameters (such as cylinder diameter) only move the crossing to a different value of k_x. This robustness is crucial for our experimental realization of such states. In fact, the trapped state persists even when the C_4 rotational symmetry of the structure is broken, as shown in Figure 3.2. However, perturbations that break inversion or mirror symmetry will introduce additional degrees of freedom in the Fourier amplitudes, thus reducing the infinite-lifetime bound state into a long-lived leaky resonance unless additional tuning parameters are used; this is shown in Figure 3.3.

3.4 Fabrication and Measurement Setup

To experimentally confirm the existence of this trapped state, we use interference lithography to fabricate a macroscopic Si_3N_4 PhC slab ($n = 2.02$, thickness 180 nm) with a square array of cylindrical holes (periodicity 336 nm, hole diameter 160 nm), separated

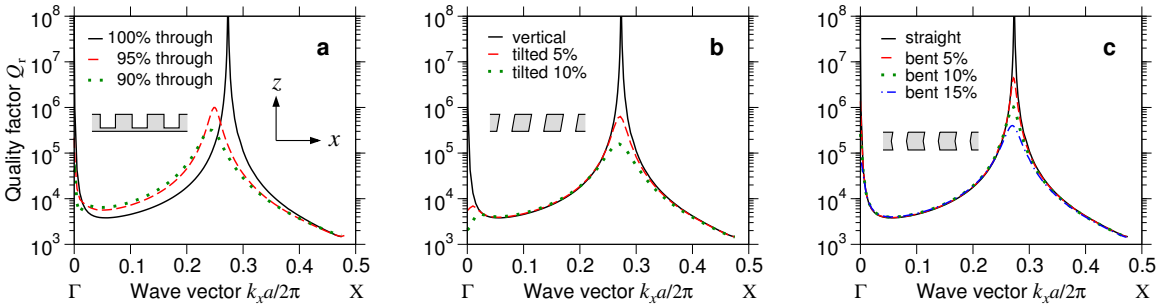

Figure 3.3: Dependence of the TM_1 band lifetime on perturbations that break inversion symmetry I or mirror-flip symmetry σ_z. a, Square-lattice photonic crystal slab with cylindrical holes that are not etched through the entire slab. Both I and σ_z are broken. **b,** Slab with tilted cylindrical holes. σ_z is broken but I is intact. **c,** Slab with cylindrical holes that are bent in the middle. I is broken but σ_z is intact.

from the lossy silicon substrate with 6 μm of silica (Figure 3.4a). Scanning electron microscope (SEM) images of the sample are shown in Figure 3.4b, c. The material Si_3N_4 provides low absorption and enough index contrast with the silica layer ($n = 1.46$). To create an optically symmetric environment needed to reduce the degrees of freedom in the outgoing-wave amplitudes, we etch the holes through the entire Si_3N_4 layer, and immerse the sample in an optical liquid that is index-matched to silica.

The Si_3N_4 layer was grown by LPCVD on top of 6 μm thermally grown SiO_2 on a silicon wafer (LioniX), and subsequently coated with antireflection coating, a SiO_2 intermediate layer, and negative photoresist. The periodic PhC pattern was created with Mach-Zehnder interference lithography using a 325 nm He/Cd laser. Two orthogonal exposures defined the two-dimensional pattern. The interference angle was chosen for periodicity 336 nm, and the exposure time chosen for hole diameter 160 nm. After exposures, the sample was developed, and the pattern was transferred from photoresist to Si_3N_4 by reactive-ion etching; CHF_3/O_2 gas was used to etch SiO_2 and Si_3N_4, and He/O_2 gas was used to etch the antireflection coating. More details on the fabrication

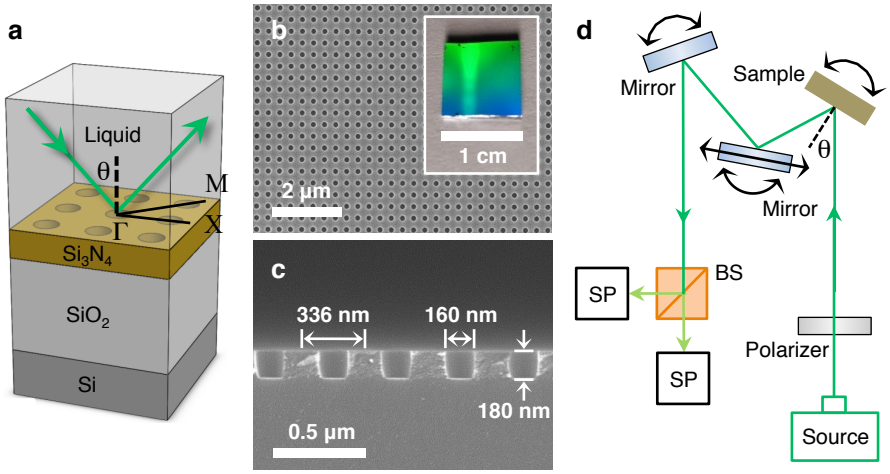

Figure 3.4: Fabricated PhC slab and the measurement setup. **a** Schematic layout of the fabricated structure. The device is immersed in a liquid, index-matched to silica at 740 nm wavelength. **b, c,** SEM images of the structure in top view and side view. Inset of **b** shows an image of the whole PhC. **d,** Schematic of the setup for reflectivity measurements. BS, beamsplitter; SP, spectrometer.

can be found in Ref. [109].

We perform angle-resolved reflectivity measurements (schematic setup shown in Figure 3.4d) to characterize the PhC sample. The source was a supercontinuum laser (SuperK Compact, NKT Photonics) with divergence angle 6×10^{-4} radian and beam-spot width 2 mm on the PhC sample at normal incidence. A polarizer selected p-polarized light, which coupled with the TM_1 band. To create σ_z symmetry, the sample was immersed in a colorless liquid with index $n = 1.454$ at 740 nm (Cargille Labs). The sample was mounted on two perpendicular motorized rotation stages: one oriented the PhC to the Γ-X direction, while the other scanned the incident angle θ. The reflected beam was split into two and collected by two spectrometers, each with a resolution of 0.05 nm (HR4000, Ocean optics). Measurements were made every 0.5° from normal incidence to 60°.

3.5 Detecting Bound States from Reflectivity

Light incident on the PhC slab excites the guided resonances, creating sharp Fano features in the reflectivity spectrum [41]. In comparison, a perfect bound state has no Fano feature, because it is decoupled from far-field radiation. In the measured reflectivity spectrum (Figure 3.5a), we indeed observe that the Fano feature of the TM_1 band disappears near 35°. The measurements agree well with the theory prediction, shown in Figure 3.5b, with the resonance wavelengths between the two differing by less than 2 nm. The measured Fano features are slightly broader than predicted, due to inhomogeneous broadening (since the measured data are averaged over many unit cells) and scattering loss introduced by disorders.

To be more quantitative, we extract the resonance lifetimes from the Fano features. This requires the temporal coupled-mode theory, which we describe in the next section.

3.6 Coupled-mode Theory and Fitting

In temporal coupled-mode theory (CMT), the field A of the resonance and fields $s_{m\pm}$ of the incoming/outgoing planewaves are considered separate entities that are weakly coupled to each other through their spatial overlaps [80, 66]. A schematic illustration is given in Figure 3.5c. The resonance decays with a radiative-decay lifetime τ_{r} from leakage into the outgoing planewaves, and a non-radiative-decay lifetime τ_{nr} from material absorption and disorder scattering. As we will see, the effect of τ_{nr} is to broaden the resonance feature in the reflectivity spectrum; therefore it also heuristically accounts for the inhomogeneous broadening in the measured reflectivity data. Incoming planewaves

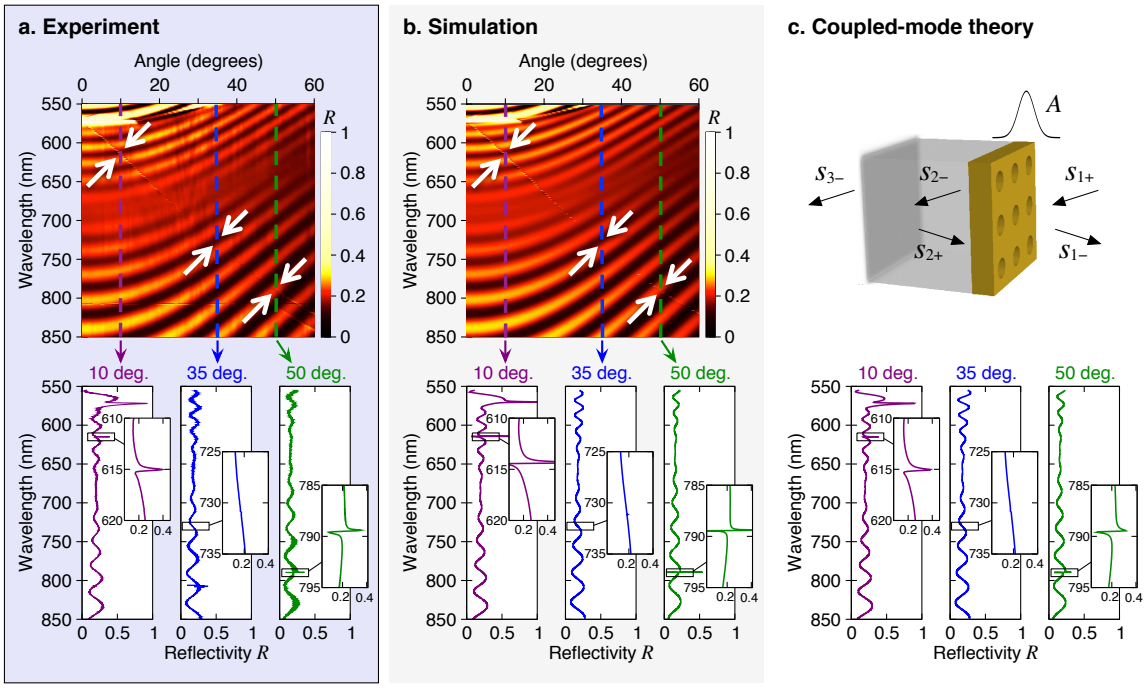

Figure 3.5: Detection of resonances from reflectivity data. a, Experimentally measured specular reflectivity for p-polarized light along Γ-X. The crucial feature of interest is the resonance, which shows up as a thin faint line (emphasized by white arrows) extending from the top-left corner of the top panel to the bottom-right corner. Disappearance of the resonance feature near 35° indicates a trapped state with no leakage. Bottom panel shows slices at three representative angles, with close-ups near the resonance features. **b,** Calculated p-polarized specular reflectivity using the rigorous coupled-wave analysis (RCWA) method [114] with known refractive indices and measured layer thickness. **c,** Top: schematic for the scattering process in temporal coupled-mode theory (CMT), which treats the resonance A and the incoming/outgoing planewaves $s_{m\pm}$ as separate entities weakly coupled to each other. Bottom: reflectivity given by the analytical CMT expression; the resonance frequency and lifetimes, which are the only unknowns in the CMT expression, are fitted from the experimental data in **a**.

excite the resonance with coupling coefficients denoted by κ_1 and κ_2. Thus we have

$$\frac{dA}{dt} = \left(-i\omega_0 - \frac{1}{\tau_\mathrm{r}} - \frac{1}{\tau_\mathrm{nr}}\right) A + \kappa_1 s_{1+} + \kappa_2 s_{2+}. \tag{3.2}$$

The planewaves on the two sides of the slab couple to each other through a direct scattering process, with transmission and reflection coefficients t_slab and r_slab. The resonance decays into the outgoing planewaves, with coupling coefficients denoted by d_1 and d_2. Therefore,

$$\begin{aligned} s_{1-} &= r_\mathrm{slab} s_{1+} + t_\mathrm{slab} s_{2+} + d_1 A, \\ s_{2-} &= t_\mathrm{slab} s_{1+} + r_\mathrm{slab} s_{2+} + d_2 A. \end{aligned} \tag{3.3}$$

Lastly, the reflection at the silica-silicon interface (with coefficient r_{23}) and the propagation inside the silica layer impose that

$$s_{2+} = e^{2i\beta h_2} r_{23} s_{2-} \tag{3.4}$$

where $\beta = \sqrt{n_{\mathrm{SiO}_2}^2 \omega^2/c^2 - |\mathbf{k}|^2}$ is the propagation constant in the silica layer, and h_2 is the layer's thickness. The normalization of the field amplitudes is chosen such that $|A|^2$ is the energy stored in the resonance, and $|s_{m\pm}|^2$ is the power carried by the incoming or outgoing planewaves.

Now, assume $e^{-i\omega t}$ time dependence for the resonance amplitude A. Solving equations (1–4) as a system of linear equations, we obtain

$$\frac{s_{1-}}{s_{1+}} = r_\mathrm{slab} + \frac{d_1\kappa_1}{i(\omega_0-\omega) + \tau_\mathrm{r}^{-1} + \tau_\mathrm{nr}^{-1}} + \frac{\left[t_\mathrm{slab} + \frac{d_1\kappa_2}{i(\omega_0-\omega)+\tau_\mathrm{r}^{-1}+\tau_\mathrm{nr}^{-1}}\right]\left[t_\mathrm{slab} + \frac{d_2\kappa_1}{i(\omega_0-\omega)+\tau_\mathrm{r}^{-1}+\tau_\mathrm{nr}^{-1}}\right]}{e^{-2i\beta h_2} r_{23}^{-1} - r_\mathrm{slab} - \frac{d_2\kappa_2}{i(\omega_0-\omega)+\tau_\mathrm{r}^{-1}+\tau_\mathrm{nr}^{-1}}} \tag{3.5}$$

which gives us the overall reflectivity. This expression can be simplified, as follows.

First, σ_z mirror-flip symmetry of the PhC slab requires fields of the resonance to be either even or odd in z, and so $d_2 = \pm d_1$. Secondly, energy conservation requires that in the absence of input power ($s_{1+} = s_{2+} = 0$), the energy dissipated through radiative decay must be carried away by s_{1-} and s_{2-}; this leads to $|d_1|^2 = 1/\tau_\mathrm{r}$. Thirdly, inversion symmetry I and σ_z mirror symmetry yields $I\sigma_z = C_2$ rotational symmetry about the plane normal, and a combination of time reversal symmetry and C_2 symmetry leads to $r_\mathrm{slab} d_1^* + t_\mathrm{slab} d_2^* + d_1 = 0$ (Refs. [71, 42]). A combination of these facts yields

$$d_1^2 = -\frac{1}{\tau_\mathrm{r}}(r_\mathrm{slab} \pm t_\mathrm{slab}). \tag{3.6}$$

Lastly, the coupling coefficients for the incoming and for the outgoing waves are actually the same under energy conservation and time reversal requirements [80, 66, 42], *i.e.* $d_1 = \kappa_1$ and $d_2 = \kappa_2$. With these known properties, we can write the overall reflectivity as

$$R = \left|\frac{s_{1-}}{s_{1+}}\right|^2 = \left| r_\mathrm{slab} - f(\omega) + \frac{[t_\mathrm{slab} \mp f(\omega)]^2}{e^{-2i\beta h_2} r_{23}^{-1} - r_\mathrm{slab} + f(\omega)} \right|^2 \tag{3.7}$$

with

$$f(\omega) = \frac{Q_\mathrm{r}^{-1}}{2i(1-\omega/\omega_0) + Q_\mathrm{r}^{-1} + Q_\mathrm{nr}^{-1}} \left(r_\mathrm{slab} \pm t_\mathrm{slab}\right), \tag{3.8}$$

where $Q_\mathrm{r} = \omega_0 \tau_\mathrm{r}/2$ and $Q_\mathrm{nr} = \omega_0 \tau_\mathrm{nr}/2$ are the normalized lifetimes. This is the expression we use to extract the lifetime of the resonances from the experimentally measured reflectivity spectrum.

We note that, the only unknowns in this reflectivity expression are the resonance frequency and the lifetimes: r_{23} is given by the Fresnel equations, and r_slab, t_slab can be approximated as the reflection and transmission coefficients of a homogeneous slab whose permittivity is equal to the spatial average of the PhC slab [41, 42].

In the absence of $f(\omega)$, equation (7) reduces to the expression for multi-layer thin-film reflectivity. Therefore the Fano features are completely captured by $f(\omega)$. From equation (8), we see that the width of the Fano feature is proportional to $Q_{\mathrm{r}}^{-1} + Q_{\mathrm{nr}}^{-1}$, while the height of the feature grows with Q_{r}^{-1}. This confirms our intuitive understanding that, when the resonance becomes a bound state ($Q_{\mathrm{r}} = \infty$), it decouples from the far field, and the Fano feature disappears.

It is straightforward to generalize this CMT expression to include multiple resonances in the spectrum; same derivation shows that we can simply replace $f(\omega)$ in equation (7) with a summation $\sum_j f^{(j)}(\omega)$ for different resonances labeled by j. Each resonance has its resonant frequency and lifetimes that are to be determined from the fitting. Lastly, we note that the $\pm$ signs relate to how the resonance fields transform under mirror flips in z. When the electric field is used to determine the phase of A and $s_{m\pm}$, we should read the upper signs for TE-like modes, lower signs for TM-like modes.

3.7 Resonance Lifetimes

The only unknowns in the CMT reflectivity expression are the resonance frequency and the lifetimes, which we obtain by fitting to the measured reflectivity spectrum. The fitted curves are shown in the bottom panel of Figure 3.5c; we see very good agreement between the original data and the fitted curves, confirming the validity of the CMT expression.

The obtained radiative Q_{r} is shown in Figure 3.6a. At around 35°, Q_{r} reaches 1,000,000, near the instrument limit imposed by the resolution and signal-to-noise ratio, and in a good agreement with the values calculated from FDTD. For validation, we also repeat the same fitting procedure for the simulated reflectivity spectrum, and confirm

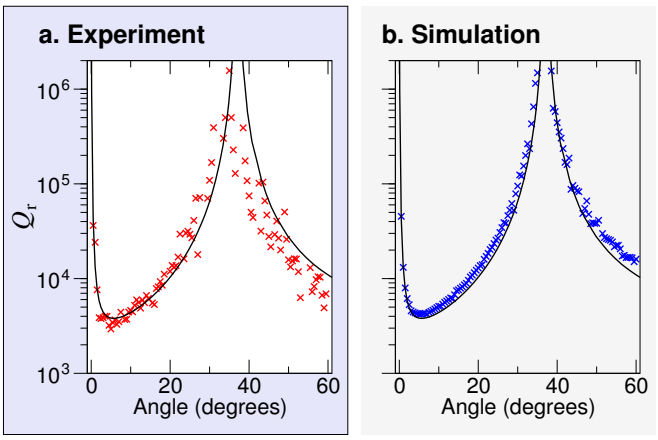

Figure 3.6: Quantitative evidence on the disappearance of leakage. a, b, Normalized radiative lifetime Q_r extracted from the experimentally-measured reflectivity spectrum (**a**) and the RCWA-calculated reflectivity spectrum (**b**). Black solid line shows prediction from FDTD.

that consistent theoretical estimates of Q_r are obtained (Figure 3.6b). These evidences quantitatively verify that we have observed the predicted bound state of light.

Our analysis so far assumes excitation with a perfect planewave. However, some care must be taken with the Gaussian beam from the supercontinuum source. First, the beam spot has a diameter of 2 mm at normal incidence, so the excited mode has a finite lateral size of $L \approx 2$ mm. This finite-sized mode consists of a spread of k points, with $\delta k_{\text{mode}} \approx 2\pi/L \approx (2 \times 10^{-4})(2\pi/a)$. Second, the beam has a divergence angle of $\delta\theta \approx 6 \times 10^{-4}$ radian, so the source also has a spread of k points, with $\delta k_{\text{source}} \approx (2\pi/\lambda)\delta\theta \approx (3 \times 10^{-4})(2\pi/a)$. The measured radiative loss will be the averaged value within this spread of k points.

The outgoing-wave amplitude goes through zero linearly (see Figure 3.1g of the main text), so the outgoing power goes as $(\Delta k)^2$ near the embedded bound states, where $\Delta k = |\mathbf{k} - \mathbf{k}_0|$ is distance from the special k point, $\mathbf{k}_0$. Specifically, FDTD simulations show that near the special trapped state studied in this paper, $Q_r \approx 100/(\Delta k a/2\pi)^2$.

In a circular area with diameter δk, the effective Q_{r} will be $800/(\delta k a/2\pi)^2$, which is around 10^{10} for the k-point spread due to the beam. This sets the upper limit on the Q_{r} we can obtain with our source. In this experiment, this is not the limiting factor for the measured Q_{r}. In comparison, the non-radiative Q_{nr} is limited to about 10^4 which is due to loss from material absorption, disorder scattering, in-plane lateral leakage, and inhomogeneous broadening.

3.8 Conclusions

We have observed an optical state that remains perfectly confined even though there exist symmetry-compatible radiation modes in its close vicinity; this realizes the long sought-after idea of trapping waves within the radiation continuum, without symmetry incompatibility [229, 220, 137, 201, 49, 244, 124, 71, 163, 111, 102]. The state has a high quality factor (implying low loss and large field enhancement), large area, and strong confinement near the surface, making it potentially useful for chemical/biological sensing, organic light emitting devices, and large-area laser applications. It also has wavevector and wavelength selectivity, making it suitable for optical filters, modulators, and waveguides. Furthermore, the ability to tune the maximal radiative Q_{r} from infinite to finite (Figure 3.3) is another unique property that may be exploited. Lastly, the fundamental principles of this state hold for any linear wave phenomenon, not just optics.

Chapter 4

Topological nature of optical bound states in the continuum*

4.1 Introduction

Bound states in the continuum (BICs) are unusual solutions of wave equations describing light or matter: they are discrete and spatially bounded, but exist at the same energy as a continuum of states which propagate to infinity. Until recently, BICs were constructed through fine-tuning parameters in the wave equation [220, 49, 19, 137, 29, 230, 196, 138] or exploiting the separability of the wave equation due to symmetry [39, 190, 135, 162, 108]. More recently, BICs that that are both robust and not symmetry-protected ("accidental") have been predicted [200, 163, 124, 115, 71, 72] and experimentally realized [72] in extended structures; the simplest such system is a periodic dielectric slab [72], which also has symmetry-protected BICs. Here we show that both types of BICs in such systems are vortex centers in the polarization direction of far-field radiation. The robustness of these BICs is due to the existence of conserved and quantized topological charges, defined by the number of times the polarization vectors

*This chapter is based on: B. Zhen†, C. W. Hsu†, L. Lu, A. D. Stone, M. Soljačić, "Topological nature of optical bound states in the continuum," *Phys. Rev. Lett.*, accepted (2014) arXiv:1408.0237 [†equal contribuation].

wind around the vortex centers. Such charges can only be generated or annihilated by making large changes in the system parameters, and then only according to strict rules, which we derive and test numerically. Our results imply that laser emission based on such states will generate vector beams [243].

These BICs exist in photonics crystal slabs, which are dielectric slabs with a periodic modulation of refractive index at the wavelength scale [80] surrounded by air or a low-index medium. Photonic crystal slabs are used in many applications including surface-emitting lasers [68], photovoltaics [99], LEDs [233], and biosensing [52, 241, 246]. The periodic modulation alters the dispersion relation of light in the slabs and gives rise to photonic bands, analogous to electronic band structures in solids. In general light can escape from the surface of the slab and propagate to the far-field, but for a portion of the photonic band (that is "below the light line") light is perfectly confined to the slab by the generalized form of total internal reflection [80]. In contrast, modes above the light line appear generically as resonances with finite lifetimes due to their coupling to the continuum of extended modes [41]. It has been known for some time that bound states with infinite lifetimes also exist *above* the light line at isolated high-symmetry wavevectors. This type of BIC arises from the symmetry mismatch between their mode profiles inside the photonic crystal and those of the external propagating modes (radiation continuum) [153, 149, 41, 108]. Recently, a new type of BIC, unprotected by symmetry, has been found (both theoretically and experimentally) to exist at arbitrary wavevectors in bands above the light line in photonic crystal slabs [72]. These BICs occur "accidentally", when the relevant couplings to the continuum (see below) all vanish simultaneously. However their existence does not require fine-tuning of system parameters; small changes in parameters simply shift the position of these special points along the band diagram. An intuitive understanding of why such BICs exist and are

robust was previously lacking. Recently, an explanation based on accidental triangular symmetry of the radiating fields was proposed [240] but does not explain the robustness of these BICs and their occurrences in TE-like bands.

4.2 Vortex Centers

We now show that both types of BICs in photonic crystal slabs are vortex centers in the polarization direction of the far-field radiation of the slabs. Using the Bloch theorem for photonic crystals [80], we write the electric field of a resonance as $\mathbf{E}_{\mathbf{k}}(\boldsymbol{\rho}, z) = e^{i\mathbf{k}\cdot\boldsymbol{\rho}}\mathbf{u}_{\mathbf{k}}(\boldsymbol{\rho}, z)$, where $\mathbf{k} = k_x\hat{x} + k_y\hat{y}$ is the two-dimensional wave vector, $\boldsymbol{\rho} = x\hat{x} + y\hat{y}$ is the in-plane coordinate, $\mathbf{u}_{\mathbf{k}}$ is a periodic function in $\boldsymbol{\rho}$, and z is the normal direction to the slab. While the fields inside the slab are periodically modulated, outside the slab each state consists of propagating plane waves and/or evanescent waves that decay exponentially away from the surface. For states above the light line (resonances), and wavelengths below the diffraction limit, the only non-zero propagating-wave amplitudes are the zero-order (constant in-plane) Fourier coefficients of $\mathbf{u}_{\mathbf{k}}$, given by $\mathbf{c}(\mathbf{k}) = c_x(\mathbf{k})\hat{x} + c_y(\mathbf{k})\hat{y}$ (Figure 4.1a). Here, $c_x(\mathbf{k}) = \hat{x}\cdot\langle\mathbf{u}_{\mathbf{k}}\rangle$, $c_y(\mathbf{k}) = \hat{y}\cdot\langle\mathbf{u}_{\mathbf{k}}\rangle$, and the brackets denote spatial average over one unit cell on any horizontal plane outside the slab. Note that $\mathbf{c}(\mathbf{k})$ is the projection of $\langle\mathbf{u}_{\mathbf{k}}\rangle$ onto the x-y plane; it points in the polarization direction of the resonance in the far field, so we refer to $\mathbf{c}(\mathbf{k})$ as the "polarization vector".

A resonance turns into a BIC when the outgoing power is zero, which happens if and only if $c_x = c_y = 0$. In general, c_x and c_y are both complex functions of $\mathbf{k}$, and varying the wave vector components (k_x, k_y) is not sufficient to guarantee a solution where $c_x = c_y = 0$. However, when the system is invariant under the operation $C_2^z T$, implying that $\epsilon(x, y, z) = \epsilon^*(-x, -y, z)$, we show in the next section that c_x and c_y can

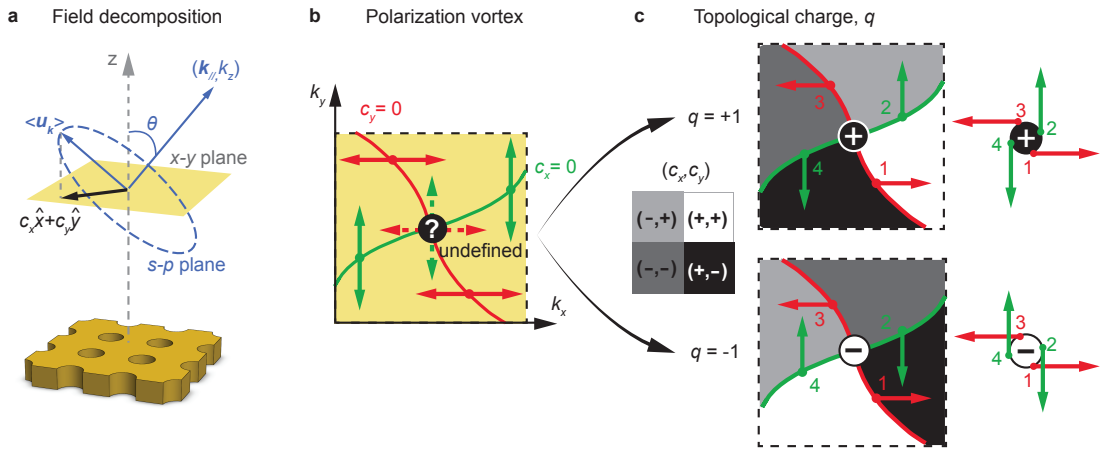

Figure 4.1: Stable bound states in the continuum (BICs) as vortex centers of polarization vectors. **a**, Schematics of radiation field decomposition for resonances of a slab structure. The spatially-averaged Bloch part of the electric field $\langle \boldsymbol{u_k} \rangle$ is projected onto the x-y plane as the polarization vector $\boldsymbol{c} = (c_x, c_y)$. A resonance turns into a BIC if and only if $c_x = c_y = 0$. **b**, Schematic illustration for the nodal lines of c_x (green) and of c_y (red) in a region of **k** space near a BIC. The direction of vector $\boldsymbol{c}$ (shown in arrows) becomes undefined at the nodal line crossing, where a BIC is found. **c**, Two possible configurations of the polarization field near a BIC. Along a closed loop in k-space containing a BIC (loop goes in counterclockwise direction, 1→2→3→4), the polarization vector either rotates by angle 2π (denoted by topological charge $q = +1$) or rotates by angle -2π (denoted by topological charge $q = -1$). Different regions of the k space are colored in four gray-scale colors according to the signs of c_x and c_y. In this way, a BIC happens where all four gray-scale colors meet, and charge $q = +1$ corresponds to the color changing from white to black along the counterclockwise loop C, and charge $q = -1$ corresponds to the color changing from black to white.

be chosen to be real numbers simultaneously; in other words, the far field is linearly polarized (here C_2^z is 180° rotation operator around z axis, and T is the time reversal operator). When the system also has up-down mirror symmetry (σ_z), the outgoing waves on one side of the slab determine those on the other; for such systems, BICs are stable because they correspond to the intersections between the nodal line of c_x and the nodal line of c_y in the k_x-k_y plane. Such a nodal intersection naturally causes a vortex in the polarization vector field centered on the BIC, as illustrated in Figure 4.1b, for the simplest case. Along the nodal line of c_x (or c_y), the direction of $\mathbf{c}(\mathbf{k})$ is along the y axis (or x axis), as illustrated in Figure 4.1b. As one encircles the nodal intersection (BIC) in the k_x-k_y plane each component of the polarization vector flips sign as its nodal line is crossed so as to create a net circulation of $\pm 2\pi$ in the polarization field. At the nodal intersection the polarization direction becomes undefined, since at the BIC there is zero emission into the far-field. Conversely one could say that BICs cannot radiate because there is no way to assign a far-field polarization that is consistent with neighbouring $\mathbf{k}$ points. Thus robust BICs are only possible when there is vorticity in the polarization field.

4.3 Symmetry requirements for stable BICs

Here, we give the proof that stable BICs at arbitrary k points can be found when the system is invariant under $C_2^z T$ and σ_z operators, and that stable BICs at C_2^z-invariant k points can be found when the system has C_2^z symmetry. Here, C_2^z means 180° rotation around z axis, and T means the time reversal operator. The schematics of the symmetry requirement is summarized in Figure 4.2.

In region *I*, systems are invariant under the symmetry operator $C_2^z T$, namely

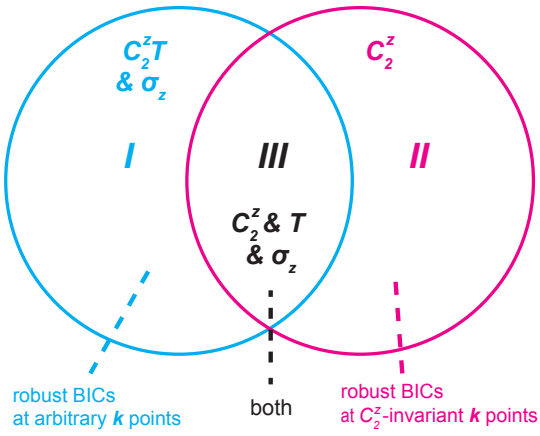

Figure 4.2: Symmetry requirements for BICs. Systems in the blue circle are invariant under operators C_2^zT and σ_z, where stable BICs at arbitrary wavevectors can be found. In the red circle, where C_2^z is a symmetry of the system, robust BICs can be found at high-symmetry wavevector points. Here, high-symmetry wavevectors mean C_2^z-invariant ones, while arbitrary wavectors are not necessarily C_2^z-invariant. In the overlapping area (region *III*), both types BICs can be found. All numerical examples in this Letter are within region *III*.

$\epsilon^\star(x,y,z) = \epsilon(-x,-y,z)$. Let $\mathbf{u_k}$ be an eigenfunction of the master operator [80] $\Theta_\mathbf{k} = \frac{1}{\epsilon}(\nabla + i\mathbf{k}) \times (\nabla + i\mathbf{k})\times$, and recall that $\mathbf{k}$ here only has x and y components since we are considering a slab structure that does not have translational symmetry in z. A short derivation shows that at any $\mathbf{k}$ point, $\mathbf{u_k}(\mathbf{r})$ and $C_2^z\mathbf{u}_\mathbf{k}^*(C_2^z\mathbf{r})$ are both eigenfunctions of $\Theta_\mathbf{k}(\mathbf{r})$ with the same eigenvalue, so they must differ at most by a phase factor,

$$\begin{aligned} \mathbf{u_k}(\mathbf{r}) &= e^{i\theta_\mathbf{k}} C_2^z \mathbf{u}_\mathbf{k}^*(C_2^z\mathbf{r}) \\ &= e^{i\theta_\mathbf{k}}(-\mathbf{u}_\mathbf{k}^{x*}, -\mathbf{u}_\mathbf{k}^{y*}, \mathbf{u}_\mathbf{k}^{z*})|_{(-x,-y,z)} \end{aligned} \tag{4.1}$$

Here $\theta_\mathbf{k}$ is an arbitrary phase factor. Meanwhile, we are free to multiply $\mathbf{u_k}$ with any

phase factor, and it remains a valid eigenfunction. For our purpose here, we explicitly choose the phase factor of $\mathbf{u_k}$ such that $e^{i\theta_\mathbf{k}} = -1$ for all $\mathbf{k}$. With this choice, we can average over x and y to get $\mathbf{c}(\mathbf{k}) = \mathbf{c}^*(\mathbf{k})$ for all $\mathbf{k}$. That is, the polarization vector $\mathbf{c}(\mathbf{k})$ is purely real.

Using the fact that systems in region I also have the up-down mirror symmetry σ_z, namely $\epsilon(x, y, z) = \epsilon(x, y, -z)$, we can link the radiation loss above and below the photonic crystal slab denoted by $\mathbf{c}^\uparrow$ and $\mathbf{c}^\downarrow$. At any $\mathbf{k}$ point, $\mathbf{u_k}(\mathbf{r})$ and $\sigma_z\mathbf{u_k}(\sigma_z\mathbf{r})$ are both eigenfunctions of $\Theta_\mathbf{k}(\mathbf{r})$ with the same eigenvalue, so

$$\begin{aligned} \mathbf{u_k}(\mathbf{r}) &= e^{i\psi_\mathbf{k}}\sigma_z\mathbf{u_k}(\sigma_z\mathbf{r}) \\ &= e^{i\psi_\mathbf{k}}(\mathbf{u}^x_\mathbf{k}, \mathbf{u}^y_\mathbf{k}, -\mathbf{u}^z_\mathbf{k})|_{(x,y,-z)} \end{aligned} \tag{4.2}$$

with $\psi_\mathbf{k}$ being an arbitrary phase factor (not to be confused with the one in Eq. (4.1)). Since $\sigma_z^2 = 1$, we can apply Eq. (4.2) twice to show that $e^{i\psi_\mathbf{k}} = \pm 1$. Averaging over x and y, we see that $\mathbf{c}^\uparrow = \pm\mathbf{c}^\downarrow$.

After using these two symmetries, the number of independent real variables in all radiation coefficients $c^{\uparrow,\downarrow}_{x,y}$ has been reduced from 8 to 2. Given that the number of independent tuning parameters is also 2: (k_x, k_y), we are able to get stable BICs. Note that the combination of C_2^zT and σ_z is just one sufficient condition for stable BICs in photonic crystal slabs. There might be other different choices of symmetries. For example, PT and σ_z is equivalent to C_2^zT and σ_z, where P is the inversion operator. Also, the requirement of σ_z is not necessary when there is leakage to one direction only (such as BICs on the surface of a photonic bandgap structure [71]).

In region *II*, stable BICs at C_2^z-invariant k points can be found. Systems in this region have C_2^z symmetry, namely $\epsilon(x, y, z) = \epsilon(-x, -y, z)$. k points are C_2^z-invariant

when $-\mathbf{k} = \mathbf{k} + \mathbf{G}$, with $\mathbf{G}$ being a reciprocal lattice vector. A short derivation shows that at any k point, $\mathbf{u_k}(\mathbf{r})$ and $C_2^z\mathbf{u}_{-\mathbf{k}}(C_2^z\mathbf{r})$ are both eigenfunctions of $\Theta_\mathbf{k}(\mathbf{r})$ with the same eigenvalue, so

$$\mathbf{u_k}(\mathbf{r}) = e^{i\gamma_\mathbf{k}} C_2^z \mathbf{u}_{-\mathbf{k}}(C_2^z\mathbf{r}), \tag{4.3}$$

with $\gamma_\mathbf{k}$ being an arbitrary phase factor (not to be confused with the two phase factors above). At these high-symmetry $\mathbf{k}$ points, using Bloch theorem we know: $\mathbf{u}_{-\mathbf{k}} = \mathbf{u}_{\mathbf{k}+\mathbf{G}} = \mathbf{u_k}$, so we can apply Eq. (4.3) twice to get $e^{i\gamma_\mathbf{k}} = \pm 1$. When this factor is $+1$, we can average over x and y to see that $\mathbf{c}(\mathbf{k}) = 0$, corresponding to a BIC at this C_2^z-invariant k point.

In region *III*, both kinds of BICs can be found, where C_2^z, T and σ_z are all present. All our numerical examples are within this region to make it easier to understand the relation and interaction between different types of BICs.

4.4 Topological Charge

Vortices are characterized by their topological charges. Here, the topological charge (q) carried by a BIC is defined as:

$$q = \frac{1}{2\pi} \oint_C d\mathbf{k} \cdot \nabla_\mathbf{k} \phi(\mathbf{k}), \quad q \in \mathbb{Z} \tag{4.4}$$

which describes how many times the polarization vector winds around the BIC. Here, $\phi(\mathbf{k}) = \arg[c_x(\mathbf{k}) + ic_y(\mathbf{k})]$ is the angle of the polarization vector, and C is a closed simple path in k space that goes around the BIC in the counterclockwise direction. The fields $\mathbf{u_k}$ are chosen to be smooth functions of $\mathbf{k}$, so $\phi(\mathbf{k})$ is differentiable in $\mathbf{k}$ along the path. The polarization vector has to come back to itself after the closed loop, so the overall

angle change must be an integer multiple of 2π, and q must be an integer. Figure 4.1c shows examples of how the polarization vector winds around a BIC with charge $q = +1$ and also around a BIC with charge $q = -1$ along a loop C marked by 1→2→3→4→1. Similar definitions of winding numbers as in Eq. 1 can be found in describing topological defects [129] of continuous two-dimensional spins, dislocations in crystals, and quantized vortices in helium II [34]. This formalism describing polarization vortices is also closely related to Berry phases in describing adiabatic changes of polarization of light [12] and Dirac cones in gaphenes [122].

The far-field pattern at a definite $\mathbf{k}$ point by itself does not reflect the vorticity of polarization around a BIC, but laser emission centered on such a BIC will. Laser emission always has a finite width in k-space and this wave-packet will be centered on the BIC; hence it will consist of a superposition of plane waves from the neighborhood of the BIC, leading naturally to a spatial twist in the polarization for the outgoing beam. Such beams have been studied previously, and are known as vector beams [243], although their connection with BICs does not appear to have been realized. The number of twists in the polarization direction is known as the order number of the vector beam, and we now see that it is given by the topological charge carried by the BIC. Note that these vector beams are different from optical vortices, which usually have a fixed polarization direction.

In Figure 4.3, we show the topological charges of BICs for the structure we investigate in the previous chapter. In this example, there are five BICs on the lowest-frequency TM-like band as shown in Figure 4.3a. The mode profiles of the z compoenent of the electric field, $\mathbf{E}_z$, for two of the BICs are shown in Figure 4.4. Here, it is clear that these modes are spatially localized in the z direction, not coupling to any radiation. In the x-y plane they are extended Bloch modes, and are therefore integrable within

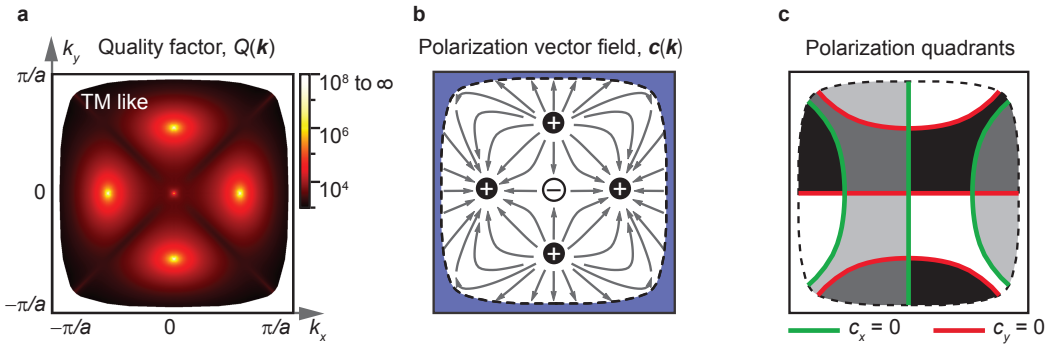

Figure 4.3: Characterization of BICs using topological charges. **a**, Calculated radiative quality factor Q of the TM_1 band on a square-lattice photonic crystal slab (as in ref. 72), plotted in the first Brillouin zone. Five BICs can be seen. **b**, Directions of the polarization vector field reveal vortices with topological charges of ± 1 at each of the five k points. The area shaded in blue indicates modes below the lightline and thus bounded by total internal reflection. **c**, Nodal lines and gray-scale colors of the polarization vector fields (same coloring scheme as in Figure 4.1c).

one unit cell, but not over the entire three-dimensional space. We obtain polarization vectors $\mathbf{c}(\mathbf{k})$ from finite-difference time-domain (FDTD) calculations [152], which reveal five vortices with topological charges of ± 1 at these five k points (Figure 4.3b). As discussed above, the BICs and their topological charges can also be identified from the nodal-line crossings and the gray-scale colors of c_x and c_y (Figure 4.3c).

4.5 Conservation of Topological Charge

The winding number of polarization vector along a closed path is given by the sum of the topological charges carried by all BICs enclosed within this path [129]. When system parameters vary continuously, the winding number defined on this path remains invariant, unless there are BICs crossing the boundary. Therefore, topological charge is a conserved quantity. This conservation rule leads to consequences/restrictions on

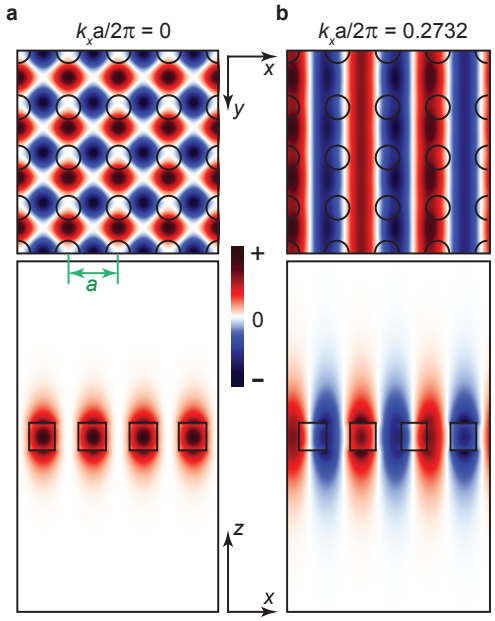

Figure 4.4: Example mode profiles of BICs. a, The mode profiles of the z component of the electric field, $\mathbf{E}_z$, for the BIC at the center of the Brillouin zone shown in Figure 4.3a. The upper part shows a slice of 4×4 unit cells on the x-y plane at the center of the high index layer; while the lower part shows a slice on the $x - z$ plane. The color bar has with arbitrary units. **b,** The mode profiles of $\mathbf{E}_z$ for the BIC on the positive k_x axis in Figure 4.3a. Both modes are spatially localized in the z direction and do not couple to the radiation. Meanwhile, in the x-y plane, they are both extended Bloch modes and are therefore integrable within one unit cell, but not over the entire three-dimensional space.

behaviors of the BICs. For example, as long as the system retains $C_2^z T$ and σ_z symmetries (Figure 4.2), a BIC can only be destroyed through annihilation with another BIC of the exact opposite charge, or through bringing it outside of the continuum (below the light line).

Since topological charge is a conserved quantity, there are a few consequences and restriction on the evolution of BICs. First, BICs are stable as long as the system retains required symmetries; however, perturbations that break these two required symmetries eliminate the existence of BICs. When $C_2^z T$ symmetry is broken, the coefficients (c_x and

c_y) require complex components, meaning the radiation becomes elliptically polarized instead of linearly polarized. When σ_z symmetry is broken, the coefficients $c_{x,y}^{\uparrow,\downarrow}$ are still real numbers, but radiation towards the top and towards the bottom become separate degrees of freedom and so they do not vanish simultaneously in general. Second, when BICs collide into each other in the moment space, the sum of all topological charges they carry remains the same before and after the collision.

4.6 Charge Bouncing

The conservation of topological charges allows us to predict and understand the behaviors of BICs when the parameters of the system are varied over a wide range, as we now illustrate. First, consider the lowest-frequency TM-like mode (TM_1 band) of a 1D-periodic structure in air shown in Figure 4.5a. This grating consists of a periodic array of dielectric bars with periodicity of a, width $w = 0.45a$, and refractive index $n = 1.45$. Its calculated band structure is shown in Figure 4.5b. When the thickness of the grating is $h = 1.50a$, there are two BICs on the k_x axis, as indicated by the radiative quality factor of the resonances (Figure 4.5c). The polarization vector $\mathbf{c}(\mathbf{k})$, also shown in Figure 4.5c, characterizes both BICs as carrying charges $q = +1$. When the grating thickness is decreased to $h/a = 1.43$ (all other parameters fixed), the two BICs move towards the center of the Brillouin zone, meet at the $\mathbf{\Gamma}$ point, and deflect onto the k_y axis (Figure 4.5d). This is inevitable due to the conservation of the topological charges: annihilation cannot happen between two BICs of the same charge.

4.7 Charge Annihilation

Annihilation of BICs is only possible when charges of opposite signs are present. This can be seen in the lowest-frequency TE-like band of the same structure (Figure 4.5e,f). When $h/a = 1.04$, there are two off-$\mathbf{\Gamma}$ BICs with charge -1 and a BIC with charge $+1$ at the $\mathbf{\Gamma}$ point (Figure 4.5e). As h/a decreases, the two -1 charges move to the center and eventually annihilate with the $+1$ charge, leaving only one BIC with charge $q = -1$ (Figure 4.5f).

Figure 4.5 ***(following page)*****: Evolution of BICs and conservation of topological charges.** **a**, Schematic drawing of a photonic crystal slab with one-dimensional periodicity in x and is infinitely long in y. **b**, Calculated TM-like band structure along k_x axis and along k_y axis. The area shaded in yellow indicates the light cone, where there is a continuum of radiation modes in the surrounding medium. **c, d**, An example showing topological charges with the same sign bouncing off each other. As the slab thickness h decreases, the two BICs with charge $+1$ move along the k_x axis, meet at the origin, and then deflect onto the k_y axis. This can be understood from the conservation of topological charges or from the evolution of nodal lines. **e, f**, An example of topological charge annihilation happening on the lowest-frequency TE-like band of the same structure with different slab thicknesses. As the slab thickness h decreases, two BICs with charge -1 meet with a BIC with charge $+1$ at the origin. These three BICs annihilate to yield one BIC with charge -1, as governed by charge conservation.

Figure 4.5: (continued)

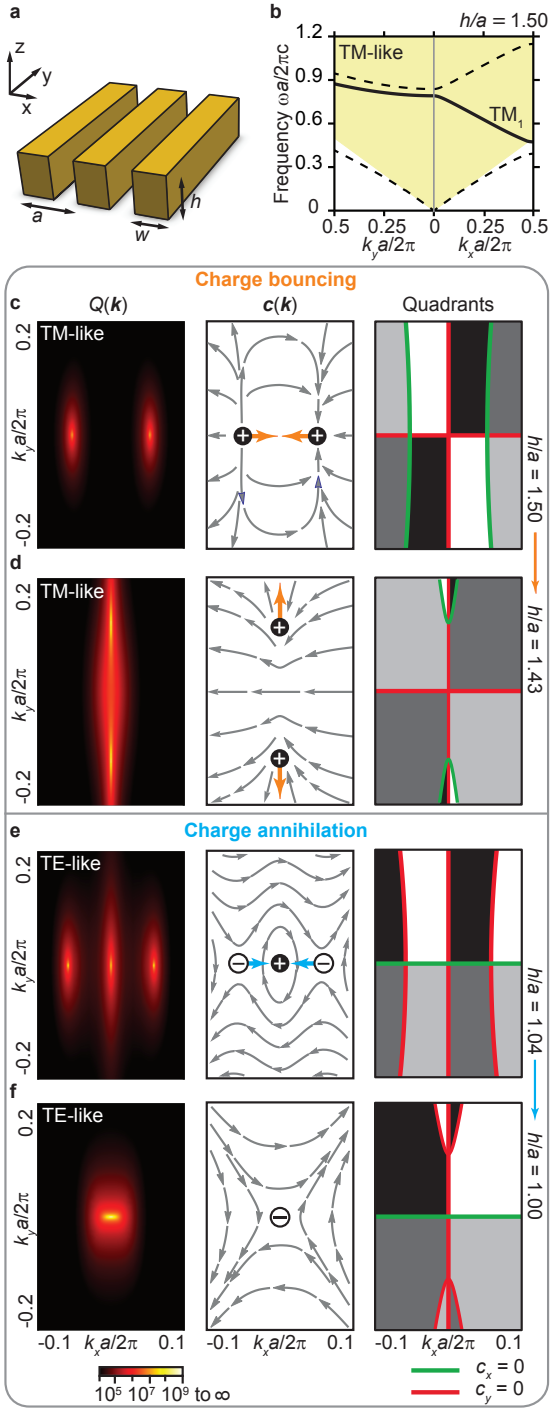

4.8 Charge Generation

Generation of BICs is also restricted by charge conservation, and can be understood as the reverse process of charge annihilation. We provide an example by considering the lowest-frequency TE-like mode in a photonic crystal slab of $n = 3.6$ with a square lattice of cylindrical air holes of diameter $d = 0.5a$ (Figure 4.6a). As shown in Figure 4.6b, As the slab thickness increases, BICs are generated at the $\mathbf{\Gamma}$ point. Each time, four pairs of BICs with exact opposite charges are generated, consistent with charge conservation and C_{4v} symmetry of the structure. With further increase of the slab thickness, the eight BICs move outward along high-symmetry lines and eventually go outside of the continuum (fall below the light line).

4.9 Example of charge -2

Although the examples discussed so far only show topological charges of ± 1, other values of charges can be found in higher-frequency bands of the PhC or in structures with higher rotational symmetry. For example, Figure 4.7 shows a stable BIC of charge -2 at the $\mathbf{\Gamma}$ point arising from the double degeneracy of nodal lines caused by the C_{6v} symmetry of the system.

We consider the lowest-frequency TE-like mode of a photonic crystal slab with a hexagonal lattice of cylindrical air holes (shown in Figure 4.7a). The refractive index of the slab is $n = 1.5$; the air-hole diameter is $0.5a$; and the thickness of the slab is 0.5a, where a is the lattice constant. This system has C_6^z symmetry. Normalized lifetime plot indicates a BIC at the center of the Brillouin zone shown in Figure 4.7b. The polarization vector field characterizes the BIC carrying charge -2 shown in Figure 4.7c.

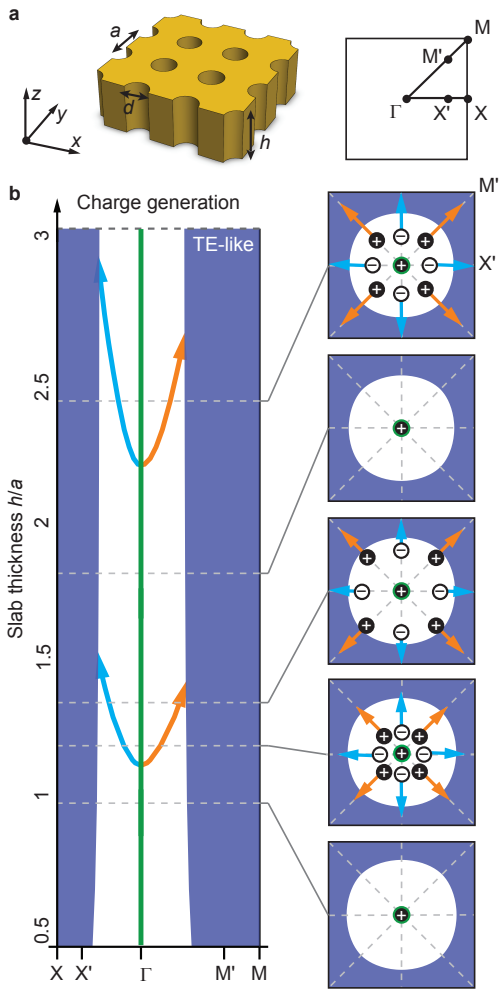

Figure 4.6: Generation of BICs. **a**, Schematic drawing of a photonic crystal slab with two-dimensional periodicity. **b**, Generation of BICs on the TE_1 band when the slab thickness h is increased. Each time, four pairs of BICs with charges ± 1 are generated simultaneously, consistent with the charge conservation and C_{4v} symmetry. Insets show the locations of BICs in the k space and their corresponding topological charges for $h/a = 1.0, 1.2, 1.35, 1.8$, and 2.4. As the slab thickness increases, the BICs move outward and eventually fall below the light line into the area shaded in dark blue.

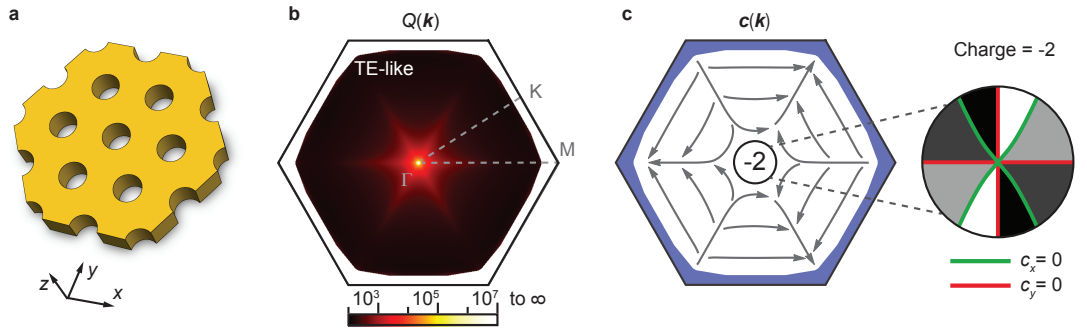

Figure 4.7: Stable BIC with topological charge -2. **a**, Schematic drawing of the photonic crystal slab. **b**, Q plotted in the first Brillouin zone, showing a BIC at the Γ point. **c**, Polarization vector field characterizes the BIC with a stable topological charge of -2, as can be shown from double degeneracies of both nodal lines.

Charge -2 can also be understood from the double degeneracy of both nodal lines of c_x (green) and c_y (red), shown in the inset of Figure 4.7c. All four nodal lines are pinned at Γ point stabilized by the C_6 symmetry.

4.10 BICs related by point group symmetries

The symmetries of the system also restrict the possible values of topological charges, since the nodal curves must respect the point symmetry. BICs at $\mathbf{k}$ points related by in-plane point-group symmetries of the system (mirror reflections and rotations) have the same topological charges.

Here, we prove that when the structure has a certain in-plane point group symmetry $\mathcal{R}$ (namely, $\epsilon(\mathbf{r}) = \epsilon(\mathcal{R}\mathbf{r})$; $\mathcal{R}$ can be a combination of rotation and reflection on the x-y plane) and when the band has no degeneracy, a BIC at $\mathbf{k}$ indicates there is another BIC at $\mathcal{R}\mathbf{k}$ with the same topological charge. The assumption here is that the eigenfunctions $\mathbf{u_k}$ at different k points already have their phases chosen to ensure the reality of $\mathbf{c}(\mathbf{k})$, and the signs of $\mathbf{u_k}$ at different k points have been chosen such that $\mathbf{u_k}$ is continuous

with respect to $\mathbf{k}$ (so that a small change in $\mathbf{k}$ leads to a small change in $\mathbf{u_k}$).

We start by relating the eigenfunction at $\mathbf{k}$ and the eigenfunction at $\mathcal{R}\mathbf{k}$. Let $\mathbf{u_k}$ be an eigenfunction of operator $\Theta_\mathbf{k}$. Since the system is invariant under transformation $\mathcal{R}$, we know $\hat{O}_\mathcal{R}\mathbf{u_k}$ is an eigenfunction of $\Theta_{\mathcal{R}\mathbf{k}}$, so in the absence of degeneracy, we can write $\hat{O}_\mathcal{R}\mathbf{u_k} = \alpha_\mathbf{k}\mathbf{u}_{\mathcal{R}\mathbf{k}}$, where $\alpha_\mathbf{k}$ is some number. The number $\alpha_\mathbf{k}$ must have unit magnitude (due to the normalization of $\mathbf{u_k}$ and $\mathbf{u}_{\mathcal{R}\mathbf{k}}$) and must be real-valued (because $\mathbf{c}(\mathbf{k})$ is real-valued), so it can only take on discrete values of ± 1. Also, $\alpha_\mathbf{k}$ must be a continuous function of $\mathbf{k}$ since $\mathbf{u_k}$ is continuous with respect to $\mathbf{k}$. Since $\alpha_\mathbf{k}$ is both discrete-valued and continuous, it must be a constant. Then, we may denote this constant with its value at the Γ point, as $\alpha_\mathbf{k} = \alpha_\Gamma$. Note that $\mathcal{R}\mathbf{\Gamma} = \mathbf{\Gamma}$, so we can determine coefficient $\alpha_\mathbf{\Gamma}$ using the mode profile: $\hat{O}_\mathcal{R}\mathbf{u_\Gamma} = \alpha_\mathbf{\Gamma}\mathbf{u_\Gamma}$. In conclusion, we have $\mathbf{u}_{\mathcal{R}\mathbf{k}} = \alpha_\Gamma \hat{O}_\mathcal{R}\mathbf{u_k}$.

Now we consider how the angle $\phi(\mathcal{R}\mathbf{k})$ is related to $\phi(\mathbf{k})$. The vector field $\mathbf{u_k}$ transforms under the rotation operator as $(\hat{O}_\mathcal{R}\mathbf{u_k})(\mathbf{r}) = \mathcal{R}\mathbf{u_k}(\mathcal{R}^{-1}\mathbf{r})$, so averaging over x and y we get $\langle \hat{O}_\mathcal{R}\mathbf{u_k}\rangle = \mathcal{R}\langle\mathbf{u_k}\rangle$. Let P be the operator that projects a 3D vector onto the x-y plane, namely $P\mathbf{r} = \mathbf{r} - (\mathbf{r}\cdot\hat{z})\hat{z}$; it commutes with $\mathcal{R}$, since it does not alter the x or y component. Then $\mathbf{c}(\mathbf{k}) = P\langle\mathbf{u_k}\rangle$, and

$$\mathbf{c}(\mathcal{R}\mathbf{k}) = P\langle\mathbf{u}_{\mathcal{R}\mathbf{k}}\rangle = P\langle\alpha_\Gamma\hat{O}_\mathcal{R}\mathbf{u_k}\rangle = \alpha_\Gamma\mathcal{R}P\langle\mathbf{u_k}\rangle = \alpha_\Gamma\mathcal{R}\mathbf{c}(\mathbf{k}). \tag{4.5}$$

So, the polarization vector at the the transformed k point is simply the original polarization vector transformed and times ± 1. So, the angle of the polarization vector only changes by a constant in the case of proper rotations (where $\det\mathcal{R} = 1$); in the case of improper rotations (where $\det\mathcal{R} = -1$), it also changes sign. So, in general, we can write

$$\phi(\mathcal{R}\mathbf{k}) = (\det\mathcal{R})\phi(\mathbf{k}) + c \tag{4.6}$$

with c being a constant depending on $\mathcal{R}$ and α_Γ. It follows that $\nabla_{\mathcal{R}\mathbf{k}}\phi(\mathcal{R}\mathbf{k}) = (\det\mathcal{R})\mathcal{R}\nabla_{\mathbf{k}}\phi(\mathbf{k})$, so the topological charge at $\mathcal{R}\mathbf{k}$ is

$$\begin{aligned} q_{\mathcal{R}\mathbf{k}} &= \frac{1}{2\pi}\oint_{C_{\mathcal{R}\mathbf{k}}} \nabla_{\mathbf{k}''}\phi(\mathbf{k}'')\cdot d\mathbf{k}'' \\ &= \frac{1}{2\pi}\oint_{\mathcal{R}^{-1}C_{\mathcal{R}\mathbf{k}}} \nabla_{\mathcal{R}\mathbf{k}'}\phi(\mathcal{R}\mathbf{k}')\cdot \mathcal{R}d\mathbf{k}' \\ &= \frac{1}{2\pi}(\det\mathcal{R})\oint_{C_{\mathbf{k}}} \nabla_{\mathcal{R}\mathbf{k}'}\phi(\mathcal{R}\mathbf{k}')\cdot \mathcal{R}d\mathbf{k}' \\ &= \frac{1}{2\pi}(\det\mathcal{R})^2\oint_{C_{\mathbf{k}}} \cancel{\mathcal{R}}\nabla_{\mathbf{k}'}\phi(\mathbf{k}')\cdot \cancel{\mathcal{R}}d\mathbf{k}' \\ &= q_{\mathbf{k}}, \end{aligned} \tag{4.7}$$

where $C_{\mathcal{R}\mathbf{k}}$ is a closed simple path that is centered on $\mathcal{R}\mathbf{k}$ and loops in counterclockwise direction, $\mathcal{R}^{-1}C_{\mathcal{R}\mathbf{k}}$ is this loop transformed by $\mathcal{R}^{-1}$ (which centers on $\mathbf{k}$ in counterclockwise direction if $\mathcal{R}$ is a proper rotation, or in clockwise direction if $\mathcal{R}$ is improper), and $C_{\mathbf{k}}$ is this transformed loop traversed in counterclockwise direction.

In conclusion, we have proven that if a system has certain point group symmetry $\mathcal{R}$, then the topological charges carried by the BIC at $\mathbf{k}$ and at $\mathcal{R}\mathbf{k}$ on a singly degenerate band have to be the same. This conclusion agrees with all examples in Figures 4.3, 4.5 and 4.6.

4.11 Allowed Charges at High-symmetry Points

Using the fact that BICs at $\mathbf{k}$ points related by in-plane point-group symmetries of the system (mirror reflections and rotations) have the same topological charges, one can calculate all possible topological charges of BICs at high symmetry $\mathbf{k}$ points. For a system with C_n symmetry, the possible topological charges at the Γ point on a singly-

Table 4.1: Allowed stable topological charges at Γ for singly degenerate bands. $A(B)$ corresponds to modes of different representations of the symmetry operator [182]. Note that only singly degenerate representations of symmetry operators are included in here.

Symmetries	Representation	Charges	Allowed n	Allowed charges
C_2	A	$\pm 1 + 2n$	0	± 1
	B	$0 + 2n$		0
C_3	A	$1 + 3n$	$0, \pm 1, ...$	+1,+4,-2,...
C_4	A	$1 + 4n$	$0, \pm 1, ...$	+1,+5,-3,...
	B	$-1 + 4n$		-1,-5,+3,...
C_6	A	$1 + 6n$	$0, \pm 1, ...$	+1,+7,-5,...
	B	$-2 + 6n$		-2,+4,-8,...

degenerate band are given in Table 4.1. This is consistent with all examples in this paper. This table can be used to predict the charges in other systems of interest and to design high order vector beams.

Allowed topological charges at high symmetry k points can be determined by the field eigenvalues of the rotational symmetry of a system. For systems with m-fold rotational symmetry, we can first determine the relationship between polarization direction at wavevector $\mathbf{k}$ and at rotated wavevector $\mathcal{R}\mathbf{k}$ ($\phi(\mathbf{k})$ and $\phi(\mathcal{R}\mathbf{k})$) using Eq. (4.5). Since the wavevector gets back to its original point if applying this rotation m-times: $\mathcal{R}^m\mathbf{k} = \mathbf{k}$, we can then apply this relationship m times and get how many times the polarization vector rotates around the center of the Brillouin zone. From there, we categoraize all possible charges allowed at $\mathbf{\Gamma}$ as shown in Table 4.1. Allowed charges depend on two factors. The first one is which symmetry representation the band belongs to. The second

one is the degeneracy of nodal lines at Γ, because more nodal lines intersecting at the same point usually leads to more oscillations in color and thus higher topological charges. This factor is reflected by the integer number n, depending on the number of equivalent $\mathbf{\Gamma}$ points at this frequency [78]. Note that only singly degenerate bands are considered in this Letter, having no crossing with other bands in the bandstructures, as can be seen in Table 4.1. Further research directions may include BICs on degenerate bands, as well as the search of BICs with higher-order and potentially fractional topological charges.

4.12 Conclusions

In conclusion, we have demonstrated that BICs in photonic crystal slabs are associated with vortices in the polarization field and explained their robustness in terms of conserved topological charges. We derive the symmetries that constrain these charges and explain their generation, evolution and annihilation. We conjecture that most robust BICs [39, 162, 108, 163, 124, 115, 71, 72] will correspond to topological defects in appropriate parameter spaces. Our finding connects electromagnetic BICs to a wide range of physical phenomena including Berry phases around Dirac points [122], topological defects [129], and general vortex physics [34]. Optical BICs in photonic crystals have a wealth of applications. Lasing action can naturally occur at BIC states where the quality factor diverges. The angular (wavevector) tunablity of the BICs makes them great candidates for on-chip beam-steering [104]. Furthermore, photonic crystal lasers through BICs are naturally vector beams [78, 98], which are important for particle accelerations, optical trapping and stimulated emission depletion microscopy.

Chapter 5

Transparent displays enabled by resonant nanoparticle scattering*

5.1 Introduction

Transparent display is a rapidly growing technology that enables many useful applications. With transparent displays, navigating information can be displayed on car windshields and aircraft cockpit windows; regular glass windows and even eyeglasses can become monitor screens for work or entertainment. A number of different transparent displays have been developed, each suitable for a subset of the applications. The simplest type is the head-up display, which projects into the viewer's eyes through reflecting the image off a beam splitter [145]. Head-up displays are well suited to certain occasions, but the narrow viewing angle limits the position of the viewer. Diffusive screens achieve wider viewing angles by light scattering [55]; such screens do not have wavelength selectivity, so stronger scattering is necessarily accompanied by lower transparency. Frequency-conversion screens achieve higher transparency using molecules that convert the projected ultraviolet light to visible light [204, 112, 203], or infrared light

*This chapter is based on: C. W. Hsu, B. Zhen, W. Qiu, O. Shapira, B. G. DeLacy, J. D. Joannopoulos, and M. Soljačić, "Transparent displays enabled by resonant nanoparticle scattering," *Nature Communications* **5**, 3152 (2014).

to visible light [35]; the conversion, however, is challenging to implement with high efficiency. Instead of relying on projection, one can also make electronic flat-panel displays transparent, for example by combining organic light-emitting diodes with transparent electronics [56, 87, 157]. There is active research in developing this type of transparent displays, but scaling to large display sizes remains challenging. Given the limitations of these existing methods, it remains of great interest to explore new types of transparent displays.

Here we create a transparent display by projecting monochromatic images onto a transparent medium embedded with nanoparticles that selectively scatter light at the projected wavelength. With the wavelength-selective scattering, such a screen can efficiently display the projected image while being highly transparent to the ambient light. After optimizing the design of such nanoparticles, we experimentally demonstrate this concept with a blue-color, broad viewing angle, transparent display made of silver nanoparticles in a polymer matrix. This method is simple, low cost, and scalable to large sizes; these features make it attractive for some of the various transparent display applications.

5.2 Concept: Wavelength-selective Scattering

Our approach is based on the fact that nanoparticles with sharp resonances can selectively scatter light of a particular wavelength, while being almost transparent at other wavelengths. By embedding wavelength-selective nanoparticles in a transparent medium and by projecting images at the resonant wavelength λ_0, we can create a screen that scatters most of the projected light while being almost transparent to the broad-band ambient light. This is illustrated in Figure 5.1. To implement a full-color display, one

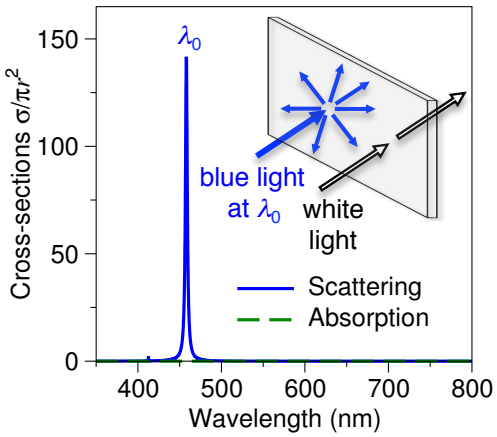

Figure 5.1: Working principle for a transparent display based on wavelength-selective scattering from nanoparticles. The desired nanoparticles have the scattering cross-section sharply peaked at wavelength λ_0, and the absorption cross-section uniformly zero. A transparent medium embedded with such nanoparticles is transparent except for light at wavelength λ_0, as sketched in the inset. As an example, here we show the cross-sections for a metallic sphere in air, where the sphere has radius $r = 15$ nm, and the metal is described by the Drude model with plasma wavelength 260 nm and negligible dissipation; the absorption cross-section is negligible in this case.

could use three types of nanoparticles, each selectively scattering light at one of the three desired colors: red, green, and blue; alternatively, one could use a designed nanoparticle with multiple resonances, each lying at one of the three desired wavelengths. The challenge of a good implementation lies in making the resonances sharp while maintaining high transparency away from the resonances.

5.3 Material Choice

One way to achieve wavelength selectivity is using the localized surface plasmon resonances in metallic nanoparticles [93, 76, 106, 9, 40]. We first provide a rough estimate

to determine which metal is optimal to use. For a particle much smaller than the wavelength λ of the incident light, the local electromagnetic field has almost no spatial variation. We can calculate the optical response from such a particle using the quasi-static approximation (also called dipole approximation) [15]. Here we apply this method to estimate the sharpness of the scattering cross-section for small plasmonic particles of arbitrary shapes. In the quasi-static approximation, the scattering cross-section σ_{sca} averaged over angle and polarization of the incoming light is [15]

$$\langle \sigma_{\text{sca}} \rangle = \frac{k^4}{6\pi} \frac{1}{3} \sum_{j=1,2,3} |\alpha_j(\epsilon)|^2 , \tag{5.1}$$

where $k = 2\pi\sqrt{\epsilon_m}/\lambda$ is the wavenumber in the surrounding medium, and $\alpha_{1,2,3}$ are the static electric polarizabilities of the particle in three orthogonal polarizations. Localized surface plasmon resonances occur at the wavelength λ_0 for which

$$\frac{1}{\alpha_j(\text{Re}(\epsilon(\lambda_0)))} = 0. \tag{5.2}$$

For a sphere, this condition simplifies to $\text{Re}(\epsilon(\lambda_0)) = -2\epsilon_m$; here we work with the more general expression that is applicable to arbitrary shapes. We denote the real and imaginary parts of the on-resonance (at λ_0) and off-resonance (at $\lambda_0 + \Delta\lambda$, for a small $\Delta\lambda$ of interest) dielectric constants as

$$\epsilon(\lambda_0) = \epsilon_r + i\epsilon_i, \qquad \epsilon(\lambda_0 + \Delta\lambda) = (\epsilon_r + \Delta\epsilon_r) + i(\epsilon_i + \Delta\epsilon_i), \tag{5.3}$$

assuming $\Delta\epsilon_r \ll \epsilon_r$ and $\Delta\epsilon_i \ll \epsilon_i$. We write the polarizability as a rational function, $\alpha_j(\epsilon) = N(\epsilon)/D(\epsilon)$, and let the polynomial in the denominator be $D(\epsilon) = \sum_{n=0} c_n \epsilon^n$. Using the fact that $D(\epsilon_r) = 0$, we can subtract $D(\epsilon_r)$ from the off-resonance $D(\epsilon)$, and

take out the common factor to get

$$D(\epsilon(\lambda_0 + \Delta\lambda)) \approx [\Delta\epsilon_r + i\epsilon_i] \left[c_1 + c_2 (2\epsilon_r + i\epsilon_i) + c_3 \left(3\epsilon_r^2 - \epsilon_i^2 + 3i\epsilon_r\epsilon_i\right) + \cdots\right] \quad (5.4)$$

Only the first square bracket is of interest to us, since none of the terms in the second square bracket depends on $\Delta\lambda$. With this observation, we see that the ratio between on-resonance and off-resonance scattering cross-sections is approximately

$$\frac{\langle\sigma_{\text{sca}}(\lambda_0)\rangle}{\langle\sigma_{\text{sca}}(\lambda_0 + \Delta\lambda)\rangle} \approx \left|\frac{\alpha_j(\epsilon(\lambda_0))}{\alpha_j(\epsilon(\lambda_0 + \Delta\lambda))}\right|^2 \approx \left|\frac{D(\epsilon(\lambda_0 + \Delta\lambda))}{D(\epsilon(\lambda_0))}\right|^2 \approx 1 + \left|\frac{\Delta\epsilon_r}{\epsilon_i}\right|^2. \quad (5.5)$$

Note that this result is valid for particles of arbitrary shapes, as long as particle size $\ll$ wavelength. With this result, we can estimate the sharpness of the scattering cross-section using only the dielectric function $\epsilon(\lambda)$ of the metal. However, we note that the resonance condition, equation (5.2), requires materials with negative $\text{Re}(\epsilon)$, so this result can only be applied to plasmonic resonances.

Equation (5.5) reveals that, for optimal wavelength-selective scattering, the desired material should have a small $\text{Im}(\epsilon)$ and a fast-changing $\text{Re}(\epsilon)$ near the resonance wavelength λ_0. A metal with negligible loss would be ideal (Figure 5.1 provides one example; also see Ref. [212]), but most metals are quite lossy in the visible spectrum. Figure 5.2a shows the metals with large $\eta \equiv |\text{Re}(d\epsilon/d\lambda)/\text{Im}(\epsilon)|^2$ in the visible spectrum (refractive index from Ref. [155]). Silver has the highest value of η for most of the visible spectrum, so we choose to work with silver-based nanoparticles.

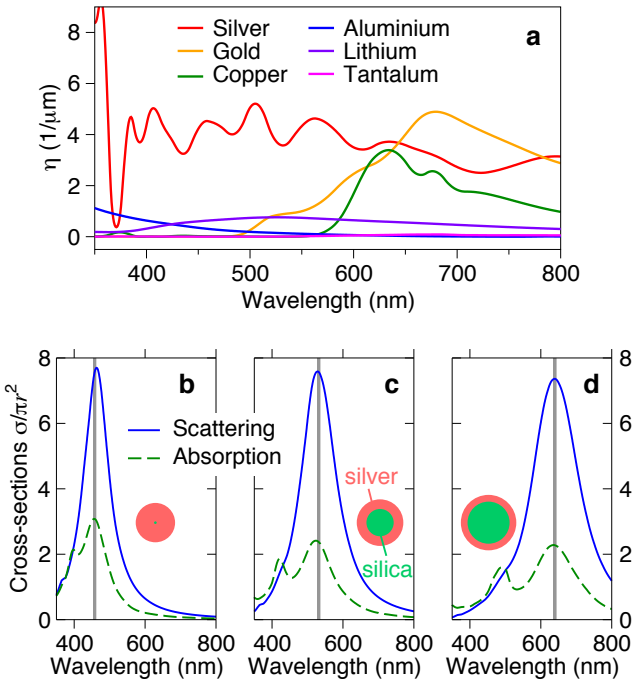

Figure 5.2: Theory design for metallic nanoparticles suitable for displaying three different colors. (**a**) A performance estimator for the wavelength selectivity of small plasmonic particles. See text for the definition of η. (**b-d**) Scattering and absorption cross-sections for silica-core silver-shell nanoparticles (embedded in an $n = 1.44$ medium) optimized to scatter monochromatic light at $\lambda_0 = 458$ nm (blue, **b**), 532 nm (green, **c**), and 640 nm (red, **d**). Insets show the relative sizes of the structures; r is the outer radius of the particle.

5.4 Optimization

For more detailed optimization, we define a figure of merit (FOM)

$$\mathrm{FOM} = \frac{\sigma_{\mathrm{sca}}(\lambda_0)}{2\overline{\sigma_{\mathrm{sca}}} + \max\{\sigma_{\mathrm{abs}}\}} \tag{5.6}$$

that captures the desired properties: a uniformly low absorption cross-section σ_{abs}, a high scattering cross-section σ_{sca} at λ_0, and low σ_{sca} elsewhere. The overline and the symbol $\max\{\dots\}$ denote the mean and the maximum in the visible spectrum (from 390 nm to 750 nm). The number 2 is a weighing factor chosen to balance sharp scattering and low absorption. The absolute value of the cross-section per particle is less important here because one can adjust the areal density of the nanoparticles on the screen; thus, the FOM is defined as a ratio. Also, in order to have a colorless transparent screen, we prefer a flat absorption spectrum, so we use $\max\{\sigma_{\mathrm{abs}}\}$ rather than $\overline{\sigma_{\mathrm{abs}}}$. One can also consider imposing a wavelength-dependent weight on the cross-sections to account for the spectral sensitivity of human eyes [187], but we omit this weight for simplicity. With this FOM, we perform numerical optimizations on spherical core-shell nanoparticles with a silver shell and silica core, embedded in a transparent medium with refractive index $n = 1.44$. Scattering and absorption cross-sections are calculated with the transfer matrix method [168], using $n = 1.45$ for silica and experimental values of the dielectric function for silver [155]. Particle size distribution is assumed to be a Gaussian with the standard deviation being 10% of the mean. We choose the core radius and shell thickness that maximize the FOM by performing a global optimization via the multi-level single-linkage algorithm [103] implemented within the free nonlinear optimization package NLopt [83]. The resonance wavelength λ_0 can be tuned to arbitrary colors.

Table 5.1: Optimal particle sizes and FOM for silica-core silver-shell nanoparticles.

Wavelength λ_0	Core radius	Shell thickness	FOM
458 nm	1.3 nm	30.8 nm	1.01
532 nm	22.2 nm	15.8 nm	0.91
640 nm	34.3 nm	11.0 nm	0.81

Figure 5.2b-d show the cross-sections of structures optimized to scatter monochromatic light at $\lambda_0 = 458$ nm (blue), 532 nm (green), and 640 nm (red); the corresponding particle sizes and FOMs are listed in Table 5.1.

According to the example in Figure 5.1, one would prefer σ_{sca} to be even more narrow in wavelength; nevertheless, as we will see, one can obtain fairly good transparent display properties even with cross-sections comparable to those shown in Figure 5.2. Therefore, we leave it to future work to further improve the design. Dielectric nanoparticles may be a promising direction, as their resonance line-widths are not as limited by absorption loss compared to metals [235]; Figure 5.3 provides such examples. Utilizing higher-order resonances [212, 60, 179, 180] is also a possible direction, provided that one can keep the lower-order broadband resonances out of the visible spectrum. The same FOM and optimization procedure can be applied in these explorations.

5.5 Fabrication and Characterization

As a proof of principle, we experimentally realize a blue-color-only transparent display. Simple spherical silver nanoparticles are used, since the structure optimized to scatter blue light has a negligible silica core (Table 5.1). A transmission electron microscopy

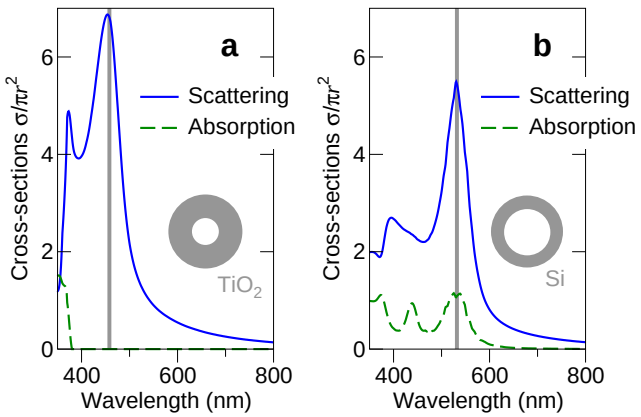

Figure 5.3: Resonant scattering of dielectric nanoshells. **(a)** Calculated cross-sections of a titanium dioxide nanoshell (inner radius 25.5 nm; outer radius 70.1 nm) optimized to scatter blue light at $\lambda_0 = 458$ nm (FOM = 1.76). **(b)** Calculated cross-sections of a silicon nanoshell (inner radius 43.8 nm; outer radius 68.2 nm) optimized to scatter green light at $\lambda_0 = 532$ nm (FOM = 1.14). Both the core and the surrounding medium are assumed to have refractive index $n = 1$; in practice they may be low-index materials such as a transparent aerogel. Calculations take into account a $\pm 10\%$ random distribution in the shell thickness. Insets show the relative sizes of the nanoshells. The resonances in dielectric nanoparticles have the advantage of low absorption loss, but the index contrast must be high to provide sufficient confinement.

(TEM) image of these particles (nanoComposix) is shown in the inset of Figure 5.4a; their diameter of 62 nm ± 4 nm is chosen to match the optimized structure. To host the nanoparticles in a transparent polymer matrix, we mix 10% weight of polyvinyl alcohol (PVA, 80% hydrolyzed, Sigma Aldrich) into an aqueous solution of silver nanoparticles (concentration 0.01 mg/mL). We pour 480 mL of this liquid onto a framed square glass plate that is 25 cm in width, remove air bubbles from the liquid with a vacuum chamber, and let the liquid dry out in the hood at room temperature. Over a course of 40 hours, the liquid solidifies into a transparent polymer film of thickness 0.46 mm. This transparent thin film is the screen of our display. Its average transmittance is 60% in the visible spectrum (averaged from 390 nm to 750 nm).

Figure 5.4a shows the transmittance spectrum of this film. For a direct comparison with theory, the measured data is normalized by the transmittance of a plain PVA film of the same thickness (which is higher than 90% in the visible spectrum). Theory prediction (solid line in Figure 5.4a) from the calculated cross-sections and the Beer-Lambert law (no fitting variables) agrees well with the measured data; the slight discrepancy is due to a minor clustering of the nanoparticles (Figure 5.5). The calculated cross-sections indicate that the on-resonance scattering is significantly stronger than the on-resonance absorption (Figure 5.4b), which is good for our purpose here. Figure 5.4c shows the angular distribution of scattered light at λ_0. The distribution is close to the Lambertian distribution for an ideal diffusely reflecting surface, confirming that the scattered light can be viewed from a wide angle. The polarization dependence is weak, indicating that we may operate the screen with incident light of arbitrary polarization.

A minimal model for the angular dependence yields the lines in Figure 5.4c. The overall trend of the angular distribution can be described by a factor $f_1 = \cos\theta$ that accounts for the observed area at angle θ; this is the Lambertian distribution. To

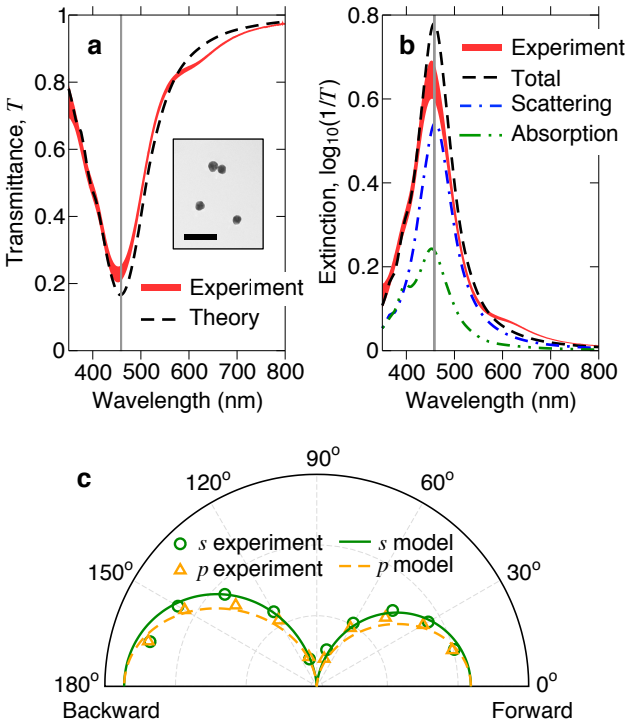

Figure 5.4: Characterization of the fabricated film that is used as a transparent screen. (**a**) Transmittance spectrum of the film; width of the experimental curve indicates plus/minus one standard deviation across different spots on the film. Inset shows a TEM image of the nanoparticles; the diameter is 62 nm ± 4 nm. Scale bar, 200 nm. (**b**) Same data plotted as extinction, together with theory-predicted contributions from scattering and absorption. (**c**) Angular distribution of scattered light at 458 nm, when normally incident light has electric field polarized perpendicular (s) and parallel (p) to the scattering plane. The radial axis is in arbitrary units.

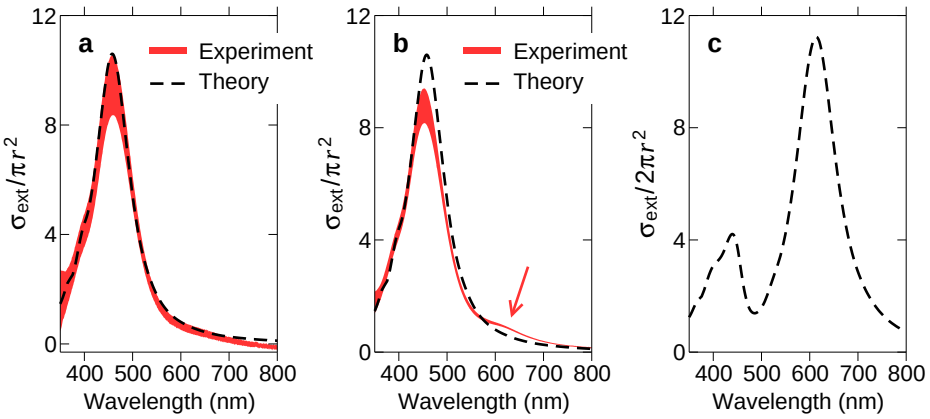

Figure 5.5: Effects of nanoparticle clustering. (a, b) Experimental and theoretical extinction cross-section ($\sigma_{\text{ext}} = \sigma_{\text{sca}} + \sigma_{abs}$) spectrum for a spherical silver nanoparticle in PVA. Width of the experimental curve indicates plus/minus one standard deviation. The initial nanoparticle concentration is 5 μg/mL in **a**, and 10 μg/mL in **b**. Measured extinction data in **b** show an excess of σ_{ext} near 620 nm, indicated by an arrow. **(c)** Theoretical extinction cross-section spectrum of two silver nanoparticles that stick together, calculated for polarization along the axis of alignment. These results indicate that the excess of σ_{ext} near 620 nm is present only at higher concentration of nanoparticles, and it can be explained by the presence of nanoparticles that stick together (one such example is shown in the TEM image, in Figure 3a of the main text).

account for the polarization dependence, we consider a single-scattering event from a small particle, which has a factor $f_2^{\perp} = 1$ and $f_2^{\parallel} = \cos^2\theta'$ for electric field polarized perpendicular or parallel to the scattering plane [15]; here θ' is the angle inside the PVA film, given by $\sin\theta = n\sin\theta'$, where $n = 1.44$ is the refractive index of PVA. We also account for the transmission coefficient f_3 from PVA to air, given by Fresnel equations. Lastly, light scattered to the back side is attenuated by absorption, which we estimate to be around 20%, so we include an additional factor of $f_4 = 0.8$ for $\theta < 90$ deg., $f_4 = 1$ for $\theta > 90$ deg. Combining these factors, we model the angular dependence as $f_1 f_2 f_3 f_4$. Prediction of this minimal model is plotted in Figure 5.4c.

5.6 Display Demonstration

In Figure 5.6a, we show the transparent display at work, with a blue MIT logo projected onto the screen from a small laser projector (MicroVision SHOWWX+). This projector is suitable here since it functions by projecting monochromatic light from three laser diodes (red, green, and blue) [48]; we measure the wavelength of its blue light to be 458 nm ± 2 nm. The projected image shows up clearly on our screen, and is visible from all directions. In comparison, the same image projected onto regular glass (Figure 5.6a, photo on the right) can barely be seen due to the lack of scattering. The transparency of our screen can be judged by comparing it with regular glass: Figure 5.6a shows that objects behind the screen (three colored cups) remain visible, and their apparent color and brightness change only very slightly. We also compare an image projected onto this screen and onto a piece of white paper: Figure 5.6b shows that on our screen, the projected image is slightly dimmer but the contrast is better due to less scattering of ambient light. Finally, we point out that high-resolution images can be projected onto

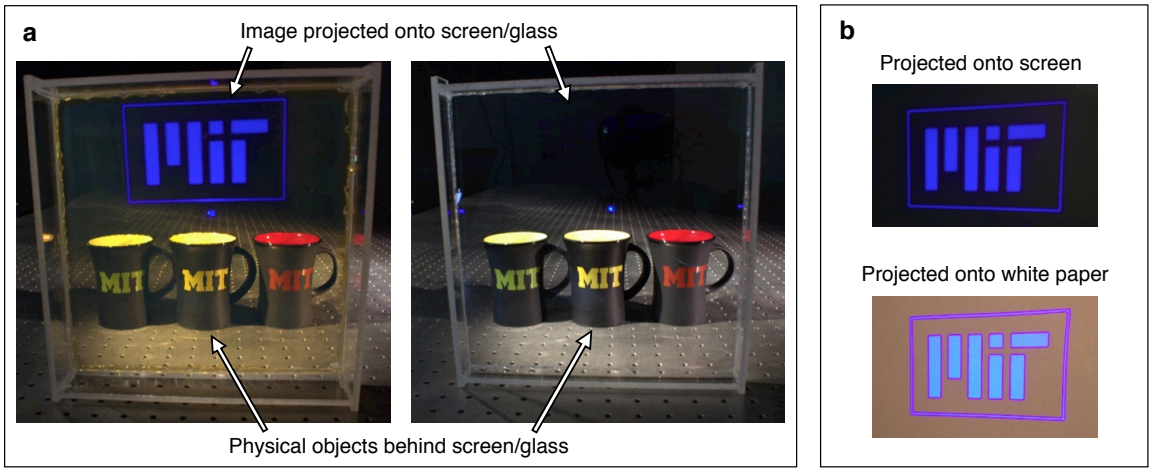

Figure 5.6: Demonstration of a blue-color transparent display. (**a**) Photographs showing the transparent screen (left) in comparison with a regular piece of glass (right). A laser projector projects a blue MIT logo onto both the transparent screen and the regular glass; the logo shows up clearly on the transparent screen, but not on the regular glass. Three cups are placed behind to visually assess the transparency. (**b**) Photographs comparing letters projected onto the transparent screen (top) and onto a piece of white paper (bottom). In both **a** and **b**, the pair of photographs are captured with the same lighting condition and exposure, and photographs are not edited. See also Supplementary Movie 1.

this screen with clarity, because the screen has on average 6×10^9 nanoparticles per cm^2 of area.

5.7 Conclusions

We have proposed and demonstrated transparent displays enabled by the wavelength-selective scattering of nanoparticles. Decent transparency and scattering efficiency has been achieved with our proof-of-concept demonstration, and this method has additional attractive features including simplicity, wide viewing angle, and scalability to large sizes. The method is also economical: in our experiment, the polymer is inexpensive, and only 7 μg of silver nanoparticles is used per cm^2 of screen. The natural next step of

this method will be achieving narrower line-width for the scattering while maintaining transparency away from the resonance; this will further enhance transparency, and will be important for the realization of a full-color transparent display.

Finally, we point out a few extensions of this transparent display method. First, with a flexible polymer matrix, we can potentially realize flexible and scrollable transparent displays. Second, since most light undergoes single scattering (the thickness of the film, 0.46 mm, is comparable to the mean free path at resonance, 0.26 mm) instead of multiple scattering, the scattered light retains the polarization of the incident light. Therefore, one can achieve three-dimensional viewing effect by projecting two images simultaneously (one right-handed circularly polarized and one left-handed circularly polarized) and viewing the superimposed image with polarized glasses. Third, by placing a black cloth behind such a transparent screen, one can also create a black screen (non-transparent) that has higher contrast than a traditional white screen: as shown in Figure 5.6b, a traditional white screen may have low contrast due to the diffuse scattering of ambient light, but the transparent screen does not.

Chapter 6

Theoretical criteria for scattering dark states in nanostructured particles*

6.1 Introduction

When macroscopic structures are shrunk to the nanoscale, their optical properties depart dramatically from the intuitive ray-optics picture [15]. Subwavelength structures on resonance can have scattering cross sections much larger than their geometrical sizes [60, 180], and the presence of multiple resonances leads to even more possibilities through mode hybridization [166] and interference effects [134, 118, 170, 94, 59]. A particularly interesting phenomenon is the suppressed scattering in nanostructures with multiple plasmonic resonances [218, 199, 7, 54, 51, 50, 169, 140, 8, 107, 117, 1, 30, 46], plasmonic and excitonic resonances [100, 232, 45, 237, 123, 186, 242], or dielectric resonances [23, 96], referred to collectively as a "scattering dark state." A wealth of models

*This chapter is based on: C. W. Hsu, B. G. DeLacy, S. G. Johnson, J. D. Joannopoulos, and M. Soljačić, "Theoretical criteria for scattering dark states in nanostructured particles," *Nano Letters* **14**, 2783 (2014).

has been employed to describe this suppressed scattering, ranging from perturbative models [7], generalization of the Fano formula [54, 51, 50], and electrostatic approximation, [30, 46] to coupled-mechanical-oscillator models [140, 8, 107, 1, 117]. These models reveal valuable insights and facilitate the design of specific structures with desired line shapes. However, the general criteria for observing such scattering dark states remain unclear. Non-scattering states have been known in atomic physics since the early works of Fano [43] and have been discovered in a variety of nanoscale systems in recent years [178, 181, 118, 134, 170, 94]. However, Fano resonances generally concern the interference between a narrow discrete resonance and a broad resonance or continuum. Meanwhile, many occurrences of the scattering dark state involve the interference between multiple narrow discrete resonances, and it seems necessary to treat the multiple resonances at equal footing. Thus, we seek a formalism analogous to the phenomenon of coupled-resonator-induced transparency [134] that has been established in certain other systems such as coupled mechanical oscillators [53, 81], coupled cavities [150, 202], coupled microring resonators [198, 121, 144, 238, 211], and planar metamaterials [44, 156, 245, 113].

Here, we derive the general equations governing the resonant light scattering from a spherical or a non-spherical but subwavelength obstacle, accounting for multiple resonances with low loss. Due to the spherical symmetry (or the small size) of the obstacle, different channels of the multipole fields are decoupled. We find that within each channel, n resonances always lead to $n-1$ scattering dark states in the low-absorption limit. This universal result is independent of the radiative decay rates of the resonances, method of coupling (can be near-field or far-field), nature of the resonances (can be plasmon, exciton, whispering-gallery, *etc.*), number of resonances, which of the multipole, TE or TM polarization, and other system details. With different choices of

basis, one can interpret the scattering dark state as arising from the far-field coupling of multiple radiating resonances, or arising from the near-field coupling of a radiating and several non-radiating resonances. We provide explicit examples using plasmonic resonances and whispering-gallery resonances, showing zero scattering for lossless materials and significantly suppressed scattering for realistic materials with loss. We also discuss potential applications for slow light, transparent projection screen, and wavelength-selective transmission.

6.2 Multipole Expansion

Consider a linearly polarized planewave incident on an obstacle that is spherical or non-spherical but much smaller than the wavelength of the incident light. This obstacle can have arbitrary number of layers and material composition; in the small-obstacle case, it can also be a cluster of particles. We start with the general formalism for such a scattering problem. Outside the obstacle, the electric field can be written as $\mathbf{E} = \nabla \times (\mathbf{r}\psi_{\mathrm{TE}}) - (i/k)\nabla \times \nabla \times (\mathbf{r}\psi_{\mathrm{TM}})$, where $\mathbf{r}$ is position from the particle center, k is the wave number, and ψ_σ is a scalar function satisfying the Helmholtz equation [15]. We use σ to denote the two polarizations: transverse-electric (TE) or transverse-magnetic (TM), where the electric or magnetic field is perpendicular to $\mathbf{r}$. Choose our coordinate such that the z axis and the x axis is aligned with the polarization and the propagation direction of the incident light respectively. The incident planewave consists of all multipole terms with $l > 0$ and $m = 1$ in both TE and TM [15], so the general solution can be written as

$$\psi_\sigma(r, \theta, \phi) = f_\sigma(\phi) \sum_{l=1}^{\infty} \left[s^-_{l,\sigma} h^{(1)}_l(kr) + s^+_{l,\sigma} h^{(2)}_l(kr) \right] P^1_l(\cos\theta), \tag{6.1}$$

where $f_{\mathrm{TE}}(\phi) = \sin\phi$, $f_{\mathrm{TM}}(\phi) = \cos\phi$, $h_l^{(1)}$ (or $h_l^{(2)}$) is the spherical Henkel function of the first (or second) kind corresponding to outgoing (or incoming) spherical wave, and P_l^1 is the associated Legendre polynomial with $m = 1$. The amplitudes of outgoing and incoming waves $s_{l,\sigma}^{\mp}$ are coefficients of the general solution. Here, each angular momentum and polarization pair (l, σ) corresponds to a distinct "channel." The spherical symmetry (or the small size) of the obstacle means that different channels are decoupled, so optical response properties are given by the reflection coefficients $R_{l,\sigma} \equiv s_{l,\sigma}^{-}/s_{l,\sigma}^{+}$. Energy conservation requires that $|R_{l,\sigma}| \leq 1$ in each channel. The total scattering cross section of this particle is given by

$$\sigma_{\mathrm{sca}} = \frac{\lambda_{\mathrm{m}}^2}{8\pi} \sum_{\sigma} \sum_{l=1}^{\infty} (2l+1) \left|1 - R_{l,\sigma}\right|^2 , \tag{6.2}$$

where λ_{m} is the wavelength in the surrounding medium. Note that there is no inter-channel interference here, unlike the intensity of the scattered light at a specific angle (such as back scattering) where different channels of spherical waves can interfere [213, 118].

In each channel, the scattering from a single low-loss resonance is given by a Lorentzian function [60, 180, 178, 181]. Therefore, when we consider multiple resonances each in a different channel, the total response will be a sum of Lorentzians with no scattering dark state; this is illustrated schematically in Figure 6.1a. For a scattering dark state, we need multiple overlapping resonances in the same channel, as illustrated in Figures 6.1b and c.

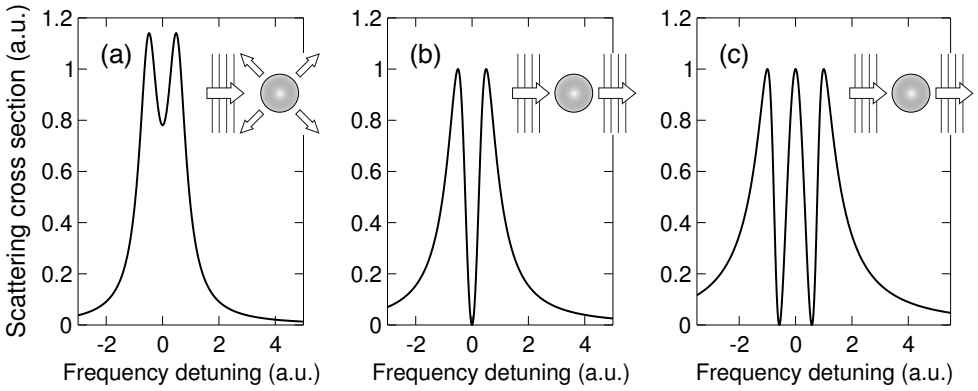

Figure 6.1: Schematic plots for light scattering when multiple resonances are excited simultaneously. (a) Two resonances in different radiation channels (*e.g.*, TM_1 and TE_1). In this case, radiation from the two resonances add up incoherently, and the cross section is a sum of two Lorentzian functions. The particle is opaque in between the two resonances (illustrated in the inset). (b) Two resonances in the same radiation channel. In this case, radiation from the two resonances add up coherently, giving rise to a different line shape and a scattering dark state where the particle becomes transparent (illustrated in the inset). (c) Three resonances in the same radiation channel. Here, two scattering dark states arise (illustrated in the inset).

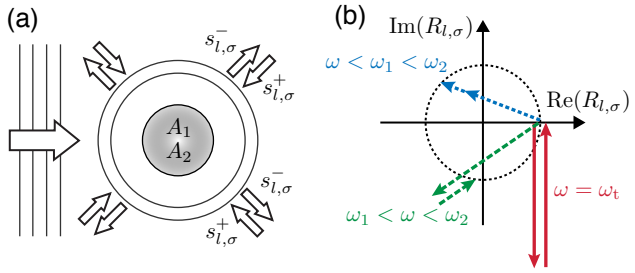

Figure 6.2: Illustration of a scattering dark state in a doubly resonant nanostructure. (a) Abstract diagram showing a nanostructure where two resonances, A_1 and A_2, in the same angular momentum l and polarization σ channel are simultaneously excited by incoming wave $s^+_{l,\sigma}$, and both radiate into outgoing wave $s^-_{l,\sigma}$. (b) Schematic illustrations showing the complex reflection coefficient $R_{l,\sigma} = s^-_{l,\sigma}/s^+_{l,\sigma}$ with contributions from the two resonances (each indicated by an arrow). When absorption loss is negligible, $R_{l,\sigma}$ always lands on the unit circle, and the two outgoing waves add up either in phase or out of phase. Different excitation frequencies are shown by arrows of different colors; at frequency ω_t, the two outgoing waves cancel, giving rise to a scattering dark state where the particle becomes transparent.

6.3 Temporal Coupled-mode Theory

We start with the simplest case of two resonances in channel (l, σ), as illustrated in Figure 6.2a. The two resonances may be of any nature (*e.g.*, plasmon, exciton, whispering-gallery). When the resonances have low loss, $R_{l,\sigma}$ has two poles on the complex-frequency plane, near which the system follows a simple set of equations described by the temporal coupled-mode theory (TCMT) [66, 202, 60, 178, 181]. As a starting point, we "turn off" the radiation loss and absorption loss of the resonances, and the resonance amplitudes A'_j $(j = 1, 2)$ evolve as

$$\frac{d}{dt}\begin{pmatrix} A'_1 \\ A'_2 \end{pmatrix} = -i\begin{pmatrix} \omega'_1 & \omega'_{12} \\ \omega'_{21} & \omega'_2 \end{pmatrix}\begin{pmatrix} A'_1 \\ A'_2 \end{pmatrix}, \tag{6.3}$$

where ω'_j are the resonant frequencies, and ω'_{12}, ω'_{21} are the near-field coupling strengths. We proceed by changing to the basis A_j (without the primes) that diagonalizes the matrix (so ω_{12} is now zero), which is always possible because the matrix is Hermitian by energy conservation. In the new basis, we "turn on" the low losses of the resonances, and couple them to the spherical wave in channel (l, σ),

$$\frac{d}{dt}\begin{pmatrix} A_1 \\ A_2 \end{pmatrix} = \left[-i\begin{pmatrix} \omega_1 & 0 \\ 0 & \omega_2 \end{pmatrix} - \begin{pmatrix} \gamma_1 & \gamma_{12} \\ \gamma_{12} & \gamma_2 \end{pmatrix} - \begin{pmatrix} \xi_1 & 0 \\ 0 & \xi_2 \end{pmatrix}\right]\begin{pmatrix} A_1 \\ A_2 \end{pmatrix} + \begin{pmatrix} \kappa_1 \\ \kappa_2 \end{pmatrix} s^+_{l,\sigma}, \tag{6.4}$$

where γ_j are radiative decay rates, ξ_j are absorptive decay rates, and κ_j are coupling coefficients to the incoming wave. Because both resonances radiate into the same channel $s^{\pm}_{l,\sigma}$, the radiative coupling rate γ_{12} is necessary to ensure energy conservation [202]. Absorptions do not have such constraints, so we let $\xi_{12} = 0$ for simplicity. Meanwhile,

the outgoing wave is given by

$$s^{-}_{l,\sigma} = s^{+}_{l,\sigma} + d_1 A_1 + d_2 A_2, \tag{6.5}$$

where d_j are coupling coefficients, and the first term $s^{-}_{l,\sigma} = s^{+}_{l,\sigma}$ comes from the planewave itself [15]. Since we are considering nanostructures, we exclude the direct (non-resonant) background scattering process related to Fano resonances [178, 181]; only the resonant scattering processes are considered here. The normalizations are chosen such that $|A_j|^2$ is the electromagnetic energy in each resonance and $|s^{\pm}_{l,\sigma}|^2$ is the incoming and outgoing power. For low absorption loss, we can apply energy conservation and time reversal symmetry [202] to eliminate many unknowns and get $\kappa_j = d_j$, $\gamma_j = -d_j^2/2$, and $\gamma_{12} = -d_1 d_2/2$. Solving Eqs 6.4 and 6.5 for a steady-state solution at frequency ω gives the reflection coefficient $s^{-}_{l,\sigma}/s^{+}_{l,\sigma}$ as

$$R_{l,\sigma} = 1 - 2\frac{\left[i(\omega_2 - \omega) + \xi_2\right]\gamma_1 + \left[i(\omega_1 - \omega) + \xi_1\right]\gamma_2}{\left[i(\omega_1 - \omega) + \gamma_1 + \xi_1\right]\left[i(\omega_2 - \omega) + \gamma_2 + \xi_2\right] - \gamma_1\gamma_2}, \tag{6.6}$$

which yields the scattering cross sections spectrum through Eq 6.2.

6.4 Scattering Dark State

When there is negligible absorption loss ($\xi_1 = \xi_2 = 0$), the particle becomes transparent in this channel ($R_{l,\sigma} = 1$) at the "transparency frequency," defined as

$$\omega = \frac{\omega_1\gamma_2 + \omega_2\gamma_1}{\gamma_1 + \gamma_2} \equiv \omega_{\mathrm{t}}. \tag{6.7}$$

Since ω_t is simply a weighted average of the two resonant frequencies, it *always* exists, regardless of the radiative decay rates and other system details. We therefore conclude that the scattering dark state is a general phenomenon in the low-absorption limit when two resonances in the same channel are simultaneously excited.

In the presence of material loss, the scattering cross section cannot be strictly zero even at ω_t. This can be viewed as a consequence of the optical theorem [15], which relates the forward scattering amplitude to the total extinction cross section (scattering plus absorption). Taking $\xi_1 = \xi_2 = \xi$ and $\gamma_1 = \gamma_2 = \gamma$, the reflection coefficient at ω_t is $R_{l,\sigma} \approx 1 - 16\gamma\xi/(\omega_1 - \omega_2)^2$ to leading order of the absorptive decay rate ξ. So, the "low-absorption limit" can be quantified as $\xi \ll (\omega_1 - \omega_2)^2/\gamma$.

The scattering dark state occurs when the two outgoing waves $d_1 A_1$ and $d_2 A_2$ have equal magnitude and opposite phase, as illustrated in Figure 6.2b. When $\omega < \omega_1 < \omega_2$ or when $\omega > \omega_2 > \omega_1$, the two outgoing waves add up in phase (shown in blue dotted arrows). When $\omega_1 < \omega < \omega_2$, the two add up out of phase (shown in green dashed arrows). At the transparency frequency ω_t, the two waves exactly cancel each other (shown in red solid arrows), making the particle completely transparent in the (l, σ) channel.

6.5 Choice of Basis

We now address the choice of basis. In the derivation above, we choose a basis to express the two resonances such that $\omega_{12} = 0$ (no coupling in the absence of loss), and the scattering dark state arises from interference in the far-field radiation of the two resonances. The underlying system is independent of the basis, and we may as well choose a basis that diagonalizes the radiative-decay-rate matrix (so that $\gamma'_{12} = 0$, no

radiative coupling; the prime denotes variables in that basis); in such a basis, Eqs 6.4 and 6.5 become

$$\frac{d}{dt}\begin{pmatrix} A_1' \\ A_2' \end{pmatrix} = \left[-i \begin{pmatrix} \omega_1' & \omega_{12}' \\ \omega_{12}' & \omega_2' \end{pmatrix} - \begin{pmatrix} \gamma_1' & 0 \\ 0 & 0 \end{pmatrix} - \begin{pmatrix} \xi_1' & \xi_{12}' \\ \xi_{12}' & \xi_2' \end{pmatrix} \right] \begin{pmatrix} A_1' \\ A_2' \end{pmatrix} + \begin{pmatrix} \kappa_1' \\ 0 \end{pmatrix} s_{l,\sigma}^{+}, \tag{6.8}$$

$$s_{l,\sigma}^{-} = s_{l,\sigma}^{+} + d_1' A_1',$$

with $\omega_1' = (\omega_1\gamma_1 + \omega_2\gamma_2)/(\gamma_1+\gamma_2)$, $\omega_2' = (\omega_1\gamma_2 + \omega_2\gamma_1)/(\gamma_1+\gamma_2)$, $\omega_{12}' = (\omega_2 - \omega_1)\sqrt{\gamma_1\gamma_2}/(\gamma_1+\gamma_2)$, $\gamma_1' = \gamma_1+\gamma_2$, and $\kappa_1' = d_1' = \sqrt{d_1^2+d_2^2}$. The transformation of the absorptive decay rates is similar. We see that $\gamma_2' = 0$ (and so $\kappa_2' = d_2' = 0$). So, in this basis, resonance A_1' radiates, but resonance A_2' does not; this is exactly the subradiant-superradiant model [245, 113, 140, 107, 1]. Intuitively, this choice of basis is possible because there is only one channel of radiation, which can be incorporated into just one degree of freedom. The scattering dark state still exists in the low-absorption limit at the frequency given by Eq 6.7. But, now it is the direct near-field coupling ω_{12}' that leads to transparency. We therefore conclude that the scattering dark state can be interpreted as arising from the far-field coupling of two radiating resonances, or arising from the near-field coupling of one radiating resonance and a non-radiating resonance. Both interpretations are valid; it is only a matter of basis choice.

6.6 Arbitrary Number of Resonances

Above, we considered the case of two spectrally overlapping resonances in the same channel. Here, we consider the more general case with arbitrarily many overlapping resonances in channel (l,σ). The temporal coupled-mode theory equations is now written

in matrix form:

$$\begin{aligned} \frac{dA}{dt} &= \left(-i\Omega - \Gamma - \Xi\right) A + K^{\mathrm{T}} s^{+}_{l,\sigma}, \\ s^{-}_{l,\sigma} &= s^{+}_{l,\sigma} + DA. \end{aligned} \tag{6.9}$$

Similar to the two-resonance case, we choose the basis such that Ω is diagonal (so that the resonances are orthogonal when we take the loss to zero), and we ignore any direct (non-resonant) background scattering process. With n resonances, the matrices are

$$\begin{aligned} A &= \begin{pmatrix} A_1 \\ A_2 \\ \vdots \\ A_n \end{pmatrix}, & \Omega &= \begin{pmatrix} \omega_1 & 0 & \dots & 0 \\ 0 & \omega_2 & \dots & 0 \\ \vdots & \vdots & \ddots & \vdots \\ 0 & 0 & \dots & \omega_n \end{pmatrix}, \\ \Gamma &= \begin{pmatrix} \gamma_1 & \gamma_{12} & \cdots & \gamma_{1n} \\ \gamma_{21} & \gamma_2 & \cdots & \gamma_{2n} \\ \vdots & \vdots & \ddots & \vdots \\ \gamma_{n1} & \gamma_{n2} & \cdots & \gamma_n \end{pmatrix}, & \Xi &= \begin{pmatrix} \xi_1 & \xi_{12} & \cdots & \xi_{1n} \\ \xi_{21} & \xi_2 & \cdots & \xi_{2n} \\ \vdots & \vdots & \ddots & \vdots \\ \xi_{n1} & \xi_{n2} & \cdots & \xi_n \end{pmatrix}, \\ K &= \begin{pmatrix} \kappa_1, & \kappa_2, & \dots & \kappa_n \end{pmatrix}, & D &= \begin{pmatrix} d_1, & d_2, & \dots & d_n \end{pmatrix}. \end{aligned} \tag{6.10}$$

The meaning of these variables are the same as Eqs. (4) and (5) in the main text. With incoming light at frequency ω, Eq. (6.9) gives the steady-state reflection coefficient $s^{-}_{l,\sigma}/s^{+}_{l,\sigma}$ as

$$R_{l,\sigma} = 1 + D\left[i(\Omega - \omega I_n) + \Gamma + \Xi\right]^{-1} K^{\mathrm{T}}, \tag{6.11}$$

where I_n is the n-by-n identity matrix. The particle becomes transparent in this channel when $R_{l,\sigma} = 1$. Optical theorem suggests that zero scattering can only occur with zero absorption; therefore, we consider the small-absorption limit, $\Xi = 0$. Energy

conservation and time reversal symmetry require the matrices to satisfy $K = D$, $D^\dagger D = 2\Gamma$, and $D^* = -D$, as shown in Ref. [202]. Therefore, the transparency condition can be simplified to

$$D\left[i(\Omega - \omega I_n) - \frac{1}{2}D^{\mathrm{T}}D\right]^{-1} D^{\mathrm{T}} = 0. \tag{6.12}$$

By rewriting the matrix inverse using the Woodbury matrix identity, we see that this condition is satisfied when $D(\Omega - \omega I_n)^{-1}D^{\mathrm{T}} = 0$, which can be written as

$$\sum_{j=1}^{n} \frac{\gamma_j}{\omega_j - \omega} = 0 \tag{6.13}$$

because $d_j^2 = -2\gamma_j$.

This simple expression yields all the transparency frequencies. We can immediately observe that, as we gradually increase ω, the left-hand side of Eq. (6.13) swings from $-\infty$ to $+\infty$ in each interval between successive resonant frequencies. So, there is one transparency frequency in each of these $n-1$ intervals. For example, there is one transparency frequency with two resonances, two transparency frequencies with three resonances, *etc.*

Similar to the two-resonance case, it is possible to choose a basis that diagonalizes the radiative-decay-rate matrix Γ. The matrix $\Gamma = -\frac{1}{2}D^{\mathrm{T}}D$ is a rank-one matrix, so only one of its n eigenvalues is non-zero. This non-zero eigenvalue is $-\frac{1}{2}\sum_{j=1}^{n} d_j^2 = \sum_{j=1}^{n}\gamma_j$. Therefore, in the basis where Γ is diagonal, one resonance would radiate while the other $n-1$ resonances do not. Intuitively, this is because there is only one channel of radiation.

This brings our major conclusion that the scattering dark state arises generally with multiple resonances in the same channel. It does not matter how many resonances there are, or how narrow or broad each resonance is. Therefore the suppressed scatter-

ing is more general than the discrete-coupled-to-continuum or narrow-coupled-to-broad scenarios in standard Fano resonances [43, 178].

The scattering dark state is similar to the "bound state in the continuum" we have discussed in Chapters 2 to 4 because both phenomena arise from destructive interference of outgoing waves. However, a scattering dark state is *not* a bound state. Eq 6.4 indicates that the resonance amplitudes decay to zero in the absence of the incoming wave—they cannot sustain oscillation on their own, even at the transparency frequency. Also, the particle becomes transparent at steady state, but at the transient stage when $d_1 A_1 + d_2 A_2 = 0$ has not been established, the particle is opaque. The exception is when the resonant frequencies are degenerate ($\omega_1 = \omega_2$); in that case we do obtain a bound state.

6.7 Example: Lossless Metal

Lastly, we provide a few explicit examples to illustrate the concepts discussed above. First, we consider a multi-layer sphere (schematically shown in the inset of Figure 6.3a) that consists of concentric metallic core, dielectric spacer, and metallic shell. For the first example, we describe the metal layers using the Drude model with negligible damping $\epsilon(\omega) = 1 - \omega_\mathrm{p}^2/\omega^2$, let the dielectric layer be $\epsilon = 2.04$, and let the surrounding medium be air. For a particle of size $[r_1, r_2, r_3] = [0.005, 0.073, 0.132]\lambda_\mathrm{p}$ (where $\lambda_\mathrm{p} = 2\pi c/\omega_\mathrm{p}$ is the plasma wavelength, and c is the speed of light in vacuum), the exact scattering cross section is plotted as the black line in Figure 6.3a; these data are calculated using the Mie solution with the transfer matrix method [168]. The electric dipole channel TM_1 ($l = 1$, $\sigma = \mathrm{TM}$) dominates in the frequency range plotted; contributions from other channels are six orders of magnitude smaller. There is no absorption loss in this example, and

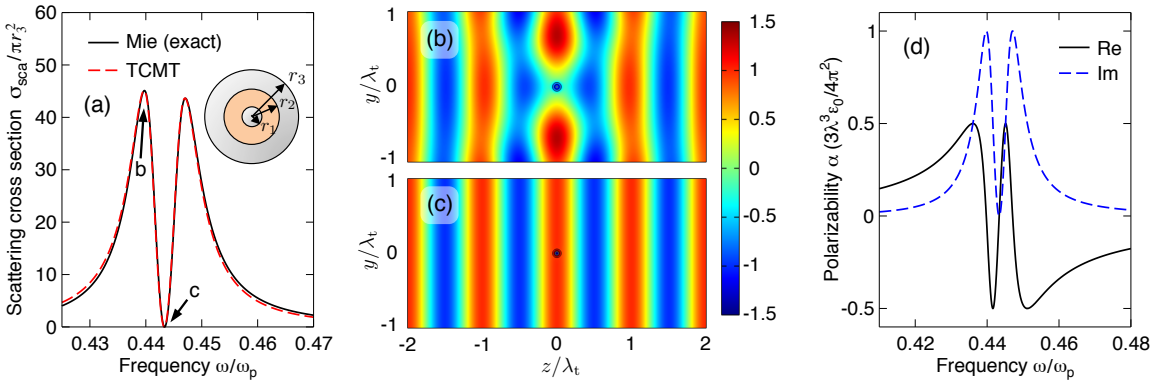

Figure 6.3: Scattering dark state in a doubly resonant nanosphere without absorption loss. (a) The particle's scattering cross section in air, calculated by the Mie solution (black solid line) and the temporal coupled-mode theory (red dashed line). The inset schematically shows the particle's composition: concentric metallic core, silica spacer ($\epsilon = 2.04$), and metallic shell, with radii $[r_1, r_2, r_3] = [0.005, 0.073, 0.132]\lambda_p$. The metal is described by the Drude model with plasma frequency ω_p and negligible damping. In the plotted range of frequency, the cross section is dominated by the TM_1 channel (electric dipole). (b, c) Steady-state electric-field pattern, $\mathrm{Re}(E_x)$, with an incident wave $\mathbf{E}_{inc} = e^{ikz}\hat{\mathbf{x}}$ that is (b) at the resonant frequency ω_1 and (c) at the transparency frequency ω_t. Animations of the field propagation are shown in Supplementary Movies S1 and S2. (d) Electric polarizability of this particle in air. At the transparency frequency, the large slope of $\mathrm{Re}(\alpha)$ can give rise to slow group velocity for a wave packet propagating through a collection of such particles.

as expected, the scattering cross section goes to zero at a transparency frequency ω_t in between the two resonance peaks. We plot the steady-state electric-field profile at one of the resonant frequencies and at ω_t in Figure 6.3b and 3c. The field profile confirms that the particle becomes invisible at ω_t. We note that the scattering dark state is robust: perturbations of parameters (such as the layer thicknesses and the refractive indices) only shift the frequency where it occurs, consistent with our discussion above.

Figure 6.3a also shows the prediction from the temporal coupled-mode theory (red dashed line). We obtain the parameters in TCMT without doing curve fitting. Instead, we locate the two poles of the exact reflection coefficient $R_{1,TM}$ (from the Mie solution)

on the complex-frequency plane. The pole locations, $0.4411 - 0.00282i$ and $0.4456 - 0.00297i$ (in units of ω_p), yield the TCMT parameters $\omega_1 = 0.4397$, $\gamma_1 = 0.00285$, $\omega_2 = 0.4470$, and $\gamma_2 = 0.00294$ when compared to the denominator of Eq 6.6. The TCMT prediction agrees excellently with the exact Mie solution even without fitting.

A collection of these nanospheres with subwavelength spacing can act as an effective medium. In general, the scattering properties of such closely spaced nanospheres are substantially different from that of an individual nanosphere in free space. However, when an individual particle is transparent, we can use the superposition principle to conclude that a collection of particles is also transparent even when closed spaced. So, near ω_t, we may infer the properties of the effective medium from an individual particle in free space, using the standard mixing formula [194]. Near ω_t, the real part of the individual particle's electric polarizability changes rapidly (Figure 6.3d), so the refractive index n_{eff} of the effective medium changes rapidly. This leads to a suppressed group velocity, $v_g = d\omega/dk = c/(n_{\text{eff}} + \omega dn_{\text{eff}}/d\omega)$, for a wave packet propagating through this medium, analogous to the atomic version of electromagnetically induced transparency [61, 65] and similar to the metamaterial realization using subwavelength optical antennas [156, 245, 113]. For example, for a random collection of the above-mentioned particles with concentration $N = (\lambda_t/3)^{-3}$ (where $\lambda_t = 2\pi c/\omega_t$ is the transparency wavelength), the group velocity is $v_g \approx c/200$ at transparency.

6.8 Example: Metal with Loss

Next, we provide examples using realistic materials with loss. Consider the same multilayer sphere schematically shown in the inset of Figure 6.3a, but with the metal layers being silver (complex permittivity from experimental data [155]) instead. Similar

metal-dielectric-metal nanospheres have been synthesized [10, 140] and studied numerically [168, 227, 236, 70, 195] in prior works. To mimic potential experimental condition, we consider such nanospheres suspended in an aqueous solution ($\epsilon = 1.77$). Figure 6.4a shows the exact scattering cross section for a particle of size $[r_1, r_2, r_3] = [20, 31, 52]$ nm. This particle is large enough that the electrostatic approximation is not appropriate, but small enough that the TM_1 channel dominates. Since the absorption and radiation loss is relatively large, the prediction from TCMT is not as accurate in this example; nonetheless, we still observe a clear dip in the scattering cross section that is suppressed by more than a factor of ten compared to the on-resonance values. Such nanoparticles can be useful for the application of transparent projection screens using resonant scattering of nanoparticles [75]. In the presence of absorption loss, the amount of scattering at ω_t does vary with perturbations. As discussed earlier, $R_{l,\sigma} \approx 1 - 16\gamma\xi/(\omega_1 - \omega_2)^2$ depends on the absorptive loss, radiative loss, and the frequency difference between the two resonances. However, the dip still exists with reasonable perturbations: for the current structure, the scattering minimum remains at least 10 times smaller than the scattering maximum with a 10% change in any thickness or refractive index parameter.

Another possible application of the scattering dark state is to selectively allow only a narrow bandwidth of light to pass through a medium. In a medium with dilute suspension of particles, the transmission is given by the Beer-Lambert law $T = \exp(-\sigma_{\text{ext}} N l)$, where $\sigma_{\text{ext}} = \sigma_{\text{sca}} + \sigma_{\text{abs}}$ is the extinction cross section of an individual particle, N is its number density, and l is the path length of the medium. Typically, resonant nanoparticles suppress transmission at a target wavelength. But with the scattering dark state, we may enhance transmission at a target wavelength instead. Figure 6.4b shows one example using the same type of silver-silica-silver nanosphere, designed to allow light with wavelength around 600 nm to pass through.

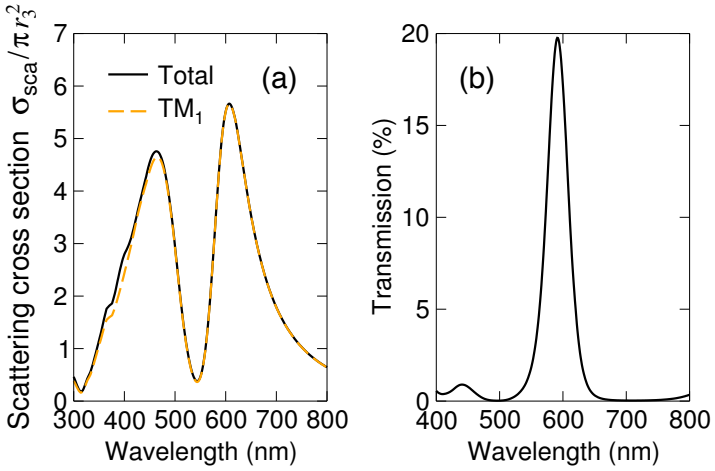

Figure 6.4: Scattering dark state in a doubly resonant nanosphere with absorption loss. (a) The scattering cross section of a particle consisting of concentric silver core, silica spacer ($\epsilon = 2.04$), and silver shell, with radii of the layers being $[r_1, r_2, r_3] = [20, 31, 52]$ nm. The cross section is calculated with the Mie solution with the particle in water ($\epsilon = 1.77$) and the complex permittivity of silver taken from experimental data [155]. Solid line shows the sum from all channels, and dashed line shows the contribution from the TM_1 channel. Animations of the field propagation at 607 nm and 544 nm are shown in Supplementary Movies S3 and S4. (b) Transmission spectrum for a dilute aqueous solution of nanoparticles of size $[r_1, r_2, r_3] = [33, 55, 77]$ nm, with the number density times path length being 7×10^9 cm^{-2}.

6.9 Example: Dielectric Particle

Our theory derivation suggests that the scattering dark state is not limited to any particular type of resonance; nor is it limited to any particular radiation channel. To illustrate these points, we consider a purely dielectric nanostructure that supports whispering-gallery resonances in multiple angular momentum channels. Specifically, we consider a nanosphere consisting of four concentric layers that alternate between a high-index dielectric ($\epsilon = 12$, can be silicon or gallium arsenide) and a low-index dielectric ($\epsilon = 1$, can be a transparent aerogel [207]). For a particle of size $[r_1, r_2, r_3, r_4] = [40, 90, 150, 160]$ nm, Figure 6.5 shows the exact scattering cross section divided into individual channels as in Eq 6.2. Scattering dark states can be seen in the TE_1, TE_2, and TE_3 channels. Note that due to the spectral overlap of the different channels, the particle may become transparent to one particular channel but not the rest; in principle, it is possible to probe the individual channels by preparing special excitation waves (for example, a tightly-focused beam can isolate the dipole channels [136]).

6.10 Conclusions

In summary, we have presented an analytical treatment for the general problem of light scattering from a multi-resonant nanostructure that is spherical or non-spherical but subwavelength in size. With n resonances in the same channel, $n - 1$ scattering dark states arise when the absorption loss is negligible; this result is independent of the radiative decay rates and many other system details. The scattering dark state can be interpreted as arising from far-field or near-field coupling, depending on the choice of basis. This theoretical treatment should improve the understanding of scattering dark

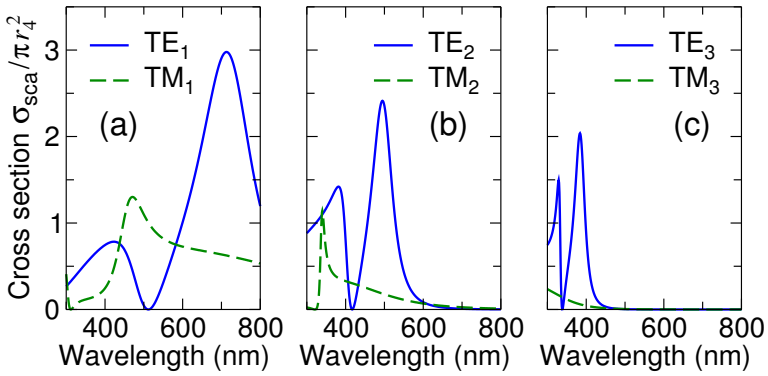

Figure 6.5: Scattering dark states in individual channels of a nanosphere made of dielectrics only. The particle consists of four concentric layers, with relative permittivities being $[\epsilon_1, \epsilon_2, \epsilon_3, \epsilon_4] = [1, 12, 1, 12]$ and radii being $[r_1, r_2, r_3, r_4] = [40, 90, 150, 160]$ nm. (a)-(c) The particle's scattering cross section in air, separated into different angular momentum and polarization channels. Scattering dark states can be seen in the TE_1, TE_2, and TE_3 channels.

states and provide guidance for future works on this topic.

It will be interesting to consider perturbations that break the spherical symmetry of the scatterer, allowing each resonance to couple to multiple channels. The interference between multiple resonances in multiple channels may lead to even richer phenomena [226, 199, 140, 202].

Chapter 7

Optimization of sharp and viewing-angle-independent structural color*

7.1 Introduction

Structural color is a narrow bandwidth (color) of reflected or scattered light determined by a wavelength-scale geometry rather than by the frequency response of the materials [97], and is important in a wide range of applications from pigments and displays to imaging and biosensing [6, 164, 95, 165]. Although it arises in both natural structures [221, 167, 231, 184, 219] and synthetic designs, all previous work on structural color has achieved either narrow bandwidth or angular insensitivity, but not both [16, 91, 192, 26, 239, 141, 36, 210, 215, 62, 47, 209, 119, 185, 120, 21, 147, 22, 4, 82]. Here, however, we show that both goals can be achieved simultaneously: a narrow 7% bandwidth can be obtained for reflection at all observation angles (0–90°) with directional illumination of an optimized structure. Besides the bandwidth (color saturation), the reflectivity's peak wavelength (hue) and peak intensity (brightness) are also insensitive to the viewing angle. The structure consists of a collection of wavelength-scale

*This chapter is based on: C. W. Hsu, O. D. Miller, S. G. Johnson, and M. Soljačić, "Optimization of sharp and viewing-angle-independent structural color," arXiv:1410.8605 (2014).

ring scatterers amenable to fabrication by direct laser writing (multiphoton lithography) [33, 64, 110, 206, 11], and is optimized so that constructive interference occurs only in a narrow bandwidth but with a dipole-like broad-angle pattern. We perform the optimization using a simplified semi-analytical model, and validate our results via 3D boundary-element method (BEM) simulations. One immediate application of this design is for angle-independent viewing of transparent displays based on wavelength-selective light scattering [75].

Previous work on synthetic structural color has explored a wide range of designs, but none has been able to achieve narrow bandwidth (sharp color) and angular insensitivity (wide viewing angle) simultaneously. Multilayer films [16, 91, 192], periodically-modulated surfaces [26, 239, 141], and three-dimensional photonic crystals [80] reflect light only at a discrete set of angles rather than omnidirectionally. Amorphous structures scatter light to all directions [36, 210, 215, 62, 47, 209, 119, 185, 120], but their colors are not as sharp and are viewing-angle dependent under directional illumination [21, 147]. The dipole scattering from resonant spherical nanoparticles has a broad-angle pattern, but sharp colors cannot be achieved because dielectric particles tend to have multiple overlapping resonances [22, 73], and metallic particles are limited by absorption loss which broadens the resonances [75, 212, 132]. Topological optimization has recently been used to design structural colors [4, 82] but was focused on maximizing the intensity of a prescribed color, rather than on minimizing the bandwidth or the angular dependence. From these prior studies, it appears that simple hand-designed geometries cannot achieve both narrow bandwidth and broad viewing angle. Therefore, we use numerical optimization to explore to what extent these two properties can be achieved simultaneously. We focus on the case of illumination from a directional light source, as is the case for viewing "structurally painted" objects under bright sunlight, for sensing

applications, and for the transparent display application described in Chapter 5.

7.2 Structure Factor and Interference of Scattered Waves

We start by considering light scattering from a collection of point scatterers where the electric dipole scattering dominates. There are a variety of ways to realize this model system; later in this chapter, we describe a simple and realistic realization using stacked dielectric rings. Here, scatterer j has electric dipole moment $\mathbf{p}_j = 4\pi\epsilon_0\alpha_j\mathbf{E}_0$, where α_j is the electric polarizability with units of volume, ϵ_0 is the vacuum permittivity, and $\mathbf{E}_0$ is the incident electric field. Neglecting multiple scattering, the differential scattering cross section from this collection is [79]

$$\frac{d\sigma}{d\Omega} = k^4 \left|\hat{\mathbf{e}}_{\text{in}} \cdot \hat{\mathbf{e}}^*_{\text{out}}\right|^2 S(\mathbf{q}), \tag{7.1}$$

where $k = 2\pi/\lambda$ is the wavenumber, λ is the wavelength, $\hat{\mathbf{e}}_{\text{in}}$ and $\hat{\mathbf{e}}_{\text{out}}$ are the polarization vectors of the incident and the scattered light. Coherent interference among radiation from different scatterers gives rise to the "structure factor"

$$S(\mathbf{q}) = \left|\sum_j \alpha_j e^{i\mathbf{q}\cdot\mathbf{r}_j}\right|^2. \tag{7.2}$$

Here, $\mathbf{r}_j$ is the position of the j-th scatterer, and $\mathbf{q}$ is the momentum transfer vector

$$\mathbf{q} = k(\hat{\mathbf{n}}_{\text{in}} - \hat{\mathbf{n}}_{\text{out}}), \tag{7.3}$$

with $\hat{\mathbf{n}}_{\text{in}}$ and $\hat{\mathbf{n}}_{\text{out}}$ being the propagation direction of the incident and the scattered light. Note that we include α_j in the definition of $S(\mathbf{q})$ to account for different types of

scatterers, but for simplicity we consider frequency-independent scalar α_j (no metallic particles where α_j depends strongly on frequency). The assumptions in this model—that dipole scattering dominates with a constant scalar polarizabilty and that multiple scattering is negligible—are valid for subwavelength weak scatterers and can be realized in a variety of physical systems. In this model system, the angle and wavelength dependence comes from $S(\mathbf{q})$ and can be calculated efficiently for fast optimization.

The interference can give rise to coloration through a wavelength-selective $S(\mathbf{q})$. However, this wavelength dependence is coupled to the incident and the viewing angles through Eq. (7.3), so structural colors are typically angle dependent. For example, periodic structures scatter strongly when $\mathbf{q}$ lies on the reciprocal lattice [79], and the peak wavelength depends sensitively on the angles. The $S(\mathbf{q})$ of amorphous structures depends only on $|\mathbf{q}|$, so the peak wavelength is a function of the angle between illumination and view [21, 147]; for a fixed illumination direction, the peak wavelength varies with viewing angle, as given by Eq. (7.3). Such typical behavior of a viewing-angle-dependent structural color is schematically illustrated in Figure 7.1(a).

We illustrate the desired behavior in Figure 7.1(b), where the structural color is viewing-angle independent when illuminated from a fixed direction. This requires an $S(\mathbf{q})$ that reaches its maximum at the target wavelength (corresponding to the desired color) and is low at other wavelengths, with very little variation when the viewing angle is varied. We use numerical optimization to search for such structures.

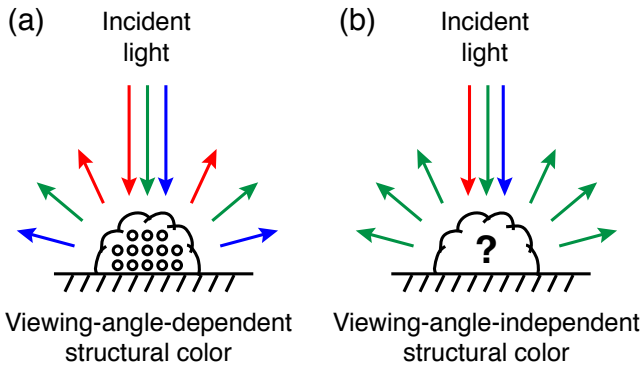

Figure 7.1: (a) Schematic illustration of a typical structurally-colored object under directional white-light illumination, where its color depends strongly on the viewing angle. (b) Schematic illustration of an object with a structural color that is independent of viewing angle under directional illumination.

7.3 Optimization

We define a figure of merit (FOM) that, as we demonstrate below, captures the desired characteristics,

$$\text{FOM} = \frac{A}{B + C}, \tag{7.4}$$

where A is $S(\mathbf{q})$ at the target wavelength averaged over the viewing angles, B is $S(\mathbf{q})$ averaged over both the viewing angles and the wavelengths in the visible spectrum, and C is the maximum value in the visible spectrum for the standard deviation of $S(\mathbf{q})$ with respect to the viewing angles. We take the illumination to be in the z direction ($\hat{\mathbf{n}}_{\text{in}} = \hat{\mathbf{z}}$), and the angular average and standard deviation are calculated by integrating over all solid angles $\hat{\mathbf{n}}_{\text{out}}$ in the backward hemisphere (*i.e.*, all $\hat{\mathbf{n}}_{\text{out}}$ with $\hat{\mathbf{n}}_{\text{out}} \cdot \hat{\mathbf{z}} \leq 0$), which are the typical angles when viewing the structure's color and for applications such as displays and sensing. We search for structures in the $4N$-dimensional parameter space (given by $\{\alpha_j, \mathbf{r}_j\}_{j=1}^{N}$) that maximize this FOM.

Optimization frequently led to structures where the discrete points arrange themselves into several rings aligned along the z axis to eliminate the azimuthal part of the viewing-angle dependence. With this insight, we focus our attention on structures made of rings aligned along the z axis. Instead of parameterizing coordinates of the individual point scatterers, we now directly parameterize coordinates of the rings to reduce the dimensionality of the search space and to avoid spurious local optima. The computation is further accelerated by analytically summing over point scatterers in a ring (assuming closely spaced points), as

$$S(\mathbf{q}) = \left| \sum_j w_j e^{iq_z z_j} J_0(q_\rho \rho_j) \right|^2 , \tag{7.5}$$

where the new summation is over the constituent rings, q_z and q_ρ are the z and the radial components of the $\mathbf{q}$ vector, and J_0 is the Bessel function. Each ring is specified by its z coordinate z_j, its radius ρ_j, and its weight w_j (which is given by the number of point scatterers in this ring times the polarizability per scatterer).

We then optimize the ring-shaped structures. An appropriate search strategy is important; directly applying global or local optimization algorithms tends to yield very suboptimal results due to the high dimensionality of the parameter space, the unevenness of the FOM landscape, and the sensitivity on initial guess. We find that a step-wise procedure [131] is very effective for this problem. Starting from vacuum, we add rings one by one. Each time a new ring is added, a global optimization is performed on parameters $\{z_j, \rho_j, w_j\}$ of the new ring only, keeping the existing parameters fixed; then a local optimization on all of the parameters is performed. This procedure keeps the FOM high as the parameter space expands its dimensionality, and global optimization is used only for the more manageable low-dimensional searches. After some experimentation

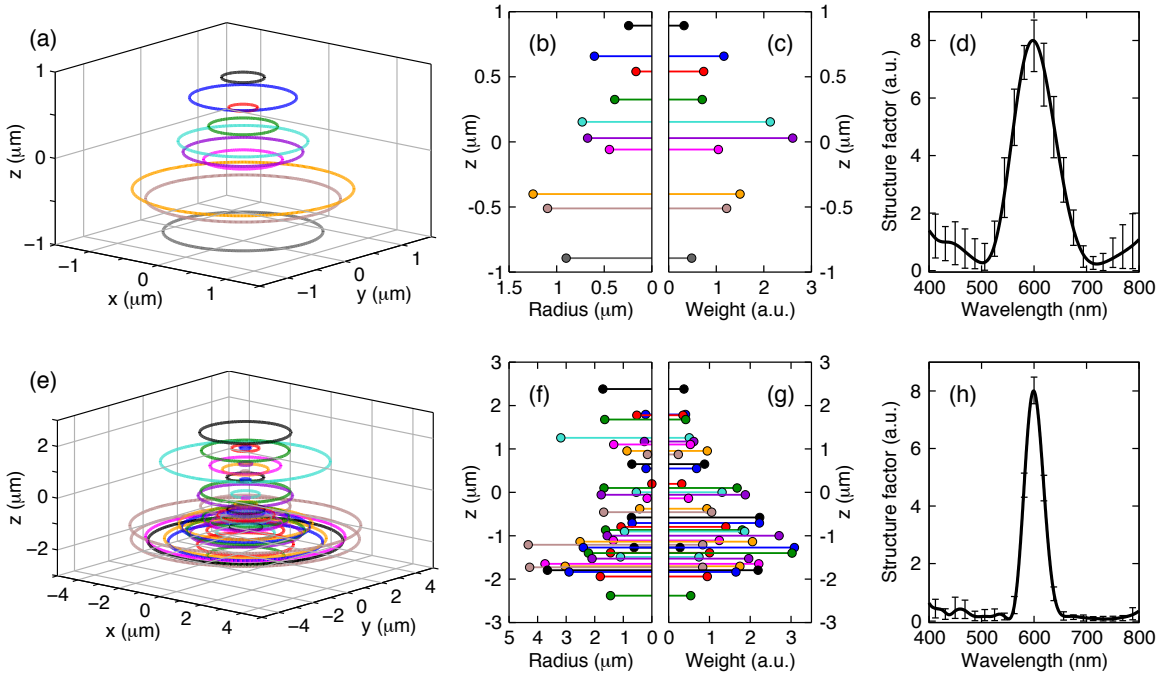

Figure 7.2: Structures optimized for a structural color that is independent of the viewing angle. (a) Visualization of an optimized structure consisting of dipole scatterers that make up 10 rings. (b), (c) Radii and weights of the rings. (d) Calculated structure factor for light incident along the z direction ($\hat{\mathbf{n}}_{\text{in}} = \hat{\mathbf{z}}$) and scattered into directions in the backward hemisphere (all solid angles $\hat{\mathbf{n}}_{\text{out}}$ with $\hat{\mathbf{n}}_{\text{out}} \cdot \hat{\mathbf{z}} \leq 0$). The solid curve is $S(\mathbf{q})$ averaged over all of these viewing angles, and the vertical bars represent the 10th and the 90th percentiles (*i.e.*, $S(\mathbf{q})$ range spanned by 80% of the viewing angles). (e)–(h) Same plots for an optimized structure with 40 rings.

with a free optimization package [83], we chose well known local [205] and global [88] search algorithms and implemented our FOM [Eq. (7.4)] to four-digit accuracy in the high-performance dynamic language Julia [14]. The best structure is picked from results of several independent runs.

7.4 Results

Figure 7.2 shows the optimized structures and their corresponding structure factors. The wavelength window is 400–800 nm, and the target wavelength is 600 nm; structures for other target wavelengths (with corresponding shift in the window) can be obtained through scaling the structure sizes since Eq. (7.1) is scale invariant. With 10 rings (shown in the upper panel), the structure reaches FOM = 2.54; its color sharpness is characterized by $A/B = 3.51$, and its viewing-angle independence is characterized by $A/C = 9.15$. With 40 rings (shown in the lower panel), the optimization discovers a structure that reaches FOM = 5.51, with its color sharpness characterized by $A/B = 7.64$ and angle independence by $A/C = 19.8$. The full width at half maximum (FWHM) of this structure factor is only 43 nm at $\lambda_0 = 600$ nm, corresponding to a narrow 7% bandwidth. As shown in Figure 7.3, the hue (peak wavelength), the brightness (peak height), and the saturation (contrast between the target color and the other colors) are all nearly independent of the viewing angle. We validate this design by realistic simulations below.

Interestingly, the parameters of these optimized structures (as shown in Figure 7.2 and tabulated in Tables 7.1 and 7.2) do not exhibit perceivable patterns, suggesting that hand design would not be a good route. The optimization procedure discovers structures with very different parameters but comparable performance, suggesting that we can pick structures more amendable to fabrication without sacrificing much performance.

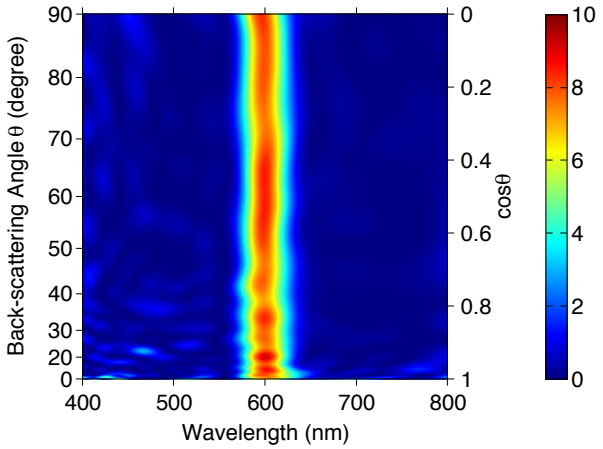

Figure 7.3: Scattering-angle-resolved spectrum of the structure factor when the 40-ring structure is illuminated along the z direction. The y-axis scale accounts for the weight in the solid angle integration, $|\sin\theta \mathrm{d}\theta| = |\mathrm{d}(\cos\theta)|$.

Table 7.1: Parameters of the optimized 10-ring structure shown in Figure 7.2(a-c).

z_j (μm)	ρ_j (μm)	w_j (a.u.)
0.893	0.243	0.323
0.658	0.603	1.161
0.540	0.167	0.736
0.325	0.390	0.705
0.153	0.732	2.135
0.029	0.675	2.606
-0.059	0.446	1.044
-0.401	1.248	1.500
-0.511	1.096	1.218
-0.893	0.900	0.484

Table 7.2: Parameters of the optimized 40-ring structure shown in Figure 7.2(e-g).

z_j (μm)	ρ_j (μm)	w_j (a.u.)	z_j (μm)	ρ_j (μm)	w_j (a.u.)
2.380	1.714	0.375	-0.795	1.080	1.401
1.794	0.217	0.413	-0.868	1.621	1.803
1.776	0.526	0.352	-0.902	0.955	1.864
1.677	1.651	0.418	-0.999	1.566	2.706
1.257	3.187	0.506	-1.109	1.350	1.241
1.171	0.261	0.615	-1.137	2.515	2.056
1.103	1.335	0.533	-1.207	4.329	0.836
0.954	0.870	0.947	-1.271	0.621	0.279
0.872	0.154	0.238	-1.272	2.399	3.083
0.650	0.699	0.880	-1.394	1.448	1.003
0.549	0.205	0.685	-1.399	2.220	3.024
0.195	0.000	0.322	-1.488	1.099	0.742
0.100	1.678	1.678	-1.526	2.095	1.962
0.002	0.543	1.309	-1.647	3.741	2.208
-0.056	1.774	1.880	-1.702	3.036	1.747
-0.138	0.163	0.486	-1.727	4.281	0.834
-0.377	0.426	0.939	-1.795	3.657	2.190
-0.457	1.686	1.054	-1.835	2.899	1.649
-0.578	0.714	2.231	-1.939	1.807	0.947
-0.706	0.692	2.225	-2.380	1.448	0.541

7.5 Realization as Dielectric Rings

A particularly simple realization of our model system consists of dielectric rings embedded in a transparent medium, with low refractive-index contrast between the two. Such a structure may be fabricated using direct laser writing (multiphoton lithography), which has been used to fabricate waveguides [206], photonic crystals [33], and many complex high-resolution three-dimensional structures [11] with feature size as small as 40 nm [64, 110]. To cover a large-area surface, one may place many copies of the optimized structure at random positions on the surface to increase the overall response while avoiding inter-structure interference. To verify that all assumptions in our model are valid in such a continuous-ring structure, we use a free-software implementation [173, 172] of the boundary-element method (BEM) to solve the corresponding scattering problem in the original 3D vectorial Maxwell's equations. BEM employs no approximation aside from discretization, so it accounts for effects not considered in our model such as multiple scattering and scattering beyond the dipole approximation. Given the computation cost, we only perform the full-wave BEM calculation on the optimized 10-ring structure, at 50 wavelengths and 50 angles. The z coordinate and major radius of each ring are taken directly from the already-optimized parameters z_j and ρ_j. The weight w_j is the polarizability per scatterer times the number of scatterers in each ring, so it is proportional to the ring volume. Therefore, we choose the thickness of each ring to have its volume proportional to the optimized w_j while keeping the thinnest ring thicker than the 40-nm resolution limit of direct laser writing. We consider dielectric rings with $\epsilon = 1.2$ in air; when the index contrast is low, a different dielectric material changes only the overall scattering strength, and a different medium only scales the overall wavelength. The BEM-calculated differential scattering cross

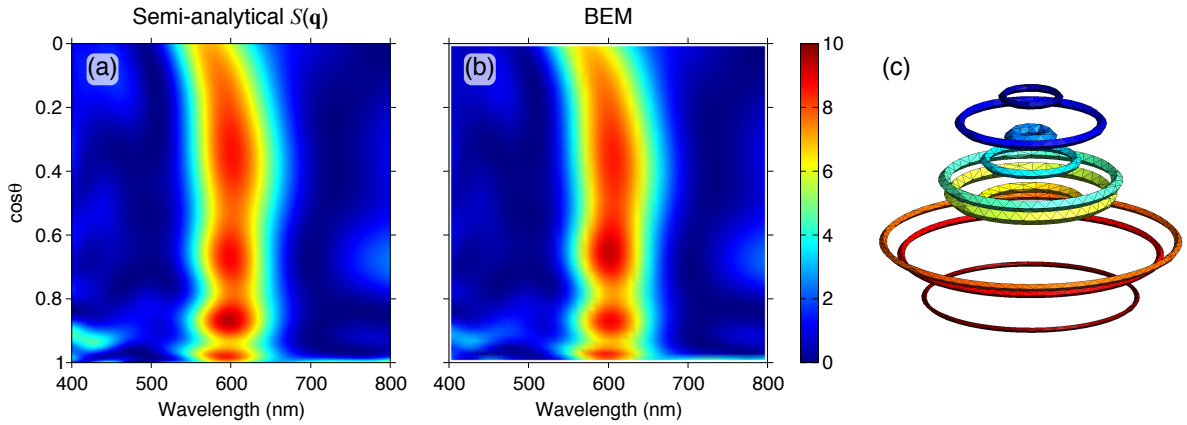

Figure 7.4: Comparison between the semi-analytical model using structure factor [Eqs. (7.1) and (7.5)] and the exact scattering response calculated using the boundary-element method (BEM) for a dielectric-ring structure. (a) Scattering-angle-resolved spectrum of the structure factor $S(\mathbf{q})$ (in arbitrary units) when the optimized 10-ring structure is illuminated along the z direction. (b) Normalized differential scattering cross section, $(d\sigma/d\Omega)/k^4$ (in arbitrary units), calculated using BEM. BEM employs no approximation aside from discretization, so it accounts for multiple scattering and scattering beyond dipole approximation. The incident light is $\mathbf{E}_0 = E_0 e^{ikz}\hat{\mathbf{x}}$, and we calculate light scattered into the y-z plane using Eq. (10.93) in Ref. [79] within the BEM framework. The particular system here consists of dielectric rings ($\epsilon = 1.2$) in air. (c) The surface mesh we use for the BEM calculation, with a total of 3100 triangles. The thickness (minor diameter) of each ring lies in between 42 nm and 122 nm.

section of this structure yields FOM = 2.51 (with $A/B = 3.58$ and $A/C = 8.38$), versus FOM = 2.54 predicted by the semi-analytical $S(\mathbf{q})$. The angle-resolved scattering spectrum from BEM is shown in Figure 7.4(b); it agrees very well with $S(\mathbf{q})$ [shown in Figure 7.4(a)], verifying that our model is appropriate for such low-index-contrast continuous-ring structures and that the optimized result has a certain degree of robustness with respect to how the model is realized. Future work could look for results even more insensitive to errors and implementation details via the "robust optimization" techniques [13, 193, 142, 225, 37, 151, 127, 128].

7.6 Conclusions

The same optimization procedure can be used when a different illumination angle is considered. However, independence of both the incident and the outgoing angles is not possible; $S(\mathbf{q})$ is a function of $\mathbf{q} = k(\hat{\mathbf{n}}_{\text{in}} - \hat{\mathbf{n}}_{\text{out}})$, so independence of both angles would require independence of the wavelength as well, meaning no color. It may be possible, however, to reduce angle dependence or enhance wavelength selectivity by intentionally going beyond dipole scattering and single scattering, or by introducing resonances in the polarizabilities or in the form factors of individual scatterers. Another interesting future direction would be to explore whether there is a fundamental lower limit on the product of the angular and frequency bandwidths per unit volume, analogous to similar limits on the delay–bandwidth product [130].

The wavelength-selective and viewing-angle-independent light scattering here can be useful for the selective-scattering transparent display in Chapter 5. In Chapter 5, the wavelength selectivity was achieved using plasmonic nanoparticles, but that approach is limited by absorption from the metal, which introduces undesirable absorption and resonance broadening; the approach here has no such limitations. Another application of this study is the creation of "structural paints" with accurately defined colors that will never fade. The sharp wavelength response can be modified by the presence of nearby molecules, so our structure may also be used for chemical and biosensing.

Chapter 8

Outlook

In this thesis, we have explored several interesting behaviors of light in resonant nanophotonic structures. Here, we discuss their implications and directions for future works.

8.1 Infinite-lifetime Resonances

The work on optical bound states in the continuum (BICs) described in Chapter 2 through Chapter 4 provides not only understanding of these unusual state but also new opportunities for applications. One application is PhC lasers. High-Q resonances in photonic crystal slabs have been used to enable high-power semiconductor lasers [68], but the emission is traditionally in the normal direction (vertical emission) or the parallel direction (edge emission), except for cases using complicated superlattice engineering [104]. The off-normal BICs we study, on the other hand, can serve as the laser resonance mode and produce laser emission in arbitrary directions. With more design, it may even be possible to enable on-chip beam steering, which can be useful for a wide range of applications from compact laser projectors, laser printers, and DVD drives to 3D laser displays.

Through the annihilation and bouncing of topological charges (described in Chapter 4) and through perturbations that alter the peak Q (*e.g.*, Figure 3.3), it is possible to

design a wide range of dispersion curves for $Q(\mathbf{k}_{\|})$ with prescribed value of peak Q. This can enable Q-matching [25] in arbitrary circumstances (for optimizing radiation efficiency) and also single-mode laser operation over larger-area and high-power [18]. Also, the systems we have studied so far concern a single resonance. When there are multiple resonances with one or more BICs at the same k point, there can be interesting effects through interference similar to what we study with nanoparticles in Chapter 6 and through interaction between resonances; this provides opportunities to engineer special $Q(\mathbf{k}_{\|})$ curves and special band structures. With the BICs, designs such as that described in Ref. [18] with two semi-infinite photonic crystals may be achievable using photonic crystal slabs (Chapter 3) or surface states in a bulk photonic crystal (Chapter 2) without the undesirable top layer.

BIC in photonics crystal slabs can be used for biosensing applications due to its long lifetime and field enhancement, as already demonstrated in Ref. [246]. The "accidental" type of BIC can also be used for sensing in a different way: the presence of biomolecules on the surface can break the mirror symmetry of the structure and lead to radiation that can be detected to monitor the presence of the molecules.

The same type of BIC states can also exist in cylindrical fibers with periodic refractive index variation along the axial direction. This opens up new opportunities in fiber optical communications, fiber lasers, and the study of nonlinearity in fibers.

In Figure 4.2 in Chapter 4, we outline the symmetry requirements for this type of BICs: C_2T and σ_z are necessary for stable BIC at low-symmetry points. The cases this thesis explored have C_2, T and σ_z symmetries all present. It would be interesting to explore situations where T and C_2 symmetries are broken individually while keeping C_2T and σ_z.

Also, in Chapter 4, we explored the topological nature of BIC in photonic crystal

slabs and periodic gratings. This concept seems valid for many other occurrences of BICs, and a generalization to more systems can be a useful extension.

The studies of BIC in this thesis are carried out using a combination of semi-analytical coupled-mode theory, finite-difference time domain (FDTD) simulations [152], and frequency-domain eigenmode solvers [84]. Computation using the mode expansion technique (such as in Ref. [163]) can provide other insights and faster computations.

The same BIC states as studied in this thesis should also exist in single-particle Schrödinger equations and acoustic and water waves; they are also worth investigating.

Another class of BIC not explored in this thesis is those enabled through separability of different degrees of freedom in the system [175, 146, 217, 92, 229]. The simplicity of this type of BIC also makes them attractive to study.

8.2 Resonant Light Scattering

Chapter 5 describes a new type of transparent display, enabled by the wavelength-selective light scattering from nanoparticles. There are a variety of directions that can be explored in future works. One can study the performance of ellipsoidal particles, which are also amenable for wet chemical synthesis and have already proven useful for maximizing extinction per volume [132, 5]. One can also explore magnetic resonances in particles of other shapes, or hot spots in between multiple particles. More generally, a topological optimization can be performed to find the geometry that will yield the best wavelength-selective scattering.

For full-color displays, optimization of transparency and of the color space can be facilitated using the CIE color space framework.

One can also explore dielectric particles. For example, higher-angular-momentum

resonances tend to be sharper. Or, quarter-wave stacks in the radial direction may lead to band gaps and strong scattering in the band-gap frequencies. But, one needs to isolate the desired resonance(s) because typically there are more resonances than desired (*e.g.*, in Figure 6.5).

Disordered structures, which sometimes allow Anderson localization, can be another venue of exploration.

One can also explore resonant scattering from quantum dots, as well as resonant scattering from electronic transitions between different energy levels where the non-radiative decay rate is small (candidates include gases, glass doped with rare-earth atoms, and diamonds with nitrogen-vacancy centers).

Chapter 6 describes resonant scattering from a particle with multiple resonances and the associated scattering dark state. An extension of this work will be to consider perturbations that break the spherical symmetry and therefore couple the different channels, and explore the presence of multiple resonances with multiple radiation channels; this would be an extension of Chapter 6 and Ref. [181].

Another potential exploration topic would be the "coherent perfect absorbers" [27, 224, 148] in the presence of multiple resonances, as an extension to Chapter 6 and Ref. [148].

With careful design of multiple resonances, the nanostructure can potentially be used for nonlinear frequency conversion [176, 17, 20, 63]. Nonlinear frequency conversion in nanoparticles can have a large number of applications from sub-diffraction imaging, neuron voltage sensing, to 3D displays.

An interesting result from Chapter 6 is that BIC can exist in the particle if two resonances are exactly degenerate. Whether two exactly degenerate resonances can be achieved remains unclear, but if it happens, it will relate to our studies in Chapter 2 to

Chapter 4, as well as Refs. [196, 138].

The interference of multiple resonances and the presence of scattering dark states is a general phenomenon that can be explored in systems other than spherical particle light scattering. In fact, the photonic crystal slab structures we study in Chapter 2 to Chapter 4 may also exhibit such phenomenon in appropriate conditions.

In Chapter 7, we design the interference from multiple dipole scatterers to create wavelength-selective scattering that is independent of the viewing angle. One natural extension would be to design structures that have wavelength-selective scattering at three sharp wavelengths corresponding to red, green, and blue; this would be useful for a full-color version of the transparent display application. Designs that reduce fabrication difficulty is another direction.

It may also be possible to reduce angle dependence or enhance wavelength selectivity by intentionally going beyond dipole scattering and single scattering, or by introducing resonances in the polarizabilities or in the form factors of individual scatterers.

Another interesting future direction would be to explore whether there is a fundamental lower limit on the product of the angular and frequency bandwidths per unit volume, analogous to similar limits on the delay–bandwidth product [130].

References

[1] R. Adato, A. Artar, S. Erramilli, and H. Altug. Engineered absorption enhancement and induced transparency in coupled molecular and plasmonic resonator systems. *Nano Lett.*, 13:2584–2591, 2013. doi: 10.1021/nl400689q. (cit. on pp. 76, 77, and 84)

[2] Y. Akahane, T. Asano, B.-S. Song, and S. Noda. High-Q photonic nanocavity in a two-dimensional photonic crystal. *Nature*, 425:944–947, 2003. doi: 10.1038/nature02063. (cit. on p. 17)

[3] R. Ameling, L. Langguth, M. Hentschel, M. Mesch, P. V. Braun, and H. Giessen. Cavity-enhanced localized plasmon resonance sensing. *Appl. Phys. Lett.*, 97: 253116, 2010. doi: 10.1063/1.3530795. (cit. on p. 16)

[4] J. Andkjær, V. E. Johansen, K. S. Friis, and O. Sigmund. Inverse design of nanostructured surfaces for color effects. *J. Opt. Soc. Am. B*, 31:164–174, 2014. doi: 10.1364/JOSAB.31.000164. (cit. on pp. 94 and 95)

[5] E. Anquillare and *et. al.* Broadband optical extinction via aspect-ratio tailored silver nanoplates. 2014. In preparation. (cit. on pp. 6 and 109)

[6] A. C. Arsenault, D. P. Puzzo, I. Manners, and G. A. Ozin. Photonic-crystal full-colour displays. *Nature Photon.*, 1:468–472, 2007. doi: 10.1038/nphoton.2007.140. (cit. on p. 94)

[7] A. Artar, A. A. Yanik, and H. Altug. Multispectral plasmon induced transparency in coupled meta-atoms. *Nano Lett.*, 11:1685–1689, 2011. doi: 10.1021/nl200197j. (cit. on pp. 76 and 77)

[8] A. Artar, A. A. Yanik, and H. Altug. Directional double Fano resonances in plasmonic hetero-oligomers. *Nano Lett.*, 11:3694–3700, 2011. doi: 10.1021/nl201677h. (cit. on pp. 76 and 77)

[9] H. A. Atwater and A. Polman. Plasmonics for improved photovoltaic devices. *Nature Mater.*, 9:205–213, 2010. doi: 10.1038/nmat2629. (cit. on p. 63)

[10] R. Bardhan, S. Mukherjee, N. A. Mirin, S. D. Levit, P. Nordlander, and N. J. Halas. Nanosphere-in-a-nanoshell: A simple nanomatryushka. *J. Phys. Chem. C*, 114:7378–7383, 2010. doi: 10.1021/jp9095387. (cit. on p. 90)

[11] J. Bauer, S. Hengsbach, I. Tesari, R. Schwaiger, and O. Kraft. High-strength cellular ceramic composites with 3D microarchitecture. *Proc. Natl. Acad. Sci. U.S.A.*, 111:2453–2458, 2014. doi: 10.1073/pnas.1315147111. (cit. on pp. 95 and 104)

[12] M. Berry. The adiabatic phase and Pancharatnam's phase for polarized light. *J. Mod. Opt.*, 34:1401–1407, 1987. doi: 10.1080/09500348714551321. (cit. on p. 47)

[13] D. Bertsimas, O. Nohadani, and K. M. Teo. Robust optimization in electromagnetic scattering problems. *J. Appl. Phys.*, 101:074507, 2007. doi: 10.1063/1.2715540. (cit. on p. 105)

[14] J. Bezanson, S. Karpinski, V. B. Shah, and A. Edelman. Julia: A fast dynamic language for technical computing. 2012. arXiv: 1209.5145. (cit. on p. 100)

[15] C. F. Bohren and D. R. Huffman. *Absorption and Scattering of Light by Small Particles*. Wiley, New York, 1998. doi: 10.1002/9783527618156. (cit. on pp. 64, 73, 76, 78, 82, and 83)

[16] L. D. Bonifacio, B. V. Lotsch, D. P. Puzzo, F. Scotognella, and G. A. Ozin. Stacking the nanochemistry deck: Structural and compositional diversity in one-dimensional photonic crystals. *Adv. Mater.*, 21:1641–1646, 2009. doi: 10.1002/adma.200802348. (cit. on pp. 94 and 95)

[17] J. Bravo-Abad, A. Rodriguez, P. Bermel, S. G. Johnson, J. D. Joannopoulos, and M. Soljačić. Enhanced nonlinear optics in photonic-crystal microcavities. *Opt. Express*, 15:16161–16176, 2007. doi: 10.1364/OE.15.016161. (cit. on p. 110)

[18] J. Bravo-Abad, J. D. Joannopoulos, and M. Soljačić. Enabling single-mode behavior over large areas with photonic Dirac cones. *Proc. Natl. Acad. Sci. U.S.A.*, 109:9761–9765, 2012. doi: 10.1073/pnas.1207335109. (cit. on pp. 22 and 108)

[19] E. N. Bulgakov and A. F. Sadreev. Bound states in the continuum in photonic waveguides inspired by defects. *Phys. Rev. B*, 78:075105, 2008. doi: 10.1103/PhysRevB.78.075105. (cit. on p. 39)

[20] I. B. Burgess, A. W. Rodriguez, M. W. McCutcheon, J. Bravo-Abad, Y. Zhang, S. G. Johnson, and M. Lončar. Difference-frequency generation with quantum-limited efficiency in triply-resonant nonlinear cavities. *Opt. Express*, 17:9241–9251, 2009. doi: 10.1364/OE.17.009241. (cit. on p. 110)

[21] L. Cao, P. Fan, E. S. Barnard, A. M. Brown, and M. L. Brongersma. Spectral reflectance and directional properties of structural coloration in bird plumage. *J. Exp. Biol.*, 205:2017–2027, 2002. (cit. on pp. 94, 95, and 97)

[22] L. Cao, P. Fan, E. S. Barnard, A. M. Brown, and M. L. Brongersma. Tuning the color of silicon nanostructures. *Nano. Lett.*, 10:2649–2654, 2010. doi: 10.1021/nl1013794. (cit. on pp. 94 and 95)

[23] L. Cao, P. Fan, and M. L. Brongersma. Optical coupling of deep-subwavelength semiconductor nanowires. *Nano Lett.*, 11:1463–1468, 2011. doi: 10.1021/nl1040429. (cit. on p. 76)

[24] F. Capasso, C. Sirtori, J. Faist, D. L. Sivco, S.-N. G. Chu, and A. Y. Cho. Observation of an electronic bound state above a potential well. *Nature*, 358:565–567, 1992. doi: 10.1038/358565a0. (cit. on p. 9)

[25] D. L. C. Chan, I. Celanovic, J. D. Joannopoulos, and M. Soljačić. Emulating one-dimensional resonant Q-matching behavior in a two-dimensional system via Fano resonances. *Phys. Rev. A*, 74:064901, 2006. doi: 10.1103/PhysRevA.74.064901. (cit. on p. 108)

[26] B.-H. Cheong, O. N. Prudnikov, E. Cho, H.-S. Kim, J. Yu, Y.-S. Cho, H.-Y. Choi, and S. T. Shin. High angular tolerant color filter using subwavelength grating. *Appl. Phys. Lett.*, 94:213104, 2009. doi: 10.1063/1.3139058. (cit. on pp. 94 and 95)

[27] Y. D. Chong and A. D. Stone. Hidden black: Coherent enhancement of absorption in strongly scattering media. *Phys. Rev. Lett.*, 107:163901, 2011. doi: 10.1103/PhysRevLett.107.163901. (cit. on p. 110)

[28] S.-L. Chua, Y. Chong, A. D. Stone, M. Soljačić, and J. Bravo-Abad. Low-threshold lasing action in photonic crystal slabs enabled by Fano resonances. *Opt. Express*, 19:1539–1562, 2011. doi: 10.1364/OE.19.001539. (cit. on p. 22)

[29] G. Corrielli, G. Della Valle, A. Crespi, R. Osellame, and S. Longhi. Observation of surface states with algebraic localization. *Phys. Rev. Lett.*, 111:220403, 2013. doi: 10.1103/PhysRevLett.111.220403. (cit. on p. 39)

[30] T. J. Davis, D. E. Gómez, and K. C. Vernon. Simple model for the hybridization of surface plasmon resonances in metallic nanoparticles. *Nano Lett.*, 10:2618–2625, 2010. doi: 10.1021/nl101335z. (cit. on pp. 76 and 77)

[31] B. G. DeLacy, W. Qiu, M. Soljačić, C. W. Hsu, O. D. Miller, S. G. Johnson, and J. D. Joannopoulos. Layer-by-layer self-assembly of plexcitonic nanoparticles. *Opt. Express*, 21:19103–19112, 2013. doi: 10.1364/OE.21.019103. (cit. on p. 6)

[32] B. G. DeLacy, O. D. Miller, C. W. Hsu, Z. Zander, S. Lacey, R. Yagloski, A. W. Fountain, E. Valdes, E. Anquillare, M. Soljačić, S. G. Johnson, and J. D. Joannopoulos. Coherent plasmon-exciton coupling in silver platelet-J-aggregate nanocomposites. 2014. In preparation. (cit. on p. 6)

[33] M. Deubel, G. Von Freymann, M. Wegener, S. Pereira, K. Busch, and C. M. Soukoulis. Direct laser writing of three-dimensional photonic-crystal templates for telecommunications. *Nature Mater.*, 3:444–447, 2004. doi: 10.1038/nmat1155. (cit. on pp. 95 and 104)

[34] R. J. Donnelly. *Quantized vortices in helium II*, volume 2. Cambridge University Press, 1991. (cit. on pp. 47 and 60)

[35] E. Downing, L. Hesselink, J. Ralston, and R. Macfarlane. A three-color, solid-state, three-dimensional display. *Science*, 273:1185–1189, 1996. doi: 10.1126/science.273.5279.1185. (cit. on p. 62)

[36] E. R. Dufresne, H. Noh, V. Saranathan, S. G. J. Mochrie, H. Cao, and R. O. Prum. Self-assembly of amorphous biophotonic nanostructures by phase separation. *Soft Matter*, 5:1792–1795, 2009. doi: 10.1039/B902775K. (cit. on pp. 94 and 95)

[37] Y. Elesin, B. Lazarov, J. Jensen, and O. Sigmund. Design of robust and efficient photonic switches using topology optimization. *Photon. Nanostruct.*, 10:153 – 165, 2012. doi: 10.1016/j.photonics.2011.10.003. (cit. on p. 105)

[38] D. V. Evans, C. M. Linton, and F. Ursell. Trapped mode frequencies embedded in the continuous spectrum. *Q. J. Mech. Appl. Math.*, 46:253–274, 1993. doi: 10.1093/qjmam/46.2.253. (cit. on pp. 8 and 9)

[39] D. V. Evans, M. Levitin, and D. Vassiliev. Existence theorems for trapped modes. *J. Fluid Mech.*, 261:21–31, 1994. doi: 10.1017/S0022112094000236. (cit. on pp. 8, 9, 39, and 60)

[40] J. A. Fan, C. Wu, K. Bao, J. Bao, R. Bardhan, N. J. Halas, V. N. Manoharan, P. Nordlander, G. Shvets, and F. Capasso. Self-assembled plasmonic nanoparticle clusters. *Science*, 328:1135–1138, 2010. doi: 10.1126/science.1187949. (cit. on p. 63)

[41] S. Fan and J. D. Joannopoulos. Analysis of guided resonances in photonic crystal slabs. *Phys. Rev. B*, 65:235112, 2002. doi: 10.1103/PhysRevB.65.235112. (cit. on pp. 8, 9, 22, 32, 35, and 40)

[42] S. Fan, W. Suh, and J. D. Joannopoulos. Temporal coupled-mode theory for the Fano resonance in optical resonators. *J. Opt. Soc. Am. A*, 20:569–572, 2003. doi: 10.1364/JOSAA.20.000569. (cit. on pp. 13, 14, and 35)

[43] U. Fano. Effects of configuration interaction on intensities and phase shifts. *Phys. Rev.*, 124:1866–1878, 1961. doi: 10.1103/PhysRev.124.1866. (cit. on pp. 77 and 87)

[44] V. A. Fedotov, M. Rose, S. L. Prosvirnin, N. Papasimakis, and N. I. Zheludev. Sharp trapped-mode resonances in planar metamaterials with a broken structural symmetry. *Phys. Rev. Lett.*, 99:147401, 2007. doi: 10.1103/PhysRevLett.99.147401. (cit. on p. 77)

[45] N. T. Fofang, T.-H. Park, O. Neumann, N. A. Mirin, P. Nordlander, and N. J. Halas. Plexcitonic nanoparticles: Plasmon-exciton coupling in nanoshell-J-aggregate complexes. *Nano Lett.*, 8:3481–3487, 2008. doi: 10.1021/nl8024278. (cit. on p. 76)

[46] C. Forestiere, L. Dal Negro, and G. Miano. Theory of coupled plasmon modes and Fano-like resonances in subwavelength metal structures. *Phys. Rev. B*, 88: 155411, 2013. doi: 10.1103/PhysRevB.88.155411. (cit. on pp. 76 and 77)

[47] J. D. Forster, H. Noh, S. F. Liew, V. Saranathan, C. F. Schreck, L. Yang, J.-G. Park, R. O. Prum, S. G. J. Mochrie, C. S. O'Hern, H. Cao, and E. R. Dufresne. Biomimetic isotropic nanostructures for structural coloration. *Adv. Mater.*, 22: 2939–2944, 2010. doi: 10.1002/adma.200903693. (cit. on pp. 94 and 95)

[48] M. Freeman, M. Champion, and S. Madhavan. Scanned laser pico-projectors: Seeing the big picture (with a small device). *Opt. Photonics News*, 20:28–34, 2009. doi: 10.1364/OPN.20.5.000028. (cit. on p. 73)

[49] H. Friedrich and D. Wintgen. Interfering resonances and bound states in the continuum. *Phys. Rev. A*, 32:3231–3242, 1985. doi: 10.1103/PhysRevA.32.3231. (cit. on pp. 8, 9, 23, 24, 38, and 39)

[50] B. Gallinet and O. J. F. Martin. Influence of electromagnetic interactions on the line shape of plasmonic Fano resonances. *ACS Nano*, 5:8999–9008, 2011. doi: 10.1021/nn203173r. (cit. on pp. 76 and 77)

[51] B. Gallinet and O. J. F. Martin. *Ab initio* theory of Fano resonances in plasmonic nanostructures and metamaterials. *Phys. Rev. B*, 83:235427, 2011. doi: 10.1103/PhysRevB.83.235427. (cit. on pp. 76 and 77)

[52] N. Ganesh, W. Zhang, P. C. Mathias, E. Chow, S. A. N. T., V. Malyarchuk, A. D. Smith, and B. T. Cunningham. Enhanced fluorescence emission from quantum dots on a photonic crystal surface. *Nature Nanotech.*, 2:515–520, 2007. doi: 10.1038/nnano.2007.216. (cit. on p. 40)

[53] C. L. Garrido Alzar, M. A. G. Martinez, and P. Nussenzveig. Classical analog of electromagnetically induced transparency. *Am. J. Phys.*, 70:37–41, 2002. doi: 10.1119/1.1412644. (cit. on p. 77)

[54] V. Giannini, Y. Francescato, H. Amrania, C. C. Phillips, and S. A. Maier. Fano resonances in nanoscale plasmonic systems: A parameter-free modeling approach. *Nano Lett.*, 11:2835–2840, 2011. doi: 10.1021/nl201207n. (cit. on pp. 76 and 77)

[55] J. F. Goldenberg and T. S. McKechnie. Diffraction analysis of bulk diffusers for projection-screen applications. *J. Opt. Soc. Am. A*, 2:2337–2347, 1985. doi: 10.1364/JOSAA.2.002337. (cit. on p. 61)

[56] P. Görrn, M. Sander, J. Meyer, M. Kröger, E. Becker, H.-H. Johannes, W. Kowalsky, and T. Riedl. Towards see-through displays: Fully transparent thin-film transistors driving transparent organic light-emitting diodes. *Adv. Mater.*, 18: 738–741, 2006. doi: 10.1002/adma.200501957. (cit. on p. 62)

[57] D. J. Griffiths. *Introduction to Quantum Mechanics*. Pearson Prentice Hall, Englewood Cliffs, NJ, 2 edition, 2004. (cit. on p. 3)

[58] M. D. Groves. Examples of embedded eigenvalues for problems in acoustic waveguides. *Math. Method. Appl. Sci.*, 21:479–488, 1998. doi: 10.1002/(SICI)1099-1476(199804)21:6<479::AID-MMA950>3.0.CO;2-V. (cit. on pp. 8 and 9)

[59] N. J. Halas, S. Lal, W.-S. Chang, S. Link, and P. Nordlander. Plasmons in strongly coupled metallic nanostructures. *Chem. Rev.*, 111:3913–3961, 2011. doi: 10.1021/cr200061k. (cit. on p. 76)

[60] R. E. Hamam, A. Karalis, J. D. Joannopoulos, and M. Soljačić. Coupled-mode theory for general free-space resonant scattering of waves. *Phys. Rev. A*, 75: 053801, 2007. doi: 10.1103/PhysRevA.75.053801. (cit. on pp. 68, 76, 79, and 81)

[61] S. E. Harris. Electromagnetically induced transparency. *Phys. Today*, 50:36, 1997. doi: 10.1063/1.881806. (cit. on p. 89)

[62] M. Harun-Ur-Rashid, A. Bin Imran, T. Seki, M. Ishii, H. Nakamura, and Y. Takeoka. Angle-independent structural color in colloidal amorphous arrays. *ChemPhysChem*, 11:579–583, 2010. doi: 10.1002/cphc.200900869. (cit. on pp. 94 and 95)

[63] H. Hashemi, A. W. Rodriguez, J. D. Joannopoulos, M. Soljačić, and S. G. Johnson. Nonlinear harmonic generation and devices in doubly resonant Kerr cavities. *Phys. Rev. A*, 79:013812, 2009. doi: 10.1103/PhysRevA.79.013812. (cit. on p. 110)

[64] W. Haske, V. W. Chen, J. M. Hales, W. Dong, S. Barlow, S. R. Marder, and J. W. Perry. 65 nm feature sizes using visible wavelength 3-d multiphoton lithography. *Opt. Express*, 15:3426–3436, 2007. doi: 10.1364/OE.15.003426. (cit. on pp. 95 and 104)

[65] L. V. Hau, S. E. Harris, Z. Dutton, and C. H. Behroozi. Light speed reduction to 17 metres per second in an ultracold atomic gas. *Nature*, 397:594–598, 1999. doi: 10.1038/17561. (cit. on p. 89)

[66] H. A. Haus. *Waves and Fields in Optoelectronics*. Prentice-Hall, Englewood Cliffs, NJ, 1984. (cit. on pp. 13, 32, 35, and 81)

[67] O. Hess, J. B. Pendry, S. A. Maier, R. F. Oulton, J. M. Hamm, and K. L. Tsakmakidis. Active nanoplasmonic metamaterials. *Nature Mater.*, 11:573–584, 2012. doi: 10.1038/nmat3356. (cit. on p. 22)

[68] K. Hirose, Y. Liang, Y. Kurosaka, A. Watanabe, T. Sugiyama, and S. Noda. Watt-class high-power, high-beam-quality photonic-crystal lasers. *Nature Photon.*, 8: 406–411, 2014. doi: 10.1038/nphoton.2014.75. (cit. on pp. 40 and 107)

[69] P. D. Hislop and I. M. Sigal. *Introduction to Spectral Theory: with Applications to Schrödinger Operators*. Springer Verlag, New York, 1996. (cit. on pp. 8, 23, and 25)

[70] J. F. Ho, B. Luk'yanchuk, and J. B. Zhang. Tunable Fano resonances in silver-silica-silver multilayer nanoshells. *Appl. Phys. A: Mater. Sci. Process.*, 107:133–137, 2012. doi: 10.1007/s00339-012-6757-1. (cit. on p. 90)

[71] C. W. Hsu, B. Zhen, S.-L. Chua, S. G. Johnson, J. D. Joannopoulos, and M. Soljačić. Bloch surface eigenstates within the radiation continuum. *Light: Science & Applications*, 2:e84, 2013. doi: 10.1038/lsa.2013.40. (cit. on pp. 6, 23, 24, 35, 38, 39, 45, and 60)

[72] C. W. Hsu, B. Zhen, J. Lee, S.-L. Chua, S. G. Johnson, J. D. Joannopoulos, and M. Soljačić. Observation of trapped light within the radiation continuum. *Nature*, 499:188–191, 2013. doi: 10.1038/nature12289. (cit. on pp. 6, 39, 40, 48, and 60)

[73] C. W. Hsu, B. G. DeLacy, S. G. Johnson, J. D. Joannopoulos, and M. Soljačić. Theoretical criteria for scattering dark states in nanostructured particles. *Nano Lett.*, 14:2783–2788, 2014. doi: 10.1021/nl500340n. (cit. on pp. 6 and 95)

[74] C. W. Hsu, O. D. Miller, S. G. Johnson, and M. Soljačić. Optimization of sharp and viewing-angle-independent structural color. 2014. arXiv: 1410.8605. (cit. on p. 6)

[75] C. W. Hsu, B. Zhen, W. Qiu, O. Shapira, B. G. DeLacy, J. D. Joannopoulos, and M. Soljačić. Transparent displays enabled by resonant nanoparticle scattering. *Nat. Commun.*, 5:3152, 2014. doi: 10.1038/ncomms4152. (cit. on pp. 6, 90, and 95)

[76] E. Hutter and J. H. Fendler. Exploitation of localized surface plasmon resonance. *Adv. Mater.*, 16:1685–1706, 2004. doi: 10.1002/adma.200400271. (cit. on p. 63)

[77] K. Ishizaki and S. Noda. Manipulation of photons at the surface of three-dimensional photonic crystals. *Nature*, 460:367–370, 2009. doi: 10.1038/nature08190. (cit. on p. 7)

[78] S. Iwahashi, Y. Kurosaka, K. Sakai, K. Kitamura, N. Takayama, and S. Noda. Higher-order vector beams produced by photonic-crystal lasers. *Opt. Express*, 19: 11963–11968, 2011. doi: 10.1364/OE.19.011963. (cit. on p. 60)

[79] J. D. Jackson. *Classical Electrodynamics*. Wiley, New York, 3 edition, 1998. (cit. on pp. 96, 97, and 105)

[80] J. D. Joannopoulos, S. G. Johnson, J. N. Winn, and R. D. Meade. *Photonic Crystals: Molding the Flow of Light*. Princeton University Press, Princeton, NJ, 2 edition, 2008. (cit. on pp. 7, 9, 13, 15, 23, 25, 27, 32, 35, 40, 41, 44, and 95)

[81] Y. S. Joe, A. M. Satanin, and C. S. Kim. Classical analogy of Fano resonances. *Phys. Scr.*, 74:259, 2006. doi: 10.1088/0031-8949/74/2/020. (cit. on p. 77)

[82] V. E. Johansen, J. Andkjær, and O. Sigmund. Design of structurally colored surfaces based on scalar diffraction theory. *J. Opt. Soc. Am. B*, 31:207–217, 2014. doi: 10.1364/JOSAB.31.000207. (cit. on pp. 94 and 95)

[83] S. G. Johnson. The NLopt nonlinear-optimization package, http://ab-initio.mit.edu/nlopt. (cit. on pp. 67 and 100)

[84] S. G. Johnson and J. D. Joannopoulos. Block-iterative frequency-domain methods for Maxwell's equations in a planewave basis. *Opt. Express*, 8:173–190, 2001. doi: 10.1364/OE.8.000173. (cit. on pp. 27, 29, and 109)

[85] S. G. Johnson, S. Fan, A. Mekis, and J. D. Joannopoulos. Multipole-cancellation mechanism for high-Q cavities in the absence of a complete photonic band gap. *Appl. Phys. Lett.*, 78:3388–3390, 2001. doi: 10.1063/1.1375838. (cit. on p. 17)

[86] D. S. Jones. The eigenvalues of $\nabla^2 u + \lambda u = 0$ when the boundary conditions are given on semi-infinite domains. *Math. Proc. Cambridge*, 49:668–684, 1953. doi: 10.1017/S0305004100028875. (cit. on pp. 8 and 9)

[87] S. Ju, J. Li, J. Liu, P.-C. Chen, Y.-g. Ha, F. Ishikawa, H. Chang, C. Zhou, A. Facchetti, D. B. Janes, and T. J. Marks. Transparent active matrix organic light-emitting diode displays driven by nanowire transistor circuitry. *Nano Lett.*, 8:997–1004, 2008. doi: 10.1021/nl072538+. (cit. on p. 62)

[88] P. Kaelo and M. Ali. Some variants of the controlled random search algorithm for global optimization. *J. Optimiz. Theory App.*, 130:253–264, 2006. doi: 10.1007/s10957-006-9101-0. (cit. on p. 100)

[89] I. Kaminer, R. Bekenstein, J. Nemirovsky, and M. Segev. Nondiffracting accelerating wave packets of Maxwell's equations. *Phys. Rev. Lett.*, 108:163901, 2012. doi: 10.1103/PhysRevLett.108.163901. (cit. on p. 1)

[90] A. Karalis, S. G. Johnson, and J. D. Joannopoulos. Discrete-mode cancellation mechanism for high-Q integrated optical cavities with small modal volume. *Opt. Lett.*, 29:2309–2311, 2004. doi: 10.1364/OL.29.002309. (cit. on p. 17)

[91] M. A. Kats, R. Blanchard, P. Genevet, and F. Capasso. Nanometre optical coatings based on strong interference effects in highly absorbing media. *Nature Mater.*, 12:20–24, 2013. doi: 10.1038/nmat3443. (cit. on pp. 94 and 95)

[92] S. Kawakami. Analytically solvable model of photonic crystal structures and novel phenomena. *J. Lightwave Technol.*, 20:1644, 2002. doi: 10.1109/JLT.2002.800267. (cit. on pp. 8, 9, and 109)

[93] K. L. Kelly, E. Coronado, L. L. Zhao, and G. C. Schatz. The optical properties of metal nanoparticles: The influence of size, shape, and dielectric environment. *J. Phys. Chem. B*, 107:668–677, 2003. doi: 10.1021/jp026731y. (cit. on p. 63)

[94] A. B. Khanikaev, C. Wu, and G. Shvets. Fano-resonant metamaterials and their applications. *Nanophotonics*, 2:247–264, 2013. doi: 10.1515/nanoph-2013-0009. (cit. on pp. 76 and 77)

[95] H. Kim, J. Ge, J. Kim, S.-e. Choi, H. Lee, H. Lee, W. Park, Y. Yin, and S. Kwon. Structural colour printing using a magnetically tunable and lithographically fixable photonic crystal. *Nature Photon.*, 3:534–540, 2009. doi: 10.1038/nphoton.2009.141. (cit. on p. 94)

[96] S.-K. Kim, R. W. Day, J. F. Cahoon, T. J. Kempa, K.-D. Song, H.-G. Park, and C. M. Lieber. Tuning light absorption in core/shell silicon nanowire photovoltaic devices through morphological design. *Nano Lett.*, 12:4971–4976, 2012. doi: 10.1021/nl302578z. (cit. on p. 76)

[97] S. Kinoshita, S. Yoshioka, and J. Miyazaki. Physics of structural colors. *Rep. Prog. Phys.*, 71:076401, 2008. doi: 10.1088/0034-4885/71/7/076401. (cit. on p. 94)

[98] K. Kitamura, K. Sakai, N. Takayama, M. Nishimoto, and S. Noda. Focusing properties of vector vortex beams emitted by photonic-crystal lasers. *Opt. Lett.*, 37:2421–2423, 2012. doi: 10.1364/OL.37.002421. (cit. on p. 60)

[99] D.-H. Ko, J. R. Tumbleston, L. Zhang, S. Williams, J. M. DeSimone, R. Lopez, and E. T. Samulski. Photonic crystal geometry for organic solar cells. *Nano Lett.*, 9:2742–2746, 2009. doi: 10.1021/nl901232p. (cit. on p. 40)

[100] N. Kometani, M. Tsubonishi, T. Fujita, K. Asami, and Y. Yonezawa. Preparation and optical absorption spectra of dye-coated Au, Ag, and Au/Ag colloidal nanoparticles in aqueous solutions and in alternate assemblies. *Langmuir*, 17: 578–580, 2001. doi: 10.1021/la0013190. (cit. on p. 76)

[101] P. Kramper, M. Agio, C. M. Soukoulis, A. Birner, F. Müller, R. B. Wehrspohn, U. Gösele, and V. Sandoghdar. Highly directional emission from photonic crystal waveguides of subwavelength width. *Phys. Rev. Lett.*, 92:113903, 2004. doi: 10.1103/PhysRevLett.92.113903. (cit. on p. 7)

[102] H. Krüger. On the existence of embedded eigenvalues. *J. Math. Anal. Appl.*, 395: 776, 2012. doi: 10.1016/j.jmaa.2012.05.075. (cit. on pp. 8, 9, 23, 24, and 38)

[103] S. Kucherenko and Y. Sytsko. Application of deterministic low-discrepancy sequences in global optimization. *Comput. Optim. Appl.*, 30:297–318, 2005. doi: 10.1007/s10589-005-4615-1. (cit. on p. 67)

[104] Y. Kurosaka, S. Iwahashi, Y. Liang, K. Sakai, E. Miyai, W. Kunishi, D. Ohnishi, and S. Noda. On-chip beam-steering photonic-crystal lasers. *Nature Photon.*, 4: 447–450, 2010. doi: 10.1038/nphoton.2010.118. (cit. on pp. 60 and 107)

[105] A. Lagendijk, B. van Tiggelen, and D. S. Wiersma. Fifty years of anderson localization. *Phys. Today*, 62:24–29, 2009. doi: 10.1063/1.3206091. (cit. on p. 23)

[106] S. Lal, S. Link, and N. J. Halas. Nano-optics from sensing to waveguiding. *Nature Photon.*, 1:641–648, 2007. doi: 10.1038/nphoton.2007.223. (cit. on p. 63)

[107] J. B. Lassiter, H. Sobhani, M. W. Knight, W. S. Mielczarek, P. Nordlander, and N. J. Halas. Designing and deconstructing the Fano lineshape in plasmonic nanoclusters. *Nano Lett.*, 12:1058–1062, 2012. doi: 10.1021/nl204303d. (cit. on pp. 76, 77, and 84)

[108] J. Lee, B. Zhen, S.-L. Chua, W. Qiu, J. D. Joannopoulos, M. Soljačić, and O. Shapira. Observation and differentiation of unique high-Q optical resonances near zero wave vector in macroscopic photonic crystal slabs. *Phys. Rev. Lett.*, 109: 067401, 2012. doi: 10.1103/PhysRevLett.109.067401. (cit. on pp. 8, 9, 22, 23, 24, 25, 28, 39, 40, and 60)

[109] J. Lee, B. Zhen, S.-L. Chua, O. Shapira, and M. Soljačić. Fabricating centimeter-scale high quality factor two-dimensional periodic photonic crystal slabs. *Opt. Express*, 22:3724–3731, 2014. doi: 10.1364/OE.22.003724. (cit. on p. 31)

[110] L. Li, R. R. Gattass, E. Gershgoren, H. Hwang, and J. T. Fourkas. Achieving $\lambda/20$ resolution by one-color initiation and deactivation of polymerization. *Science*, 324: 910–913, 2009. doi: 10.1126/science.1168996. (cit. on pp. 95 and 104)

[111] C. M. Linton and P. McIver. Embedded trapped modes in water waves and acoustics. *Wave Motion*, 45:16, 2007. doi: 10.1016/j.wavemoti.2007.04.009. (cit. on pp. 8, 9, 23, 24, and 38)

[112] J. Liu and X.-D. Sun. System and method for a transparent color image display utilizing fluorescence conversion of nano particles and molecules, 2006. US Patent 7090355 filed 18 May 2004, and issued 15 Aug 2006. (cit. on p. 61)

[113] N. Liu, L. Langguth, T. Weiss, J. Kästel, M. Fleischhauer, T. Pfau, and H. Giessen. Plasmonic analogue of electromagnetically induced transparency at the Drude damping limit. *Nature Mater.*, 8:758–762, 2009. doi: 10.1038/nmat2495. (cit. on pp. 77, 84, and 89)

[114] V. Liu and S. Fan. S^4 : A free electromagnetic solver for layered periodic structures. *Comput. Phys. Commun.*, 183:2233 – 2244, 2012. doi: 10.1016/j.cpc.2012.04.026. (cit. on p. 33)

[115] V. Liu, M. Povinelli, and S. Fan. Resonance-enhanced optical forces between coupled photonic crystal slabs. *Opt. Express*, 17:21897–21909, 2009. doi: 10.1364/OE.17.021897. (cit. on pp. 39 and 60)

[116] M. Lončar, A. Scherer, and Y. Qiu. Photonic crystal laser sources for chemical detection. *Appl. Phys. Lett.*, 82:4648–4650, 2003. doi: 10.1063/1.1586781. (cit. on p. 22)

[117] A. Lovera, B. Gallinet, P. Nordlander, and O. J. Martin. Mechanisms of Fano resonances in coupled plasmonic systems. *ACS Nano*, 7:4527–4536, 2013. doi: 10.1021/nn401175j. (cit. on pp. 76 and 77)

[118] B. Luk'yanchuk, N. I. Zheludev, S. A. Maier, N. J. Halas, P. Nordlander, H. Giessen, and C. T. Chong. The Fano resonance in plasmonic nanostructures and metamaterials. *Nature Mater.*, 9:707–715, 2010. doi: 10.1038/nmat2810. (cit. on pp. 76, 77, and 79)

[119] S. Magkiriadou, J.-G. Park, Y.-S. Kim, and V. N. Manoharan. Disordered packings of core-shell particles with angle-independent structural colors. *Opt. Mater. Express*, 2:1343–1352, 2012. doi: 10.1364/OME.2.001343. (cit. on pp. 94 and 95)

[120] S. Magkiriadou, J.-G. Park, Y.-S. Kim, and V. N. Manoharan. On the absence of red structural color in photonic glasses, bird feathers and certain beetles. 2014. arXiv: 1409.8575. (cit. on pp. 94 and 95)

[121] L. Maleki, A. B. Matsko, A. A. Savchenkov, and V. S. Ilchenko. Tunable delay line with interacting whispering-gallery-moderesonators. *Opt. Lett.*, 29:626–628, 2004. doi: 10.1364/OL.29.000626. (cit. on p. 77)

[122] J. L. Mañes, F. Guinea, and M. A. Vozmediano. Existence and topological stability of Fermi points in multilayered graphene. *Phys. Rev. B*, 75:155424, 2007. doi: 10.1103/PhysRevB.75.155424. (cit. on pp. 47 and 60)

[123] A. Manjavacas, F. J. G. d. Abajo, and P. Nordlander. Quantum plexcitonics: Strongly interacting plasmons and excitons. *Nano Lett.*, 11:2318–2323, 2011. doi: 10.1021/nl200579f. (cit. on p. 76)

[124] D. C. Marinica, A. G. Borisov, and S. V. Shabanov. Bound states in the continuum in photonics. *Phys. Rev. Lett.*, 100:183902, 2008. doi: 10.1103/PhysRevLett.100.183902. (cit. on pp. 8, 9, 17, 18, 23, 24, 38, 39, and 60)

[125] J. C. Maxwell. A dynamical theory of the electromagnetic field. *Philosophical Transactions of the Royal Society of London*, 155:459–512, 1865. Abstract: Proceedings of the Royal Society of London **13**, 531-536 (1864). (cit. on p. 1)

[126] R. D. Meade, K. D. Brommer, A. M. Rappe, and J. D. Joannopoulos. Electromagnetic Bloch waves at the surface of a photonic crystal. *Phys. Rev. B*, 44: 10961–10964, 1991. doi: 10.1103/PhysRevB.44.10961. (cit. on p. 7)

[127] H. Men, R. M. Freund, N. C. Nguyen, J. Saa-Seoane, and J. Peraire. Fabrication-adaptive optimization with an application to photonic crystal design. *Oper. Res.*, 62:418–434, 2014. doi: 10.1287/opre.2013.1252. (cit. on p. 105)

[128] H. Men, K. Y. K. Lee, R. M. Freund, J. Peraire, and S. G. Johnson. Robust topology optimization of three-dimensional photonic-crystal band-gap structures. *Opt. Express*, 22:22632–22648, 2014. doi: 10.1364/OE.22.022632. (cit. on p. 105)

[129] N. D. Mermin. The topological theory of defects in ordered media. *Rev. Mod. Phys.*, 51:591, 1979. doi: 10.1103/RevModPhys.51.591. (cit. on pp. 47, 48, and 60)

[130] D. A. B. Miller. Fundamental limit to linear one-dimensional slow light structures. *Phys. Rev. Lett.*, 99:203903, 2007. doi: 10.1103/PhysRevLett.99.203903. (cit. on pp. 106 and 111)

[131] O. D. Miller. *Photonic Design: From Fundamental Solar Cell Physics to Computational Inverse Design.* PhD thesis, University of California, Berkeley, 2012. (cit. on p. 99)

[132] O. D. Miller, C. W. Hsu, M. T. H. Reid, W. Qiu, B. G. DeLacy, J. D. Joannopoulos, M. Soljačić, and S. G. Johnson. Fundamental limits to extinction by

metallic nanoparticles. *Phys. Rev. Lett.*, 112:123903, 2014. doi: 10.1103/PhysRevLett.112.123903. (cit. on pp. 6, 95, and 109)

[133] O. D. Miller, A. G. Polimeridis, M. T. H. Reid, C. W. Hsu, B. G. DeLacy, J. D. Joannopoulos, M. Soljačić, and S. G. Johnson. Limits to the resonant optical response of metals. 2014. In preparation. (cit. on p. 6)

[134] A. E. Miroshnichenko, S. Flach, and Y. S. Kivshar. Fano resonances in nanoscale structures. *Rev. Mod. Phys.*, 82:2257–2298, 2010. doi: 10.1103/RevModPhys.82.2257. (cit. on pp. 76 and 77)

[135] N. Moiseyev. Suppression of Feshbach resonance widths in two-dimensional waveguides and quantum dots: a lower bound for the number of bound states in the continuum. *Phys. Rev. Lett.*, 102:167404, 2009. doi: 10.1103/PhysRevLett.102.167404. (cit. on pp. 8, 9, and 39)

[136] N. M. Mojarad, V. Sandoghdar, and M. Agio. Plasmon spectra of nanospheres under a tightly focused beam. *J. Opt. Soc. Am. B*, 25:651–658, 2008. doi: 10.1364/JOSAB.25.000651. (cit. on p. 92)

[137] M. I. Molina, A. E. Miroshnichenko, and Y. S. Kivshar. Surface bound states in the continuum. *Phys. Rev. Lett.*, 108:070401, 2012. doi: 10.1103/PhysRevLett.108.070401. (cit. on pp. 8, 9, 23, 24, 38, and 39)

[138] F. Monticone and A. Alù. Embedded photonic eigenvalues in 3D nanostructures. *Phys. Rev. Lett.*, 112:213903, 2014. doi: 10.1103/PhysRevLett.112.213903. (cit. on pp. 39 and 111)

[139] E. Moreno, F. J. García-Vidal, and L. Martín-Moreno. Enhanced transmission and beaming of light via photonic crystal surface modes. *Phys. Rev. B*, 69:121402, 2004. doi: 10.1103/PhysRevB.69.121402. (cit. on p. 7)

[140] S. Mukherjee, H. Sobhani, J. B. Lassiter, R. Bardhan, P. Nordlander, and N. J. Halas. Fanoshells: Nanoparticles with built-in Fano resonances. *Nano Lett.*, 10: 2694–2701, 2010. doi: 10.1021/nl1016392. (cit. on pp. 76, 77, 84, 90, and 93)

[141] B. A. Munk. *Frequency Selective Surfaces: Theory and Design.* Wiley, New York, 2000. (cit. on pp. 94 and 95)

[142] A. Mutapcic, S. Boyd, A. Farjadpour, S. G. Johnson, and Y. Avniel. Robust design of slow-light tapers in periodic waveguides. *Eng. Optim.*, 41:365–384, 2009. doi: 10.1080/03052150802576797. (cit. on p. 105)

[143] S. Naboko. Dense point spectra of Schrödinger and Dirac operators. *Theor. Math. Phys.*, 68:646–653, 1986. doi: 10.1007/BF01017793. (cit. on pp. 8 and 9)

[144] A. Naweed, G. Farca, S. I. Shopova, and A. T. Rosenberger. Induced transparency and absorption in coupled whispering-gallery microresonators. *Phys. Rev. A*, 71: 043804, 2005. doi: 10.1103/PhysRevA.71.043804. (cit. on p. 77)

[145] R. L. Newman. *Head-up displays: designing the way ahead*. Ashgate Publishing, Surrey, UK, 1995. (cit. on p. 61)

[146] J. U. Nöckel. Resonances in quantum-dot transport. *Phys. Rev. B*, 46:15348–15356, 1992. doi: 10.1103/PhysRevB.46.15348. (cit. on pp. 8, 9, and 109)

[147] H. Noh, S. F. Liew, V. Saranathan, S. G. J. Mochrie, R. O. Prum, E. R. Dufresne, and H. Cao. How noniridescent colors are generated by quasi-ordered structures of bird feathers. *Adv. Mater.*, 22:2871–2880, 2010. doi: 10.1002/adma.200903699. (cit. on pp. 94, 95, and 97)

[148] H. Noh, Y. Chong, A. D. Stone, and H. Cao. Perfect coupling of light to surface plasmons by coherent absorption. *Phys. Rev. Lett.*, 108:186805, 2012. doi: 10.1103/PhysRevLett.108.186805. (cit. on p. 110)

[149] T. Ochiai and K. Sakoda. Dispersion relation and optical transmittance of a hexagonal photonic crystal slab. *Phys. Rev. B*, 63:125107, 2001. doi: 10.1103/PhysRevB.63.125107. (cit. on pp. 8, 9, 22, and 40)

[150] T. Opatrný and D.-G. Welsch. Coupled cavities for enhancing the cross-phase-modulation in electromagnetically induced transparency. *Phys. Rev. A*, 64:023805, 2001. doi: 10.1103/PhysRevA.64.023805. (cit. on p. 77)

[151] A. Oskooi, A. Mutapcic, S. Noda, J. D. Joannopoulos, S. P. Boyd, and S. G. Johnson. Robust optimization of adiabatic tapers for coupling to slow-light photonic-crystal waveguides. *Opt. Express*, 20:21558–21575, 2012. doi: 10.1364/OE.20.021558. (cit. on p. 105)

[152] A. F. Oskooi, D. Roundy, M. Ibanescu, P. Bermel, J. D. Joannopoulos, and S. G. Johnson. MEEP: A flexible free-software package for electromagnetic simulations by the FDTD method. *Comput. Phys. Commun.*, 181:687–702, 2010. doi: 10.1016/j.cpc.2009.11.008. (cit. on pp. 11, 48, and 109)

[153] V. Pacradouni, W. J. Mandeville, A. R. Cowan, P. Paddon, J. F. Young, and S. R. Johnson. Photonic band structure of dielectric membranes periodically textured in two dimensions. *Phys. Rev. B*, 62:4204–4207, 2000. doi: 10.1103/PhysRevB.62.4204. (cit. on pp. 8, 9, 22, and 40)

[154] P. Paddon and J. F. Young. Two-dimensional vector-coupled-mode theory for textured planar waveguides. *Phys. Rev. B*, 61:2090–2101, 2000. doi: 10.1103/PhysRevB.61.2090. (cit. on pp. 8, 9, and 22)

[155] E. D. Palik. *Handbook of Optical Constants of Solids*. Academic Press, New York, 1985. (cit. on pp. 65, 67, 89, and 91)

[156] N. Papasimakis, V. A. Fedotov, N. I. Zheludev, and S. L. Prosvirnin. Metamaterial analog of electromagnetically induced transparency. *Phys. Rev. Lett.*, 101:253903, 2008. doi: 10.1103/PhysRevLett.101.253903. (cit. on pp. 77 and 89)

[157] S.-H. K. Park, C.-S. Hwang, M. Ryu, S. Yang, C. Byun, J. Shin, J.-I. Lee, K. Lee, M. S. Oh, and S. Im. Transparent and photo-stable ZnO thin-film transistors to drive an active matrix organic-light- emitting-diode display panel. *Adv. Mater.*, 21:678–682, 2009. doi: 10.1002/adma.200801470. (cit. on p. 62)

[158] A. R. Parker, R. C. McPhedran, D. R. McKenzie, L. C. Botten, and N.-A. P. Nicorovici. Aphrodite's iridescence. *Nature*, 409:36–37, 2001. doi: 10.1038/35051168. (cit. on p. 2)

[159] A. R. Parker, V. L. Welch, D. Driver, and N. Martini. Structural colour: Opal analogue discovered in a weevil. *Nature*, 426:786–787, 2003. doi: 10.1038/426786a. (cit. on p. 2)

[160] R. Parker. Resonance effects in wake shedding from parallel plates: Some experimental observations. *J. Sound Vib.*, 4:62, 1966. doi: 10.1016/0022-460X(66)90154-4. (cit. on pp. 8 and 9)

[161] J. B. Pendry, D. Schurig, and D. R. Smith. Controlling electromagnetic fields. *Science*, 312:1780–1782, 2006. doi: 10.1126/science.1125907. (cit. on p. 1)

[162] Y. Plotnik, O. Peleg, F. Dreisow, M. Heinrich, S. Nolte, A. Szameit, and M. Segev. Experimental observation of optical bound states in the continuum. *Phys. Rev. Lett.*, 107:183901, 2011. doi: 10.1103/PhysRevLett.107.183901. (cit. on pp. 8, 9, 23, 24, 28, 39, and 60)

[163] R. Porter and D. Evans. Embedded Rayleigh-Bloch surface waves along periodic rectangular arrays. *Wave Motion*, 43:29–50, 2005. doi: 10.1016/j.wavemoti.2005.05.005. (cit. on pp. 8, 9, 17, 23, 24, 29, 38, 39, 60, and 109)

[164] R. A. Potyrailo, H. Ghiradella, A. Vertiatchikh, K. Dovidenko, J. R. Cournoyer, and E. Olson. Morpho butterfly wing scales demonstrate highly selective vapour response. *Nature Photon.*, 1:123–128, 2007. doi: 10.1038/nphoton.2007.2. (cit. on p. 94)

[165] A. D. Pris, Y. Utturkar, C. Surman, W. G. Morris, A. Vert, S. Zalyubovskiy, T. Deng, H. T. Ghiradella, and R. A. Potyrailo. Towards high-speed imaging of

infrared photons with bio-inspired nanoarchitectures. *Nature Photon.*, 6:195–200, 2012. doi: 10.1038/nphoton.2011.355. (cit. on p. 94)

[166] E. Prodan, C. Radloff, N. J. Halas, and P. Nordlander. A hybridization model for the plasmon response of complex nanostructures. *Science*, 302:419–422, 2003. doi: 10.1126/science.1089171. (cit. on p. 76)

[167] R. O. Prum, R. H. Torres, S. Williamson, and J. Dyck. Coherent light scattering by blue feather barbs. *Nature*, 396:28–29, 1998. doi: 10.1038/23838. (cit. on pp. 2 and 94)

[168] W. Qiu, B. G. DeLacy, S. G. Johnson, J. D. Joannopoulos, and M. Soljačić. Optimization of broadband optical response of multilayer nanospheres. *Opt. Express*, 20:18494–18504, 2012. doi: 10.1364/OE.20.018494. (cit. on pp. 67, 87, and 90)

[169] M. Rahmani, D. Y. Lei, V. Giannini, B. Lukiyanchuk, M. Ranjbar, T. Y. F. Liew, M. Hong, and S. A. Maier. Subgroup decomposition of plasmonic resonances in hybrid oligomers: Modeling the resonance lineshape. *Nano Lett.*, 12:2101–2106, 2012. doi: 10.1021/nl3003683. (cit. on p. 76)

[170] M. Rahmani, B. Luk'yanchuk, and M. Hong. Fano resonance in novel plasmonic nanostructures. *Laser Photonics Rev.*, 7:329–349, 2013. doi: 10.1002/lpor.201200021. (cit. on pp. 76 and 77)

[171] P. T. Rakich, M. S. Dahlem, S. Tandon, M. Ibanescu, M. Soljačić, G. S. Petrich, J. D. Joannopoulos, L. A. Kolodziejski, and E. P. Ippen. Achieving centimetre-scale supercollimation in a large-area two-dimensional photonic crystal. *Nature Mater.*, 5:93–96, 2006. doi: 10.1038/nmat1568. (cit. on p. 1)

[172] M. T. H. Reid. scuff-EM: Free, open-source boundary-element software, http://homerreid.com/scuff-EM. (cit. on p. 104)

[173] M. T. H. Reid and S. G. Johnson. Efficient computation of power, force, and torque in BEM scattering calculations. 2013. arXiv: 1307.2966. (cit. on p. 104)

[174] W. Robertson, G. Arjavalingam, R. Meade, K. Brommer, A. Rappe, and J. Joannopoulos. Observation of surface photons on periodic dielectric arrays. *Opt. Lett.*, 18:528–530, 1993. doi: 10.1364/OL.18.000528. (cit. on pp. 7 and 9)

[175] M. Robnik. A simple separable Hamiltonian having bound states in the continuum. *J. Phys. A Math. Gen.*, 19:3845, 1986. doi: 10.1088/0305-4470/19/18/029. (cit. on pp. 8, 9, and 109)

[176] A. Rodriguez, M. Soljačić, J. D. Joannopoulos, and S. G. Johnson. $\chi^{(2)}$ and $\chi^{(3)}$ harmonic generation at a critical power in inhomogeneous doublyresonant cavities. *Opt. Express*, 15:7303–7318, 2007. doi: 10.1364/OE.15.007303. (cit. on p. 110)

[177] E. L. Ru and P. Etchegoin. *Principles of surface-enhanced Raman spectroscopy: and related plasmonic effects*. Elsevier, Amsterdam, 2008. (cit. on p. 22)

[178] Z. Ruan and S. Fan. Temporal coupled-mode theory for Fano resonance in light scattering by a single obstacle. *J. Phys. Chem. C*, 114:7324–7329, 2010. doi: 10.1021/jp9089722. (cit. on pp. 77, 79, 81, 82, and 87)

[179] Z. Ruan and S. Fan. Superscattering of light from subwavelength nanostructures. *Phys. Rev. Lett.*, 105:013901, 2010. doi: 10.1103/PhysRevLett.105.013901. (cit. on p. 68)

[180] Z. Ruan and S. Fan. Design of subwavelength superscattering nanospheres. *Appl. Phys. Lett.*, 98:043101, 2011. doi: 10.1063/1.3536475. (cit. on pp. 68, 76, and 79)

[181] Z. Ruan and S. Fan. Temporal coupled-mode theory for light scattering by an arbitrarily shaped object supporting a single resonance. *Phys. Rev. A*, 85:043828, 2012. doi: 10.1103/PhysRevA.85.043828. (cit. on pp. 77, 79, 81, 82, and 110)

[182] K. Sakoda. *Optical properties of photonic crystals*, volume 80. Springer, 2005. (cit. on p. 59)

[183] J. V. Sanders. Colour of precious opal. *Nature*, 204:1151–1153, 1964. doi: 10.1038/2041151a0. (cit. on p. 2)

[184] V. Saranathan, C. O. Osuji, S. G. J. Mochrie, H. Noh, S. Narayanan, A. Sandy, E. R. Dufresne, and R. O. Prum. Structure, function, and self-assembly of single network gyroid (i4132) photonic crystals in butterfly wing scales. *Proc. Natl. Acad. Sci. U.S.A.*, 107:11676–11681, 2010. doi: 10.1073/pnas.0909616107. (cit. on pp. 2 and 94)

[185] V. Saranathan, J. D. Forster, H. Noh, S.-F. Liew, S. G. J. Mochrie, H. Cao, E. R. Dufresne, and R. O. Prum. Structure and optical function of amorphous photonic nanostructures from avian feather barbs: a comparative small angle x-ray scattering (saxs) analysis of 230 bird species. *J. R. Soc. Interface*, 9:2563–2580, 2012. doi: 10.1098/rsif.2012.0191. (cit. on pp. 94 and 95)

[186] A. E. Schlather, N. Large, A. S. Urban, P. Nordlander, and N. J. Halas. Near-field mediated plexcitonic coupling and giant rabi splitting in individual metallic dimers. *Nano Lett.*, 13:3281–3286, 2013. doi: 10.1021/nl4014887. (cit. on p. 76)

[187] S. H. Schwartz. *Visual Perception: A Clinical Orientation*. McGraw Hill, New York, 4 edition, 2010. (cit. on p. 67)

[188] Y. Shen, C. W. Hsu, Y. X. Yeng, I. Celanovic, J. D. Joannopoulos, and M. Soljačić. Broadband angular selectivity of light: progress, applications, and challenges. 2014. In preparation. (cit. on p. 6)

[189] S. P. Shipman and S. Venakides. Resonance and bound states in photonic crystal slabs. *SIAM J. Appl. Math.*, 64:322–342, 2003. doi: 10.1137/S0036139902411120. (cit. on p. 9)

[190] S. P. Shipman and S. Venakides. Resonant transmission near nonrobust periodic slab modes. *Phys. Rev. E*, 71:026611, 2005. doi: 10.1103/PhysRevE.71.026611. (cit. on pp. 8, 9, 22, and 39)

[191] S. P. Shipman and A. Welters. Resonance in anisotropic layered media. *Mathematical Methods in Electromagnetic Theory (MMET), 2012 International Conference on*, pages 227–232, 2012. (cit. on pp. 8 and 9)

[192] V. R. Shrestha, S.-S. Lee, E.-S. Kim, and D.-Y. Choi. Non-iridescent transmissive structural color filter featuring highly efficient transmission and high excitation purity. *Sci. Rep.*, 4:4921, 2014. doi: 10.1038/srep04921. (cit. on pp. 94 and 95)

[193] O. Sigmund. Manufacturing tolerant topology optimization. *Acta Mech. Sinica*, 25:227–239, 2009. doi: 10.1007/s10409-009-0240-z. (cit. on p. 105)

[194] A. H. Sihvola. *Electromagnetic mixing formulas and applications*. Institution of Electrical Engineers, London, 1999. (cit. on p. 89)

[195] D. Sikdar, I. D. Rukhlenko, W. Cheng, and M. Premaratne. Unveiling ultrasharp scattering-switching signatures of layered gold-dielectric-gold nanospheres. *J. Opt. Soc. Am. B*, 30:2066–2074, 2013. doi: 10.1364/JOSAB.30.002066. (cit. on p. 90)

[196] M. G. Silveirinha. Trapping light in open plasmonic nanostructures. *Phys. Rev. A*, 89:023813, 2014. doi: 10.1103/PhysRevA.89.023813. (cit. on pp. 39 and 111)

[197] B. Simon. Some Schrödinger operators with dense point spectrum. *Proc. Amer. Math. Soc.*, 125:203–208, 1997. doi: 10.1090/S0002-9939-97-03559-4. (cit. on pp. 8 and 9)

[198] D. D. Smith, H. Chang, K. A. Fuller, A. T. Rosenberger, and R. W. Boyd. Coupled-resonator-induced transparency. *Phys. Rev. A*, 69:063804, 2004. doi: 10.1103/PhysRevA.69.063804. (cit. on p. 77)

[199] Y. Sonnefraud, N. Verellen, H. Sobhani, G. A. Vandenbosch, V. V. Moshchalkov, P. Van Dorpe, P. Nordlander, and S. A. Maier. Experimental realization of subradiant, superradiant, and Fano resonances in ring/disk plasmonic nanocavities. *ACS Nano*, 4:1664–1670, 2010. doi: 10.1021/nn901580r. (cit. on pp. 76 and 93)

[200] G. I. Stegeman. Normal-mode surface waves in the pseudobranch on the (001) plane of gallium arsenide. *J. Appl. Phys.*, 47:1712–1713, 1976. doi: 10.1063/1.322755. (cit. on p. 39)

[201] F. H. Stillinger and D. R. Herrick. Bound states in the continuum. *Phys. Rev. A*, 11:446–454, 1975. doi: 10.1103/PhysRevA.11.446. (cit. on pp. 8, 9, 23, 24, and 38)

[202] W. Suh, Z. Wang, and S. Fan. Temporal coupled-mode theory and the presence of non-orthogonal modes in lossless multimode cavities. *IEEE J. Quantum Electron.*, 40:1511–1518, 2004. doi: 10.1109/JQE.2004.834773. (cit. on pp. 77, 81, 82, 86, and 93)

[203] T. Sun, G. Pettitt, N. T. Ho, K. Eckles, B. Clifton, and B. Cheng. Full color, high contrast front projection on black emissive display. *Proc. SPIE*, 8254:82540K, 2012. doi: 10.1117/12.906619. (cit. on p. 61)

[204] X.-D. Sun and J.-Q. Liu. Light emitting material integrated into a substantially transparent substrate, 2006. US Patent 6986581 filed 3 Nov 2004, and issued 17 Jan 2006. (cit. on p. 61)

[205] K. Svanberg. A class of globally convergent optimization methods based on conservative convex separable approximations. *SIAM J. Optimiz.*, 12:555–573, 2002. doi: 10.1137/S1052623499362822. (cit. on p. 100)

[206] A. Szameit and S. Nolte. Discrete optics in femtosecond-laser-written photonic structures. *J. Phys. B*, 43:163001, 2010. doi: 10.1088/0953-4075/43/16/163001. (cit. on pp. 95 and 104)

[207] M. Tabata, I. Adachi, H. Kawai, M. Kubo, and T. Sato. Recent progress in silica aerogel Cherenkov radiator. *Phys. Procedia*, 37:642–649, 2012. doi: 10.1016/j.phpro.2012.02.410. (cit. on p. 92)

[208] A. Taflove and S. C. Hagness. *Computational electrodynamics: the finite-difference time-domain method*. Artech House, Boston, 3 edition, 2005. (cit. on p. 25)

[209] Y. Takeoka. Angle-independent structural coloured amorphous arrays. *J. Mater. Chem.*, 22:23299–23309, 2012. doi: 10.1039/C2JM33643J. (cit. on pp. 94 and 95)

[210] Y. Takeoka, M. Honda, T. Seki, M. Ishii, and H. Nakamura. Structural colored liquid membrane without angle dependence. *ACS Appl. Mater. Inter.*, 1:982–986, 2009. doi: 10.1021/am900074v. (cit. on pp. 94 and 95)

[211] M. Tomita, K. Totsuka, R. Hanamura, and T. Matsumoto. Tunable Fano interference effect in coupled-microsphere resonator-induced transparency. *J. Opt. Soc. Am. B*, 26:813–818, 2009. doi: 10.1364/JOSAB.26.000813. (cit. on p. 77)

[212] M. I. Tribelsky and B. S. Luk'yanchuk. Anomalous light scattering by small particles. *Phys. Rev. Lett.*, 97:263902, 2006. doi: 10.1103/PhysRevLett.97.263902. (cit. on pp. 65, 68, and 95)

[213] M. I. Tribelsky, S. Flach, A. E. Miroshnichenko, A. V. Gorbach, and Y. S. Kivshar. Light scattering by a finite obstacle and Fano resonances. *Phys. Rev. Lett.*, 100: 043903, 2008. doi: 10.1103/PhysRevLett.100.043903. (cit. on p. 79)

[214] K. L. Tsakmakidis, C. Hermann, A. Klaedtke, C. Jamois, and O. Hess. Surface plasmon polaritons in generalized slab heterostructures with negative permittivity and permeability. *Phys. Rev. B*, 73:085104, 2006. doi: 10.1103/PhysRevB.73.085104. (cit. on p. 7)

[215] K. Ueno, A. Inaba, Y. Sano, M. Kondoh, and M. Watanabe. A soft glassy colloidal array in ionic liquid, which exhibits homogeneous, non-brilliant and angle-independent structural colours. *Chem. Commun.*, pages 3603–3605, 2009. doi: 10.1039/B905108B. (cit. on pp. 94 and 95)

[216] F. Ursell. Trapping modes in the theory of surface waves. *Math. Proc. Cambridge*, 47:347–358, 1951. doi: 10.1017/S0305004100026700. (cit. on pp. 8 and 9)

[217] J. Čtyroký. Photonic bandgap structures in planar waveguides. *J. Opt. Soc. Am. A*, 18:435–441, 2001. doi: 10.1364/JOSAA.18.000435. (cit. on pp. 8, 9, and 109)

[218] N. Verellen, Y. Sonnefraud, H. Sobhani, F. Hao, V. V. Moshchalkov, P. V. Dorpe, P. Nordlander, and S. A. Maier. Fano resonances in individual coherent plasmonic nanocavities. *Nano Lett.*, 9:1663–1667, 2009. doi: 10.1021/nl9001876. (cit. on p. 76)

[219] S. Vignolini, P. J. Rudall, A. V. Rowland, A. Reed, E. Moyroud, R. B. Faden, J. J. Baumberg, B. J. Glover, and U. Steiner. Pointillist structural color in pollia fruit. *Proc. Natl. Acad. Sci. U.S.A.*, 109:15712–15715, 2012. doi: 10.1073/pnas.1210105109. (cit. on pp. 2 and 94)

[220] J. von Neumann and E. Wigner. Über merkwürdige diskrete eigenwerte. *Phys. Z.*, 30:465–467, 1929. (cit. on pp. 8, 23, 24, 38, and 39)

[221] P. Vukusic, J. R. Sambles, C. R. Lawrence, and R. J. Wootton. Quantified interference and diffraction in single Morpho butterfly scales. *Proc. R. Soc. Lond. B*, 266:1403–1411, 1999. doi: 10.1098/rspb.1999.0794. (cit. on pp. 2 and 94)

[222] P. Vukusic, J. R. Sambles, and C. R. Lawrence. Structural colour: Colour mixing in wing scales of a butterfly. *Nature*, 404:457–457, 2000. doi: doi:10.1038/35006561. (cit. on p. 2)

[223] J. Vučković, M. Lončar, H. Mabuchi, and A. Scherer. Design of photonic crystal microcavities for cavity QED. *Phys. Rev. E*, 65:016608, 2001. doi: 10.1103/PhysRevE.65.016608. (cit. on p. 17)

[224] W. Wan, Y. Chong, L. Ge, H. Noh, A. D. Stone, and H. Cao. Time-reversed lasing and interferometric control of absorption. *Science*, 331(6019):889–892, 2011. doi: 10.1126/science.1200735. (cit. on p. 110)

[225] F. Wang, J. S. Jensen, and O. Sigmund. Robust topology optimization of photonic crystal waveguides with tailored dispersion properties. *J. Opt. Soc. Am. B*, 28: 387–397, 2011. doi: 10.1364/JOSAB.28.000387. (cit. on p. 105)

[226] H. Wang, Y. Wu, B. Lassiter, C. L. Nehl, J. H. Hafner, P. Nordlander, and N. J. Halas. Symmetry breaking in individual plasmonic nanoparticles. *Proc. Natl. Acad. Sci. U.S.A.*, 103:10856–10860, 2006. doi: 10.1073/pnas.0604003103. (cit. on p. 93)

[227] M. Wang, M. Cao, X. Chen, and N. Gu. Subradiant plasmon modes in multilayer metal-dielectric nanoshells. *J. Phys. Chem. C*, 115:20920–20925, 2011. doi: 10.1021/jp205736d. (cit. on p. 90)

[228] Z. Wang, Y. Chong, J. D. Joannopoulos, and M. Soljačić. Observation of unidirectional backscattering-immune topological electromagnetic states. *Nature*, 461: 772–775, 2009. doi: 10.1038/nature08293. (cit. on p. 1)

[229] M. R. Watts, S. G. Johnson, H. A. Haus, and J. D. Joannopoulos. Electromagnetic cavity with arbitrary Q and small modal volume without a complete photonic bandgap. *Opt. Lett.*, 27:1785–1787, 2002. doi: 10.1364/OL.27.001785. (cit. on pp. 8, 9, 23, 24, 38, and 109)

[230] S. Weimann, Y. Xu, R. Keil, A. E. Miroshnichenko, A. Tünnermann, S. Nolte, A. A. Sukhorukov, A. Szameit, and Y. S. Kivshar. Compact surface Fano states embedded in the continuum of waveguide arrays. *Phys. Rev. Lett.*, 111:240403, 2013. doi: 10.1103/PhysRevLett.111.240403. (cit. on p. 39)

[231] H. M. Whitney, M. Kolle, P. Andrew, L. Chittka, U. Steiner, and B. J. Glover. Floral iridescence, produced by diffractive optics, acts as a cue for animal pollinators. *Science*, 323:130–133, 2009. doi: 10.1126/science.1166256. (cit. on pp. 2 and 94)

[232] G. P. Wiederrecht, G. A. Wurtz, and J. Hranisavljevic. Coherent coupling of molecular excitons to electronic polarizations of noble metal nanoparticles. *Nano Lett.*, 4:2121–2125, 2004. doi: 10.1021/nl0488228. (cit. on p. 76)

[233] J. J. Wierer, A. David, and M. M. Megens. III-nitride photonic-crystal light-emitting diodes with high extraction efficiency. *Nature Photon.*, 3:163–169, 2009. doi: 10.1038/nphoton.2009.21. (cit. on p. 40)

[234] K. J. Witsch. Examples of embedded eigenvalues for the Dirichlet Laplacian in perturbed waveguides. *Math. Method. Appl. Sci.*, 12:91–93, 1990. doi: 10.1002/mma.1670120107. (cit. on pp. 8 and 9)

[235] C. Wu, N. Arju, G. Kelp, J. A. Fan, J. Dominguez, E. Gonzales, E. Tutuc, I. Brener, and G. Shvets. Spectrally selective chiral silicon metasurfaces based on infrared Fano resonances. *Nat. Commun.*, 5:3892, 2014. doi: 10.1038/ncomms4892. (cit. on p. 68)

[236] D. Wu, S. Jiang, and X. Liu. Tunable Fano resonances in three-layered bimetallic Au and Ag nanoshell. *J. Phys. Chem. C*, 115:23797–23801, 2011. doi: 10.1021/jp209446p. (cit. on p. 90)

[237] X. Wu, S. K. Gray, and M. Pelton. Quantum-dot-induced transparency in a nanoscale plasmonic resonator. *Opt. Express*, 18:23633–23645, 2010. doi: 10.1364/OE.18.023633. (cit. on p. 76)

[238] Q. Xu, S. Sandhu, M. L. Povinelli, J. Shakya, S. Fan, and M. Lipson. Experimental realization of an on-chip all-optical analogue to electromagnetically induced transparency. *Phys. Rev. Lett.*, 96:123901, 2006. doi: 10.1103/PhysRevLett.96.123901. (cit. on p. 77)

[239] C. Yang, L. Hong, W. Shen, Y. Zhang, X. Liu, and H. Zhen. Design of reflective color filters with high angular tolerance by particle swarm optimization method. *Opt. Express*, 21:9315–9323, 2013. doi: 10.1364/OE.21.009315. (cit. on pp. 94 and 95)

[240] Y. Yang, C. Peng, Y. Liang, Z. Li, and S. Noda. Analytical perspective for bound states in the continuum in photonic crystal slabs. *Phys. Rev. Lett.*, 113:037401, 2014. doi: 10.1103/PhysRevLett.113.037401. (cit. on p. 41)

[241] A. A. Yanik, A. E. Cetin, M. Huang, A. Artar, S. H. Mousavi, A. Khanikaev, J. H. Connor, G. Shvets, and H. Altug. Seeing protein monolayers with naked eye through plasmonic Fano resonances. *Proc. Natl. Acad. Sci. U.S.A.*, 108:11784–11789, 2011. doi: 10.1073/pnas.1101910108. (cit. on p. 40)

[242] G. Zengin, G. Johansson, P. Johansson, T. J. Antosiewicz, M. Käll, and T. Shegai. Approaching the strong coupling limit in single plasmonic nanorods interacting with J-aggregates. *Sci. Rep.*, 3:3074, 2013. doi: 10.1038/srep03074. (cit. on p. 76)

[243] Q. Zhan. Cylindrical vector beams: from mathematical concepts to applications. *Adv. Opt. Photon.*, 1:1–57, 2009. doi: 10.1364/AOP.1.000001. (cit. on pp. 40 and 47)

[244] J. M. Zhang, D. Braak, and M. Kollar. Bound states in the continuum realized in the one-dimensional two-particle Hubbard model with an impurity. *Phys. Rev. Lett.*, 109:116405, 2012. doi: 10.1103/PhysRevLett.109.116405. (cit. on pp. 8, 9, 23, 24, and 38)

[245] S. Zhang, D. A. Genov, Y. Wang, M. Liu, and X. Zhang. Plasmon-induced transparency in metamaterials. *Phys. Rev. Lett.*, 101:047401, 2008. doi: 10.1103/PhysRevLett.101.047401. (cit. on pp. 77, 84, and 89)

[246] B. Zhen, S.-L. Chua, J. Lee, A. W. Rodriguez, X. Liang, S. G. Johnson, J. D. Joannopoulos, M. Soljačić, and O. Shapira. Enabling enhanced emission and low-threshold lasing of organic molecules using special Fano resonances of macroscopic photonic crystals. *Proc. Natl. Acad. Sci. U.S.A.*, 110:13711–13716, 2013. doi: 10.1073/pnas.1311866110. (cit. on pp. 40 and 108)

[247] B. Zhen, C. W. Hsu, L. Lu, A. D. Stone, and M. Soljačić. Topological nature of optical bound states in the continuum. *Phys. Rev. Lett.*, 2014. accepted for publication. (cit. on p. 6)

[248] J. Zi, X. Yu, Y. Li, X. Hu, C. Xu, X. Wang, X. Liu, and R. Fu. Coloration strategies in peacock feathers. *Proc. Natl. Acad. Sci. U.S.A.*, 100:12576–12578, 2003. doi: 10.1073/pnas.2133313100. (cit. on p. 2)